Development of a readout electronic for a Si-pixeldetector for application in a Compton camera

DISSERTATION
zur Erlangung des Grades eines Doktors
der Naturwissenschaften

vorgelegt von
Dipl. Phys. Iskander Ibragimov
aus Kasan, Russland

eingereicht beim Fachbereich Physik
der Universität Siegen

Siegen 2004

Gutachter der Dissertation: Prof. Dr. M. Holder
Prof. Dr. G. Zech
Datum der Disputation: 26. Januar 2005

Internetpublikation der Universität Siegen: urn:nbn:de:hbz:467-982

Development of a readout electronic for a Si-pixeldetector for application in a Compton camera

by
Iskander Ibragimov

Abstract: Compton cameras are very promising gamma-ray imaging systems, which have already found their application in astrophysics. Their use in nuclear medicine could offer higher sensitivity and better spatial resolution than existing mechanically-collimated gamma cameras, leading to a reduction of the radiation dose given to a patient. A Compton camera consists basically of two detectors: a scatter detector, where Compton scattering takes place, and a photoabsorber, where the scattered photons are absorbed. Silicon pixel detectors are the best choice for a scatter medium since they provide good position resolution, good energy resolution at room temperature and a relatively small Doppler broadening effect. Scintillation detectors are preferred for the use as a photoabsorber because of their greater stopping power.

In the present work a low noise readout electronic for Si-pixeldetectors with $200\mu m \times 200\mu m$ pixel size has been developed in CMOS technology. The electronic is self-triggering and delivers also a timestamp for the use in coincidences. Bonded to a Si-pixeldetector the readout circuit has been tested with gamma-ray sources; an electronic noise of about $49e^{-}$ was obtained. A pixellated CsI detector read out by a Si PIN photodiode array has been studied as a photoabsorber.

Kurzfassung: Compton-Kameras sind sehr vielversprechende Gamma-Bildgebungssysteme, die bereits ihre Anwendung in der Astrophysik gefunden haben. Ihr Einsatz in der Nuklearmedizin konnte höhere Empfindlichkeit und bessere Ortsauflösung ermöglichen als vorhandene mechanisch-kollimierte Gammakameras. Dadurch kann die einem Patienten verabreichte Strahlendosis vermindert werden. Eine Compton-Kamera besteht grundsätzlich aus zwei Detektoren: einem Streuungsdetektor, wo die Compton-Streuung stattfindet, und einem Photoabsorber, wo die gestreuten Photonen absorbiert werden. Silizium-Pixeldetektoren sind die beste Wahl für ein Streuungsmedium, da sie gute Ortsauflösung, gute Energieauflösung bei Raumtemperatur und relativ kleine Dopplerverbreitung bieten. Szintillationsdetektoren werden für den Einsatz als Photoabsorber wegen ihres größeren Strahlungsbremsvermögens bevorzugt.

In Rahmen dieser Arbeit wurde eine rauscharme Ausleseelektronik für Si-Pixeldetektoren mit einer Pixel-Größe von $200\mu m \times 200\mu m$ in der CMOS Technologie entwickelt. Die Auslese ist selbsttriggernd und liefert außerdem eine Zeitmarke zur Verwendung in Koinzidenzen. Gebondet an einem Si-Pixeldetector wurde die Ausleseelektronik mit Gammaquellen getestet; elektronisches Rauschen von ungefähr $49e^{-}$ wurde gemessen. Außerdem wurde ein pixelierter CsI Detektor mit Photodiodenauslese auf möglichen Einsatz als Photoabsorber untersucht.

Contents

1 Introduction **1**

2 Radiation detectors **3**

2.1 Interaction of radiation with matter . . . 3

2.1.1 Interaction of charged particles with matter . . . 3

2.1.2 Interaction of gamma radiation with matter . . . 6

2.2 Semiconductor detectors . . . 9

2.2.1 Semiconductors . . . 9

2.2.2 p-n junction . . . 12

2.2.3 Reverse biased p^{+}-n junction as a radiation detector . . . 13

2.2.4 Punch-through bias structure . . . 15

2.2.5 Multiple guard ring structure . . . 16

2.2.6 Intrinsic energy resolution of semiconductor detectors . . . 17

2.3 Scintillation detectors . . . 17

2.3.1 Scintillators . . . 17

2.3.2 Detection of scintillation light . . . 19

3 Compton camera prototype **23**

3.1 Choice of the detectors . . . 25

3.1.1 Scatter detector . . . 25

3.1.2 Photoabsorber . . . 26

3.2 Position uncertainty . . . 27

3.2.1 Geometry considerations . . . 28

3.2.2 Energy resolution . . . 30

3.2.3 Doppler broadening . . . 30

4 Readout electronics for scatter detector **35**

4.1 Noise considerations . . . 37

4.2 Design of the CSA . . . 40

4.2.1 Input noise matching conditions . . . 42

4.2.2 Large GBW amplifier . . . 44

4.2.3 Feedback . . . 48

4.2.4 Inject capacitor . . . 49

4.2.5 Implementation . . . 50

4.3 The CRRC shaper . . . 53

4.4 Peak detector 56
4.5 Discriminator 56
4.6 Time measurement 59
4.7 Readout logic 60
4.7.1 Pixel control logic 61
4.7.2 End-of-row and end-of-column logics 61
4.7.3 Readout control logic 62
4.8 The Digital-to-Analog Converter 63
4.8.1 Current reference 64
4.8.2 IMON structure 66

5 Measurements 67
5.1 Setup for data acquisition 67
5.2 Performance of the CSA 70
5.3 Performance of the shaper 73
5.4 Performance of the peak detector 77
5.5 Performance of the discriminator 78
5.6 Performance of the Time-to-Voltage Converter 81
5.7 Performance of the data acquisition circuitry 83
5.8 Performance of the test detector 86
5.9 Test of the readout electronic with the detector 88

6 Cesium Iodide detector 91
6.1 Performance of the photodiode array 92
6.2 Performance of the trigger circuitry 94
6.3 Performance of the cesium iodide detector 95
6.3.1 Light collection 95
6.3.2 Energy resolution 96

7 Summary and Outlook 101
7.1 Summary 101
7.2 Outlook 102

A Noise in electronic devices 105
A.1 Thermal noise 105
A.2 Flicker noise 105
A.3 Shot noise 106
A.4 MOSFET noise model 106

B Layout of the RAMSES chip 109

C Typical settings of the RAMSES chip 111

D Software for data acquisition and test 113

Bibliography 115

List of Figures **119**

Chapter 1

Introduction

The idea of using Compton scattering of photons in imaging applications come up in the middle of 70-th as Schoenfelder[Sch73] and Todd[Tod74] made proposals in astrophysics and nuclear imaging, respectively. It was suggested to replace a collimator, usually placed in front of an imaging detector, with an another position-sensitive detector, which will act as a Compton scatter for incident photons. If the initial energy of a photon is known and the scattered photon is fully absorbed in the second detector, the direction of the incident photon can be determined from the positions of interaction in the two detectors and the energy deposited in the scatter detector.

In astrophysics investigation of gamma radiation from remote objects in the 1-30 MeV energy range is of interest. The use of lead collimators, which for such high energies have to be very thick and therefore heavy, is impractical in satellite missions. As an alternative, the Compton camera principle was found to be very useful and the first Compton telescope COMPTEL was constructed and launched in 1991. The success of this mission encourages the development of the second generation of Compton telescopes. The MEGA telescope[Kan04] with the improved sensitivity and the upper energy range limit of 50MeV is now in a test phase.

The application of a Compton camera in nuclear imaging is supposed to achieve a better sensitivity in comparison with the existing mechanically-collimated cameras, called also Anger cameras. The first working Compton camera prototype build by Singh and Doria[Sin83] has shown an improvement of a factor of ten in sensitivity at approximately the same spatial resolution. In this prototype a high-purity germanium detector was used as a scatter detector; since germanium detectors need cryogenic cooling for their operation, the prototype was too bulky. Another Compton camera prototype, based on a silicon pad detector and the Michigan SPECT[1] system (SPRINT[2]), was developed at the University of Michigan[Leb99]. The performance of the prototype at 140.5keV energy was found to be worse than that of the Anger camera, but similar to it at 364.5keV energy.

A Compton camera prototype, proposed in our group, uses a silicon pixeldetector as a scatter detector and a pixellated CsI detector, read out by a silicon PIN photodiode array, as a photoabsorber. The major advantage of the proposed camera is its compactness and room-temperature operation. The subject of this thesis is mainly concerned with the

[1]Single Photon Emission Computed Tomography

[2]Single Photon RINg Tomograph

development of the low-noise readout electronics for the scatter detector.

The dissertation is organised into seven chapters. Chapter one provides a historical overview of the Compton camera development, focusing on a progress in medical imaging.

In Chapter two interaction of gamma radiation with matter and properties of some existing detector materials, scintillators and semiconductors, are considered. Afterwards the principle of operation of basic detector components such as a p-n junction and guard rings is explained. Finally the devices used for detection of scintillation light are reviewed.

The subject of Chapter three is the description of the proposed Compton camera prototype. Functionality of the Compton camera, choice of detector materials, position uncertainty due to the geometry of the camera and energy resolution in the first detector are considered.

Chapter four is devoted to the development of readout electronics for Si-pixeldetectors. A systematic concept for the low-noise design of preamplifier and shaper along with simulations is given. Functionality of other signal processing elements is described.

Performance of each readout component, compared with simulations, as well as measurements with a Si-pixeldetector are presented in Chapter five.

In Chapter six the functionality of the CsI detector is explained and its possible application as a photoabsorber is investigated. Performance of the detector, such as the light collection and the energy resolution, is analysed.

Chapter seven summarises the conducted research work and gives proposals for further investigations.

Chapter 2

Radiation detectors

The operation of any radiation detector basically depends on the manner in which the radiation to be detected interacts with the material of the detector itself. Therefore the fundamental mechanisms of the interaction of radiation with matter will be briefly reviewed. For understanding the response of specific types of the detectors the properties of various detector materials, semiconductors and scintillators, will be considered.

2.1 Interaction of radiation with matter

The interaction of radiation with matter can be mainly considered as a transfer of energy from the radiation to matter. The energy transfer mechanism depends strongly on the type of radiation. Whereas for charged particles and photons electromagnetic interactions are the most common processes, strong interactions play the key role for neutrons. The following discussion is mainly concerned with interactions of photons with matter. Since in these interactions energetic secondary electrons are produced, also interactions of charged particles with matter will be briefly reviewed.

2.1.1 Interaction of charged particles with matter

When a charged particle pass through matter two fundamental effects occur: a loss of kinetic energy by the particle and a deflection of the particle from the initial direction. Both effects are caused by ionization and excitation of bound electrons in the material and by radiative losses in the field of nuclei(bremsstrahlung); the deflection of the particle can happen also by elastic scattering from nuclei.

Collisions with electrons are statistical in nature, but great in the number for macroscopic dimensions, therefore fluctuations in the total deposited energy are small. It makes possible to operate with average energy loss per unit path length, called also the *stopping power*, which for ionization losses is given by the Bethe-Bloch formula[Gru96]:

$$\left(-\frac{dE}{dx}\right)_{ion} = 4\pi N_A r_e^2 m_e c^2 z^2 \frac{Z}{A}\frac{1}{\beta^2}\left[ln\frac{2m_e c^2\gamma^2\beta^2}{I} - \beta^2 - \frac{\delta}{2}\right] \tag{2.1}$$

where

z	- charge of the incident particle in units of the elementary charge
Z, A	- atomic number and atomic weight of the absorber
N_A	- Avogadro number
r_e	- classical electron radius
m_e	- electron mass
γ	- Lorentz factor, $\gamma = 1/\sqrt{1-\beta^2}$, where $\beta = v/c$(particle velocity divided by the speed of light)
I	- ionization constant, characteristic of the absorber material, which can be approximated for $Z > 1$ by $I = 16Z^{0.9}eV$
δ	- density effect parameter

At non-relativistic energies the stopping power is dominated by a $1/\beta^2$ factor and therefore decreases with increasing velocity until about $\beta \approx 0.96$, where a minimum is reached. A particle at this point is called a *minimum ionising* particle(MIP). For $300\mu m$ of silicon the energy loss corresponding to one MIP is about 116keV. The minimal stopping power is the same for particles of the same charge.

The energy loss due to bremsstrahlung for a particle of charge z and mass M in a substance of atomic number Z is given by a following formula[Gru96]:

$$\left(-\frac{dE}{dx}\right)_{rad} = \frac{4}{137} N_A \left(\frac{1}{4\pi\epsilon_0} \cdot \frac{e^2}{Mc^2}\right) z^2 \frac{Z^2}{A} E \cdot ln \frac{183}{Z^{1/3}} \tag{2.2}$$

It is noted that in contrast to ionization loss the radiation loss is inversely proportional to the mass squared of the incident particle and directly proportional to the kinetic energy of particle. Therefore, it is obvious, that the radiation losses for protons and heavier particles are negligible. The total energy loss is the sum of both components given by equations 2.1 and 2.2. For electrons in silicon it is given as a function of energy in Figure 2.1. One can see that the minimum of ionization occurs at electron energies of ≈1MeV and radiation losses becomes dominant above 50MeV. Losses of proton, shown also for comparison, have a minimum at much higher energies - 2-3GeV. As was pointed out above, the minimum value of dE/dx is almost the same for electrons and protons since they are particles of the same charge.

Unlike heavy particles an electron may suffer large energy losses during individual collisions which leads to large deflections from the incident direction. Therefore the path of electron will not be a straight line, as would be in the case of heavy particles. The situation is made worse by multiple elastic collisions by atoms of the absorber.

To calculate the range of electrons a so-called Continuous-Slowing-Down Approximation(CSDA) is used. In this approximation, the rate of energy loss at every point along the track is assumed to be equal and energy loss fluctuations are neglected. In Figure 2.2 the average path length, travelled by an electron as it slows down to rest, calculated by the CSDA method[NIST04], is shown as a function of electron energy for silicon, cesium iodide and cadmium telluride.

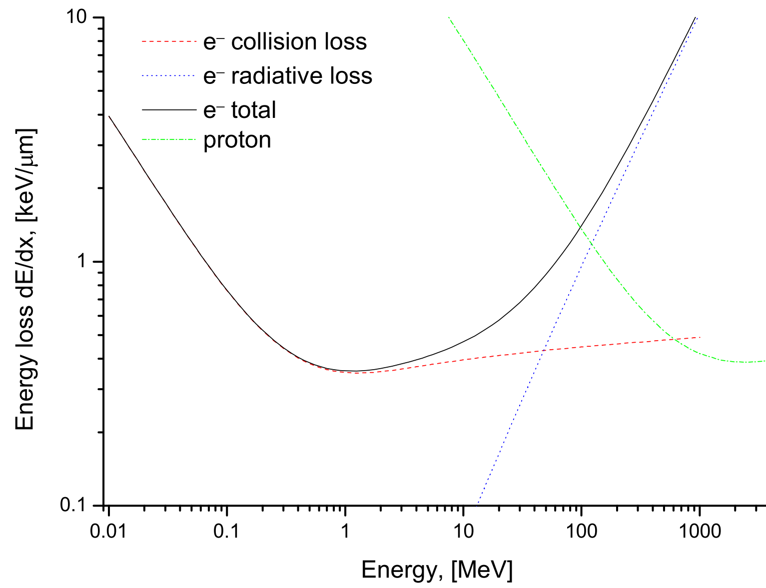

Figure 2.1: Energy loss for electron and proton in silicon

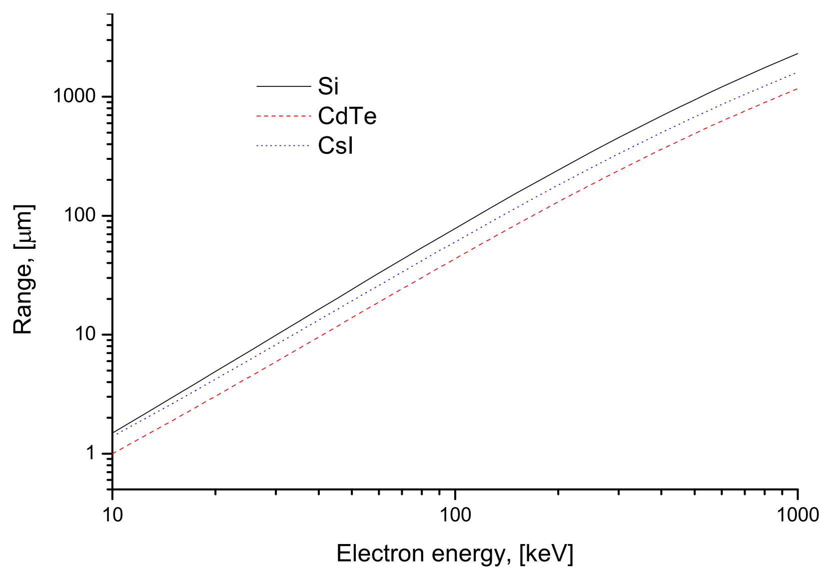

Figure 2.2: Range of electrons in silicon, cesium iodide and cadmium telluride

2.1.2 Interaction of gamma radiation with matter

Gamma rays lose their energy in matter by means of three processes: photoelectric absorption, Compton scattering and pair production. In all three cases secondary particles - free energetic electrons - are created, which interact with matter through ionization and excitation, as was described in the previous section. Each process will be described further in detail.

Photoelectric absorption

If the energy of incident photon is larger than the smallest binding energy of electrons in the atom a photoelectric absorption can happen. In a photoelectric absorption process the whole energy of the incoming photon is transferred to a single atomic electron, ionizing the atom in a single interaction.[1] Thus for a photon with energy E_γ and for an electron with binding energy E_b, a photoelectron with energy $E = E_\gamma - E_b$ is produced. The cross section for the photoeffect can be approximated by[Gru96]:

$$\sigma_{photo} \sim \frac{Z^5}{E_\gamma^{3.5}} \tag{2.3}$$

with Z being atomic number of the absorber. Thus the cross section drops very fast with increasing energy. At energies much higher than the binding energies of electrons in a specific atom this dependence flattens to $\sim E_\gamma^{-1}$.

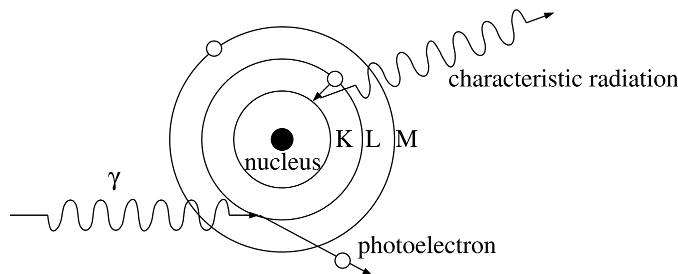

Figure 2.3: Photoelectric absorption

The place of the ejected electron will be taken by an electron from an outer shell. The energy difference between these two shells can be emitted either as a photon(fluorescence or characteristic radiation) or transferred to an electron of the same atom. If this difference is larger than the binding energy of the electron, the latter becomes free(Auger effect). As an example, the interaction of a photon with a K-shell electron is illustrated in Figure 2.3.

Compton scattering

By a Compton scattering[2] only a part of photon energy is transferred to an electron. The electron has to be "free" or loosely bound, that means that its binding energy have to be

[1] Conservation of momentum asserts that the photoeffect is not possible with a free electron.

[2] also referred to as incoherent scattering

much less than the energy of the photon.

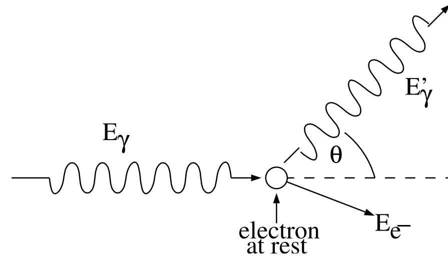

Figure 2.4: Compton scattering

Supposing the struck electron at rest and neglecting its binding energy, the energy transferred to the electron E_{e^-} can be found using energy and momentum conservation:

$$E_{e^-} = E_\gamma \frac{\frac{E\gamma}{m_e c^2}(1 - cos\theta)}{1 + \frac{E\gamma}{m_e c^2}(1 - cos\theta)} \tag{2.4}$$

with the energy of the incident photon E_γ, the energy of the scattered photon E'_γ and the scattering angle θ, as shown in Figure 2.4. The maximal energy is transferred at $\theta = 180°$ and is given by the following function:

$$E_{e^-_{max}} = E_\gamma \frac{2\alpha}{1 + 2\alpha} \tag{2.5}$$

where $\alpha = E_\gamma / m_e c^2$. This function for the energy range of interest is shown in Figure 2.5a. The probability for a Compton scattering per electron to occur is given by the

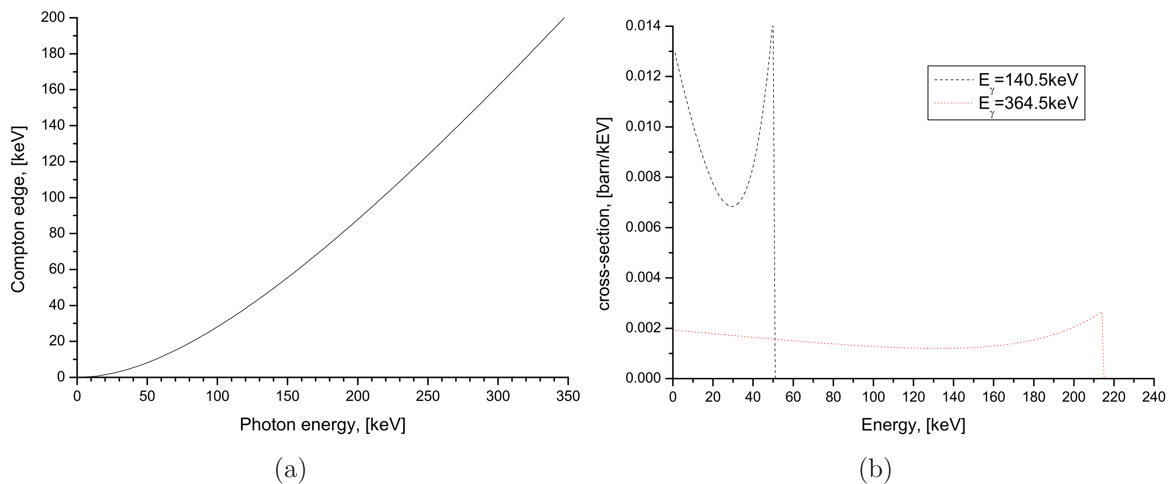

Figure 2.5: a) Energy of the Compton edge as a function of photon energy b) Energy distribution of recoil electrons for E_γ=140.5keV and E_γ=364.5keV

Klein-Nishina formula[Leo94]:

$$\sigma_{compton} = 2\pi r_e^2 \Big\{ \frac{1+\alpha}{\alpha^2} \Big[\frac{2(1+\alpha)}{1+2\alpha} - \frac{1}{\alpha} ln(1+2\alpha) \Big] + \frac{1}{2\alpha} ln(1+2\alpha) - \frac{1+3\alpha}{(1+2\alpha)^2} \Big\} \quad (2.6)$$

From this formula the energy distribution of Compton recoil electrons can be obtained[Leo94]:

$$\frac{d\sigma}{dE_{e^-}} = \frac{\pi r_e^2}{m_e c^2 \alpha^2} \Big[2 + \frac{s^2}{\alpha^2 (1-s)^2} + \frac{s}{1-s} \Big(s - \frac{2}{\alpha} \Big) \Big] \quad (2.7)$$

where $s = E_{e^-}/E_\gamma$. This distribution is shown in Figure 2.5b for two energies of incident photons. It shows an abrupt change at the maximal transferable energy, which is also known as a *Compton edge*.

Pair production

With photon energies above $\approx 1MeV$ another process takes place: creation of electron-positron pairs. A high energetic photon, passing close to the atomic nucleus, interacts with its field. The energy of the photon is converted into the rest energy and kinetic energy of two oppositely charged particles, an electron and a positron. In general the particles do not have equal energy, but their total kinetic energy $E_{kin,\Sigma} = E_\gamma - 1.02MeV$.

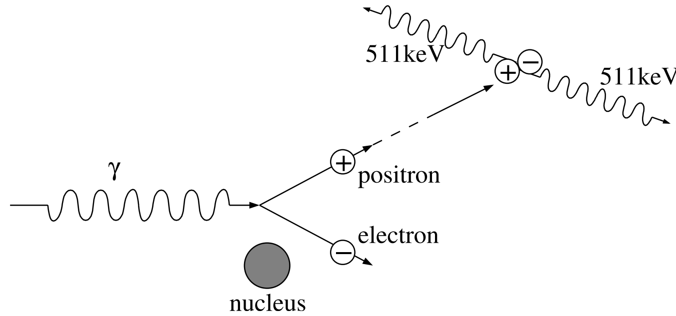

Figure 2.6: Pair production and positron annihilation

Subsequent to formation, both particles dissipate gradually their kinetic energy by ionising and excitation until they are brought to rest. The positron annihilates then with an electron, producing two photons of energy equal to the rest energy of an electron. Because of momentum conservation the photons will move in opposite directions. The process of pair production and positron annihilation is illustrated in Figure 2.6.

Total absorption coefficient

If the beam of N_0 photons passes through an absorber of thickness x, the number of photons in the outcoming beam reduces to

$$N = N_0 e^{-\mu_\Sigma x} \quad (2.8)$$

where μ_Σ is the linear absorption coefficient, which is the sum of linear absorption coefficients of all individual interaction processes, i.e. $\mu_\Sigma = \mu_{photo} + \mu_{compton} + \mu_{pair}$. The linear absorption coefficients for the photo- and Compton effects are connected with corresponding cross sections by the following relations:

$$\mu_{photo} = \rho \frac{N_A}{A} \sigma_{photo} \qquad \mu_{compton} = \rho \frac{N_A}{A} Z \sigma_{compton} \tag{2.9}$$

where N_A is the Avogadro number, A is the mass number of the absorbing material. The linear absorption coefficients of silicon and cesium iodide are given as a function of photon energy for the energy range of interest in Figure 2.7.

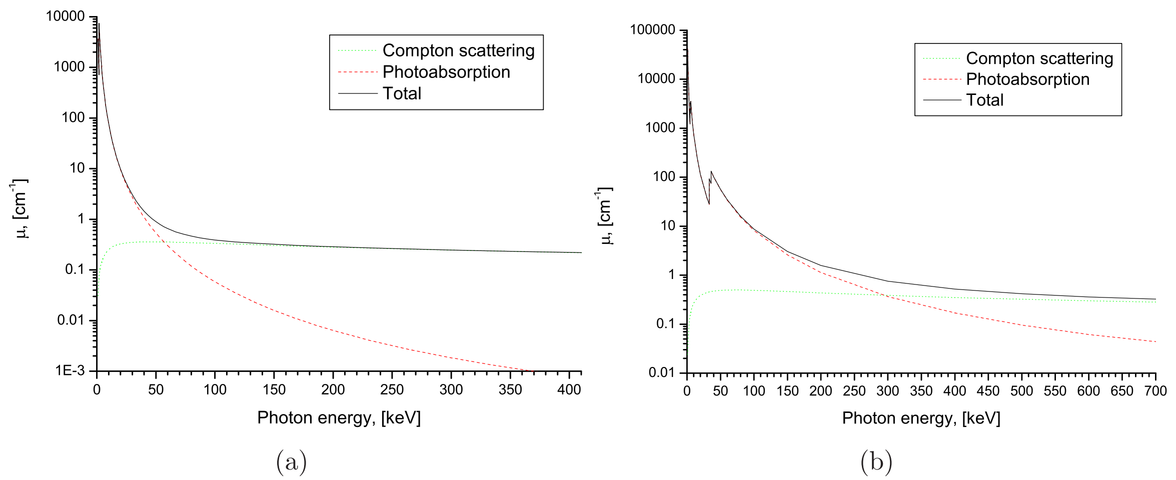

Figure 2.7: Linear absorption coefficients as a function of photon energy for a) silicon b) cesium iodide

2.2 Semiconductor detectors

Semiconductor detectors are very popular in high-energy physics, astronomy and medical physics applications because of their superior energy and spatial resolution, and also an excellent response time. Properties of some selected semiconductors together with the description of basic detector structures will be given in the following sections.

2.2.1 Semiconductors

Energy bands

In a crystalline solid, where many closely spaced atoms form a periodic lattice, electron wavefunctions of single atoms overlap building common energy states. Because of the Pauli principle, which forbids more than one electron in the same state, the energy levels of the valence electrons split themselves into many discrete levels. The separation between these levels is so small that they may be considered as a continuum, which is called an

energy band. One have to distinguish between the conduction band, which is the highest energy band, and the band next to it - the valence band. The region of forbidden states between them is called the band gap. Electrons in the conduction band can freely move throughout the crystal, the electrons in the valence band, however, are bound to their respective lattice atoms.

The width of the gap determines electrical behaviour of the solid: if the gap is of several electronvolts the solid acts as an insulator, if it is around one electronvolt - as a semiconductor and if the bands overlap - as a metal. At low temperatures in a semiconductor all the electrons are bound to their corresponding lattice atoms; it means that the valence band is completely filled and the conduction band is free, the semiconductor behaves as an insulator. As the temperature increases, approaching room temperature, the electrons can be excited into the conduction band by the thermal energy. Every excited electron leaves a *hole* in the valence band. A neighbouring electron can jump in the holes place leaving hole in its original position. It appears as a motion of a positive charge carrier through the crystal, which is also contributes to the electric current. Thus at room temperature semiconductors possess a weak conductivity due to both free electrons and holes.

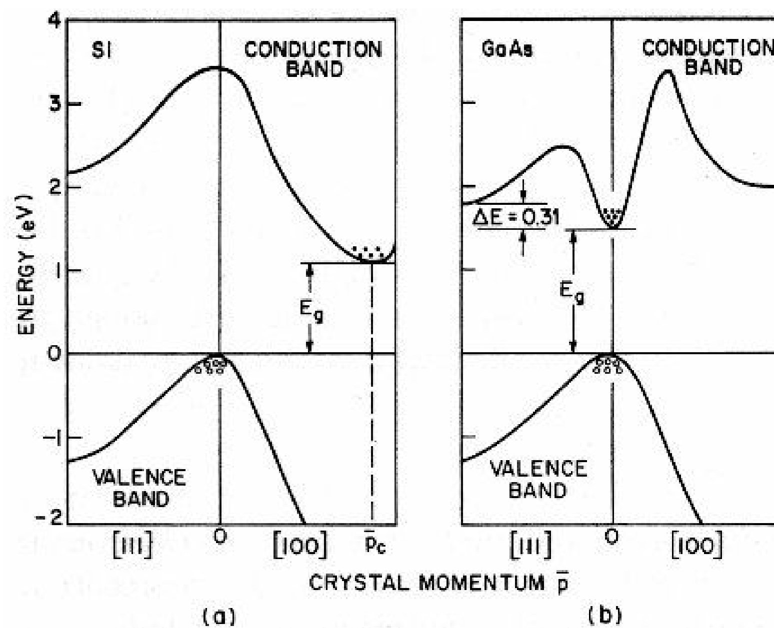

Figure 2.8: Energy band structure of a) silicon b) gallium arsenide(after [Sze85])

Energy band structures of two semiconductors often used as detectors materials - Si and GaAs are shown in Figure 2.8 as a function of the crystal momentum $\vec{p}$ in two specific(111 and 100) crystal directions. One can see that for GaAs, unlike to Si, the minimum of the conduction band is located directly above the maximum of the valence band, which is a criterion of the differentiation between direct and indirect semiconductors. This difference becomes important when generation or recombination of charge carriers is considered: indirect semiconductors require additionally a momentum transfer to the

crystal lattice during the band-to-band transitions of the carriers. This reduces significantly the probability of such transitions and therefore recombination and generation are normally occurs in two steps, involving intermediate energy states in the band introduced by impurities[Sze85,Kit96].

Intrinsic and extrinsic semiconductors

Semiconductors, which contain very few impurities comparing with the number of thermally generated electron-hole pairs, are classified as *intrinsic*, otherwise as *extrinsic* semiconductors. Practically it is very difficult to obtain a very pure semiconductor, instead, small amounts of specific impurities are intentionally added to the semiconductor to change it properties. This procedure is called doping and will be considered now for the case of silicon.

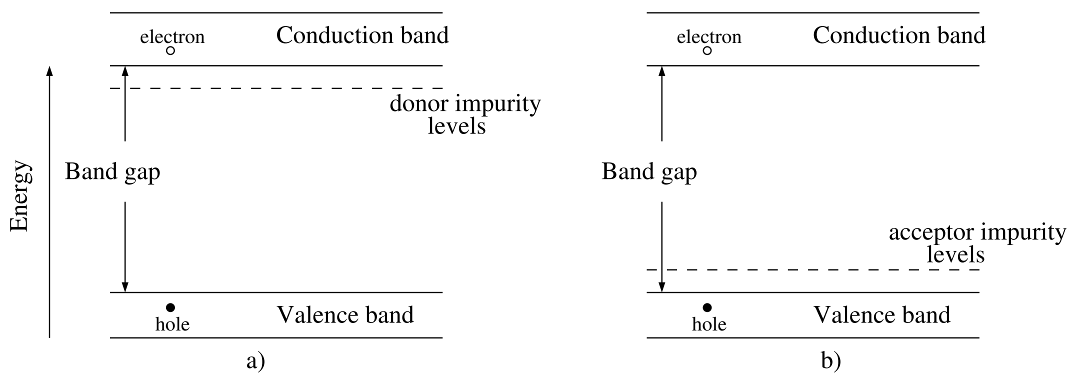

Figure 2.9: Band structure of an extrinsic semiconductor of a) p-type b) n-type

Silicon has four valence electrons, which form four covalent bonds with electrons of the neighbouring, also silicon, atoms. If a dopant has five electrons(such as phosphorus), one of its electrons will not be covalently bonded and can contribute to conduction. Thus the material with excess of electrons is formed, which is also called *n-type* semiconductor; the dopant is known as a *donor*. In the case of the dopant with three electrons(e.g. boron) one electron will be missing in the covalent bond and thus a hole is created. In this kind of material(*p-type* semiconductor) the current will be mainly due to the movement of holes; the dopant is referred to as a *acceptor*. Doping with impurities changes the energy band diagram as shown in Figure 2.9. As can be seen, intermediate states in the band gap are created: in the case of donor impurities - close to the bottom of the conduction band(Figure 2.9a), in the case of acceptors - close to the top of the valence band(Figure 2.9b). At room temperature impurity levels are almost completely ionised - electrons from donor levels will be transported in the conduction band and electrons from the valence band will fill acceptor states leaving holes in the valence band.

Properties of selected semiconductors

Properties of some useful intrinsic semiconductor materials, taken from [Lut99, Sze81, Sat02], are listed in Table 2.1. It should be noted, however, that these data can slightly

Substance	Si	Ge	CdTe	Diamond
atomic number	14	32	48..52	6
atomic mass	28	73	120	12
density,[g/cm^3]	2.3	5.3	5.9	3.5
bandgap @300K, [eV]	1.12	0.66	1.52	5.47
optical transition	indirect	indirect	direct	indirect
mean energy for electron-hole pair creation, [eV]	3.63	2.96	4.49	13.1
dielectric constant	11.9	16.2	9.7	5.7
electron mobility, [cm^2/Vs]	1450-1500	3800-3900	1050	1800
hole mobility, [cm^2/Vs]	450-500	1800-1900	100	1200-1600
Fano factor	0.12	0.13	0.15	0.08

Table 2.1: Intrinsic properties of selected semiconductors

differ depending on production technology.

2.2.2 p-n junction

The most useful structure is a p-n junction which is formed by joining together semiconductors of p- and n-type, e.g. by diffusion of the sufficient number of acceptor impurities into one end of an n-type bar. Because of the difference in the concentration of holes and electrons on the both sides of the junction the electrons from the n-region will diffuse into the p-region and fill up holes there, while diffusing holes will capture electrons in the n-region. Thus close to the junction a zone without free charge carriers is formed, known as the *depletion* zone or *space charge region*. In this zone only ionised atoms of impurities are present, positive on the n-side and negative on the p-side. This creates an electric field across the junction which diminishes the tendency for further diffusion. The potential difference across the junction, caused by the electric field, is known as a contact or a build-in potential V_{bi}. The build-in potential is generally on the order of 1V. Depletion region is appropriate for use as a detection medium, since charge carriers, generated in this region, will be swept out by the electric field, before they recombine.

A p-n junction in thermal equilibrium is shown in Figure 2.10a, where N_A is the concentration of acceptor atoms in p-region and N_D - the concentration of donor atoms in n-region; $N_A > N_D$. Charge distribution across the junction[3] is given in Figure 2.10b; distributions of electric field and electric potential across the junction[Sze81] are calculated by solving of Maxwell's equations and shown in Figure 2.10c and Figure 2.10d, respectively.

If an external voltage is applied to the junction the thermal equilibrium breaks. One have to distinguish between two possibilities of the voltage application. If a positive voltage is applied to the p-side with respect to the n-side it is referred to as a forward

[3] a uniform charge distribution in the depletion region with an abrupt change of charge concentration is considered for simplicity

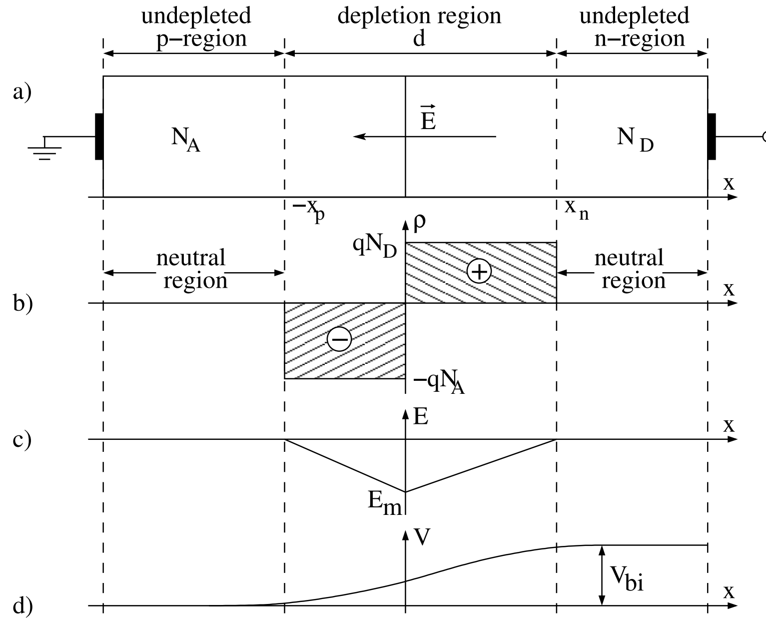

Figure 2.10: a) p-n junction at equilibrium; b) distribution of charge across the junction; c) distribution of electric field across the junction; d) distribution of electric potential across the junction

bias, if a positive voltage will be applied to the n-side the junction will be biased in the reverse direction. The forward bias will diminish the build-in potential barrier, allowing majority carriers cross the junction. If a reverse bias voltage V_{bias} is applied, the potential barrier grows and the width of the depletion layer d, given by equation 2.10[Leo93], increases:

$$d = \sqrt{\frac{2\epsilon\epsilon_0(N_A + N_D)}{qN_AN_D}(V_{bi}+ \mid V_{bias} \mid)} \tag{2.10}$$

where ϵ_0 is permittivity of vacuum and ϵ- dielectric constant of semiconductor material. Practically a pn-junction is made strongly asymmetric and therefore with application of reverse bias voltage the depletion region extends only in one direction. For a p^+-n junction, $N_A \gg N_D$, and equation 2.10 reduces to:

$$d \approx \sqrt{\frac{2\epsilon\epsilon_0}{qN_D}(V_{bi}+ \mid V_{bias} \mid)} \tag{2.11}$$

Because the depleted volume of the junction is free of mobile charges it exhibits some properties of a charged capacitor. The value of its capacitance per unit area $C = \epsilon\epsilon_0/d$ decreases with increasing reverse bias voltage.

2.2.3 Reverse biased p^+-n junction as a radiation detector

A radiation detector formed by a highly doped p^+ implantation on a lowly doped n-substrate is shown in Figure 2.11a. An additional n^+ layer provides a good ohmic con-

tact[Sze81] between the metal and the semiconductor. The p^{+}-n junction is reverse-biased with the voltage V_{bias}, sufficient to fully deplete the detector volume. The distributions of electric field and electric potential across the detector are shown in Figures 2.11b and 2.11c, respectively. Ionising radiation, entering the depletion region, generates electron-hole pairs which drift very fast in the electric field toward the electrodes. In the considered case the hole current, proportional to the absorbed energy, is sensed with a preamplifier for a further signal processing.

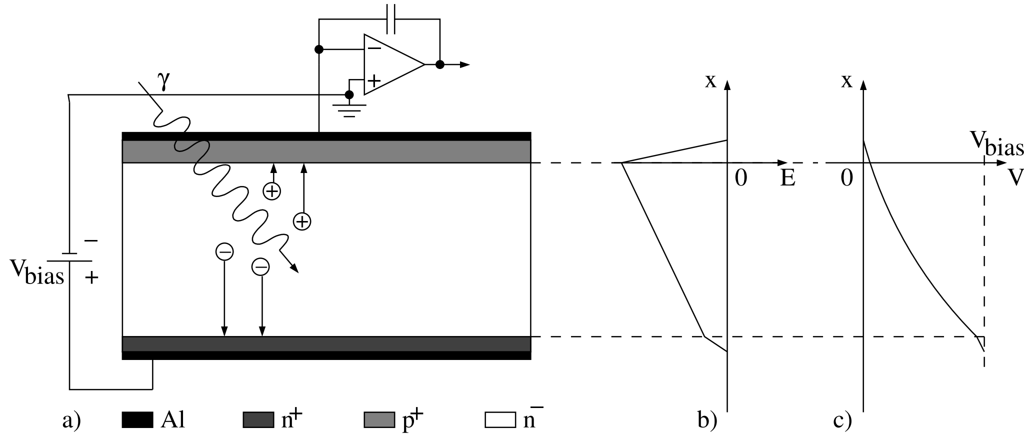

Figure 2.11: a) Reverse biased p^{+}-n junction as a radiation detector. Distributions of b) electric field and c) electric potential across the detector

From equation 2.11 with the assumption $|V_{bias}| \gg V_{bi}$ the bias voltage, required to fully deplete the detector, can be determined.

$$V_{bias,dep} \approx \frac{qN_D}{\epsilon\epsilon_0}\frac{d_{det}^2}{2} \tag{2.12}$$

For a typical silicon detector of a $300\mu m$ thickness and with a substrate doping concentration of $10^{12}cm^{-3}$ the full depletion voltage is ≈68V. The value of the detector capacitance per unit area can be found from:

$$C = \frac{\epsilon\epsilon_0}{d} \approx \sqrt{\frac{\epsilon\epsilon_0 qN_D}{2\mid V_{bias}\mid}} \tag{2.13}$$

One can see that detector capacitance decreases with applied bias, which is useful in design of low noise electronics(see Chapter 4). Also measuring the capacitance versus bias voltage characteristic the doping concentration of substrate can be found. For fully depleted, $300\mu m$ thick detector $C \approx 35pF/cm^2$, which for a pixel size of $200\mu m \times 200\mu m$ results in 14fF detector capacitance. [4]

[4] In reality it is only a small part of the total detector capacitance since the latter is dominated by a coupling capacitance to neighbouring pixels

2.2.4 Punch-through bias structure

To perform a correct test of a pixel detector prior to the bonding to usually much more expensive readout electronics, all detector pixels must be contacted as during the operation, to ensure a homogeneous electric field distribution in the detector material. Having hundreds of pixels this test cannot be done with a probe station. Therefore in modern detectors a special punch-through bias network is integrated into the sensor structure; it consists of additional implants placed close to the pixels and connected together. The application of voltage to the network will bias also the pixels due to a punch-through effect[Sze81]. During the normal operation of the detector the punch-through structure is floating and does not affect the detector performance.

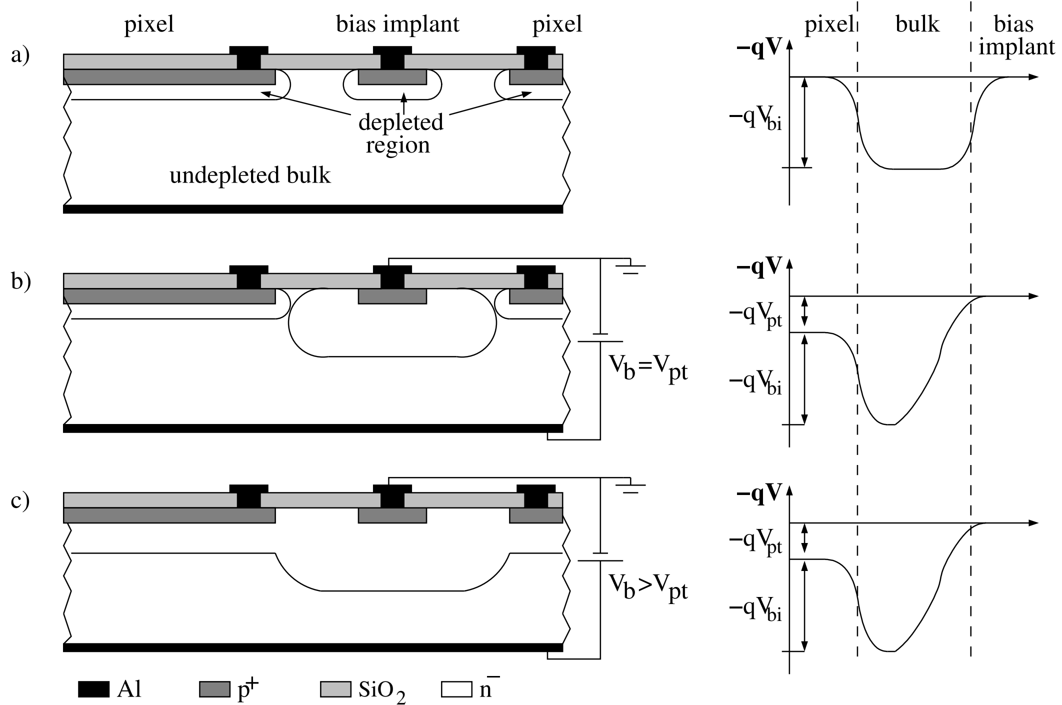

Figure 2.12: Principle of a punch-through biasing. Side view of the detector and potential distribution near the surface for a) unbiased detector, b) reverse bias equal to the punch-through voltage and c) reverse bias larger than the punch-through voltage.

The functionality of this bias mechanism is explained with the help of Figure 2.12, where a small part of the detector consisting of a punch-through bias implant(contacted) and two neighbouring pixels(floating) is considered. For the unbiased detector the natural depletion regions under the pixel and the bias implants are separated, as shown in Figure 2.12a; the potential difference between the bulk and the implants is V_{bi}. With the application of a reverse bias voltage the depletion region under the bias implant extends also laterally and at some voltage V_{pt} it touches the depletion region under the pixels; one speaks about an onset of a punch-through condition(Figure 2.12b). The value of the punch-through voltage V_{pt} depends on the bulk doping, oxide charge density and the distance between the pixel and the punch-through bias implant.

With the further increasing of the reverse bias the potential of the pixels remains unchanged and close to V_{pt}; the depletion region extends also under the pixel implants, as shown in Figure 2.12c. In this way the whole detector volume can be depleted, which makes possible the measurement of the total leakage current.

If the pixel will be additionally biased with a voltage larger than V_{pt} the pixel-bulk junction becomes forward biased. Holes from the pixel implant, injected into the n-bulk by means of thermionic emission, will drift towards the bias implant. The current will rise exponentially if the applied voltage will be further increased.

2.2.5 Multiple guard ring structure

Reverse bias voltages up to several hundreds volts have to be applied to p^+n-detectors to achieve a full depletion. With such a high bias some precautions have to be met to provide proper operation of detectors and to protect them from a breakdown. The p^+-implant has to be kept far away from the cutting edge to prevent short circuit of the detector. Also if the depletion zone reaches the detector edge the reverse current will significantly increase because of the enhanced charge generation rate in the heavily damaged crystal lattice. But a simple removal from the edge does not guarantee a stable long term operation of the detector, since other effects, such as, e.g., the accumulation of charge on the oxide surface, can help to extend the depletion zone up to the edge. Therefore there is a need in a protection structure integrated on the sensor.

Such a protection structure, called a multiple guard ring structure, consists of several floating, ring-shaped p^+ implantations, which surround the sensitive detector area. The outermost ring is biased to the backside potential whereas the innermost guard ring is held at the same potential as the sensitive area. Other rings, which bias themselves via the punch-through mechanism, described in previous section, provide a gradual voltage drop between these two rings. To save the total detector area the protection structure has to be optimised to have the largest possible voltage drop between two neighbouring rings. This drop, the punch-through voltage V_{pt}, depends on the ring spacing and a metal overlap.

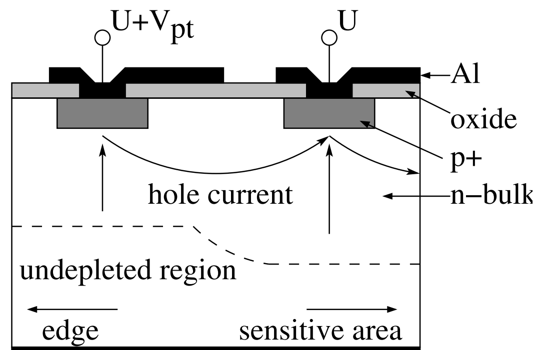

Figure 2.13: Structure of two neighbouring guard rings

The structure of two neighbouring guard rings is shown in Figure 2.13. The metallisation of the external ring extends up to the middle of the gap between the rings in order

to increase the punch-through voltage. Indeed, the potential barrier near the surface (see Figure 2.12) will be larger, suppressing the hole current, which has to flow now deeper in the bulk. Also the electric field density at the edge of p^+-implantation will be minimised, which prevents an excessive avalanche generation of carriers leading to the breakdown of the detector. With such a structure the voltage drop up to 40V between two rings can be achieved[Bis93].

2.2.6 Intrinsic energy resolution of semiconductor detectors

As was discussed in sections 2.1 and 2.2 charged particles and gamma radiation interact with a detector material by means of inelastic collisions, i.e. transferring energy to it. The energy, deposited in the semiconductor, is shared between ionisation, i.e. creation of electron-hole pairs, and exiting of lattice vibrations(phonons). The fraction of energy that goes into ionisation is an intrinsic property of the detector material, independent of the type of radiation.

The average number of electron-hole pairs N generated by the absorbed energy E is given by

$$N = \frac{E}{w} \tag{2.14}$$

where w is the mean energy required to create one electron-hole pair. Since the energy sharing process is random, there is a fluctuation in the number of created electron-hole pairs. The variation of this number is given by the following formula[Lut99]:

$$< \Delta N^2 >= F \cdot N = F\frac{E}{w} \tag{2.15}$$

where F is a Fano factor, which reflects deviation of the observed statistical fluctuations from the pure Poisson statistics. For semiconductors the Fano factor is considerably less then unity.

2.3 Scintillation detectors

Scintillation detectors are one of the oldest and widely used detectors in particle physics, astronomy and medical physics. They consist basically of a scintillation material, which converts absorbed energy into light, usually visible, and a light detector. Functionality and properties of some selected scintillators together with the description of light detectors will be given in the following sections.

2.3.1 Scintillators

Incident radiation, photons or particles, excite atoms and molecules of the scintillator material. The excited states decay by emitting a flash of light, i.e. scintillation. This property of the reemission of absorbed energy in form of visible light is known also as a *luminescence*. If the reemission occurs within tens of nanoseconds after the absorption, the process is called a *fluorescence*; if it takes longer the process is known as a *phosphorescence*. An ideal scintillator should possess a high scintillation efficiency, be transparent to its

own fluorescence radiation and have a short decay time constant. From the variety of scintillator materials two large groups, namely organic and inorganic scintillator materials, will be briefly described.

Organic scintillators

The fluorescence mechanism in organic scintillators is connected with transitions between the energy levels of individual molecules, therefore it is independent of the physical state of the scintillator. Organic scintillation materials have decay times in the order of a few nanoseconds or less. They are usually a mixture of several components: to the primary fluorescence agent, which is excited by a radiation, small amounts of other fluorescence agents are added. It can be done, for example, if there is a need to increase efficiency for a particular type of radiation. Also if the primary agent is opaque for its own light or if its light emission spectrum have to match better the light absorption spectrum of a detector a *wavelength shifter* is added. This agent absorbs the light from the primary one and reemits it at another frequency. All components of the mixture are normally dissolved in an organic liquid or in a solid plastic solvent. Plastic organic scintillators of any size and form can be easily made, which offers a tremendous flexibility in use.

Inorganic scintillators

Inorganic scintillation materials are mainly crystals and possess a regular lattice, therefore their operation principle can be understood by considering their band structure, shown in Figure 2.14. These materials are insulators with a band gap of about 5-10eV, completely filled valence band and almost empty conduction band. Incident radiation loss its energy by means of two processes. Firstly an electron from the valence band can be excited to the conduction band, producing an electron-hole pair. Secondly an *exciton* can be created if an electron is excited to a band(the exciton band) located just below the conduction band. In this case the electron and the hole left in the valence band becomes electrostatically bound, but can freely move together throughout the lattice.

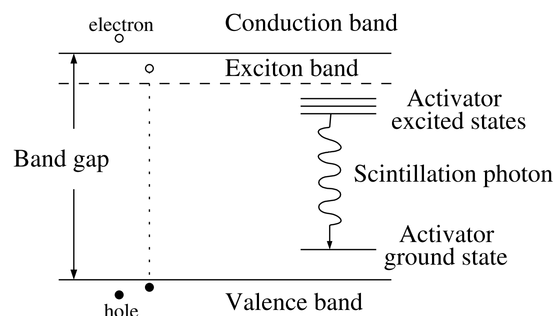

Figure 2.14: Band structure of an inorganic scintillator

A direct recombination of free electrons with holes by emitting radiation is possible but inefficient; also the energy of the radiation is larger than that of visible light. Therefore inorganic crystals are usually doped with impurities (so-called *activators*), creating

intermediate energy levels in the forbidden band. A free hole from the valence band or from an exciton can ionise activator atom, an electron from the conduction band can drop into free place and make a transition from the excited state to the ground state of the activator. If this transition is allowed a scintillation light is emitted, otherwise electron becomes trapped and its energy goes into other processes. Life time of the exited states determines the decay time of the scintillator, which is of several hundreds nanoseconds for the most inorganic scintillators - considerably longer than that for organic scintillators. The main advantage of inorganic scintillators is their greater stopping power due to their higher atomic number and higher density. Also they exhibit a very high light output, which results in a better energy resolution.

Material	ρ, $[\frac{g}{cm^3}]$	Z_{eff}	L,$[\frac{photons}{MeV}]$	τ_d, [ns]	β	S	Q	η
NaI(Tl)	3.67	51	38000	230	0.88	0.59	1.0	0.52
CsI(pure)	4.51	54	2000	16	0.97	$\approx$0.29	0.10-0.15	0.029
CsI(Tl)	4.51	54	65000	800	0.97	0.99	1.0	0.96
Lu_2SiO_5(Ce)	7.4	66	40000	40	-	-	1.0	< 0.55
$Bi_4Ge_3O_{12}$	7.13	75	8200	400	0.69	$\approx$1	0.13	0.094

Table 2.2: Properties of some inorganic scintillation materials, taken from [Lem93], where ρ - density, Z_{eff} - effective atomic number, L - light yield, τ_d - decay time, β - conversion efficiency, S - transfer efficiency, Q - luminescence quantum efficiency, η - total scintillation efficiency.

Properties of several common inorganic crystals at room temperature are given in Table 2.2. The overall quantum efficiency of a scintillation process, η, is given as a product of three parameters β, S and Q. Each parameter represents the efficiency of one of three consecutive steps of the process: β - the efficiency of conversion of incident energy into electron-hole pairs, S - the efficiency of excitation of activation centres by electrons and holes, Q - the quantum efficiency of activation centres.

Considering CsI one can see from Table 2.2 how doping with thallium(Tl) affects its performance. Its total scintillation efficiency becomes almost one, which results in the enormous increase of light output. But also the decay time becomes relative long - $0.8\mu s$.

Cesium iodide crystals are soft, which makes them less sensitive to thermal and mechanical shocks. CsI is less hygroscopic than NaI, and therefore do not have to be housed in a tight enclosure for protection from ambient atmosphere. Doped with thallium CsI shows the best light yield among scintillation materials. The only drawback is its long decay time, which make impossible the use of CsI(Tl) in applications where a high rate of events is expected.

2.3.2 Detection of scintillation light

Basically there are two kinds of light detectors: photomultiplier tubes(PMTs) and photodiodes.

Photomultiplier

In a photomultiplier incident light is absorbed in a thin photocathode layer, liberating photoelectrons. Every photoelectron is directed and accelerated by a high electric field in a multiplier section of the PMT, so that an electron cascade is created. This cascade is collected at the anode of the photomultiplier, which is also the output of the device. All parts of the PMT are housed inside a vacuum tube.

Large amplification(up to 10^7), large active area, low noise and fast rise time are the advantages of PMTs. From the other side they are bulky and require a high voltage in the order of 1keV for operation. An another important drawback is a low quantum efficiency of PMTs, typically 25%[Ren04].

Photomultiplyers are used for example in an Anger camera, shown in Figure 3.1, to detect the light coming from a large NaI scintillation crystal. Required position information is obtained by comparing relative pulse heights of signals from several photomultipliers.

More detailed description of photomultipliers can be found in a standard literature[Kno79, Leo93].

Photodiode

A photodiode is basically a depleted semiconductor with an applied electric field where electron-hole pairs, generated by incident light, are separated. Thus the photodiode can be made from a reverse biased p^+-n junction described above. Because of low energy of visible light photons(a photon of 550nm wavelength has an energy of 2.26eV) their penetration depth is also low. Therefore p^+ layer has to be made very thin to transmit the light to the sensitive, depletion region. The thickness of the depletion region and the band gap of semiconductor material determine the spectral quantum efficiency of a photodetector. A silicon photodiode can have a quantum efficiency of up to 85% is the whole range of visible light[Rem04].

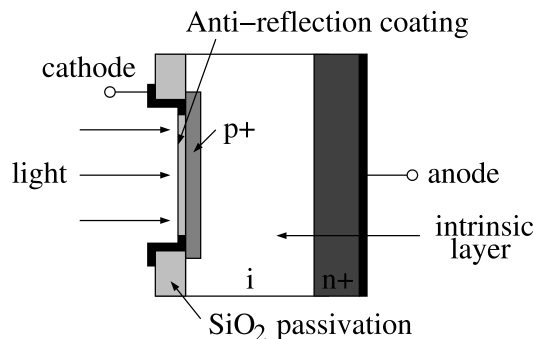

Figure 2.15: Structure of a silicon PIN photodiode

The most useful photodiode is a silicon PIN photodiode, shown in Figure 2.15, which consist of a p^+ implantation deposited on a substrate made of high-resistivity very pure n-type silicon, almost intrinsic. An anti-reflection coating, a thin film of silicon dioxide, have to be used, since otherwise about 33% of light would be reflected from a semiconductor

surface. The big advantage of the PIN photodiode is that its properties, such as quantum efficiency and response time, can be easily adapted to individual needs by changing the thickness of the intrinsic layer. From the other side the PIN photodiode has no gain and therefore needs a charge-sensitive amplifier for signal processing, which introduces additional noise.

Chapter 3

Compton camera prototype

In the nuclear medicine radioactive substrates are injected in the patient's body for diagnostic purposes. Depending on their biochemical or physiological properties they will localise in specific organs. For example, iodine(e.g. ^{131}I) will be collected in the thyroid gland where thyroid hormone, responsible for the control of metabolic rate of the body, is produced. The most useful radiopharmaceutical is ^{99m}Tc because of its excellent properties. It is a pure gamma emitter, which reduces local dose given to a patient. The photon energy of 140.5keV is large enough to suffer from attenuation inside of the body and small enough to be good collimated. It also have a half-life of six hours which keeps small the overall dose given to a patient. All further calculations will be done considering the use of this isotope.

By taking the image of agent distribution in the organ of interest one can find there any abnormalities. The image is taken by the detecting photons coming from the radioactive substrate within the body. Originally a scan method was employed for image acquisition. It was gradually replaced with a gamma camera, which has an advantage of having a full field of view. This camera, shown in Figure 3.1, was invented by Anger[Ang58]. It utilises a large area scintillator crystal optically coupled with an array of photomultiplier tubes, which allows to locate the position of interactions inside the crystal. A lead collimator perforated with many parallel holes is placed in front of the camera, so that only γ's coming from a particular direction can be detected. It allows a convenient direct imaging on the cost of low sensitivity and a high radiation dose that has to be given to a patient to obtain a good quality image. The patient has to be placed as close to the camera as possible; position resolution as small as 3mm can be achieved. A three dimensional picture can be created by rotating detectors around the patient's body and recording events at each detector location. This procedure is referred to as a SPECT.[1]

To increase sensitivity and thus to give a patient a lower radioactivity dose a Compton camera concept is proposed. The idea is to replace the collimator with an another position-sensitive detector, where emitted γ's undergo a Compton scattering before they will be fully absorbed. This is also referred to as an introducing of an *electronic* collimation instead of a mechanical(lead) collimation. By measuring energy and position of events in both detectors and assigning them by a coincidence scheme the origin of incident photons can be located. It lies on a surface of a cone with the apex at the scattering point, the

[1]Single Photon Emission Computer Tomography

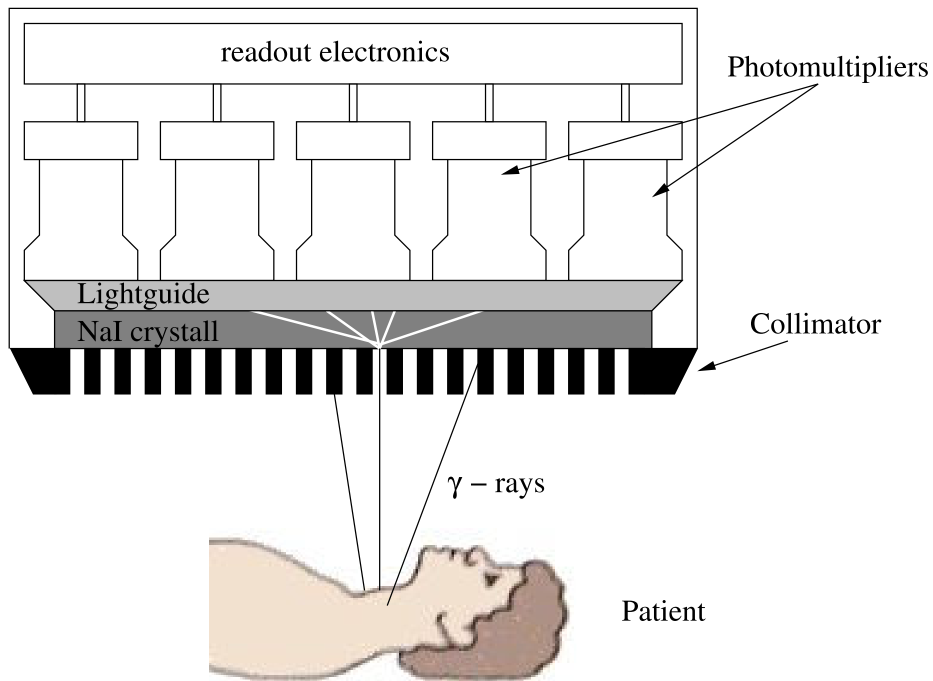

Figure 3.1: Principle of the Anger camera

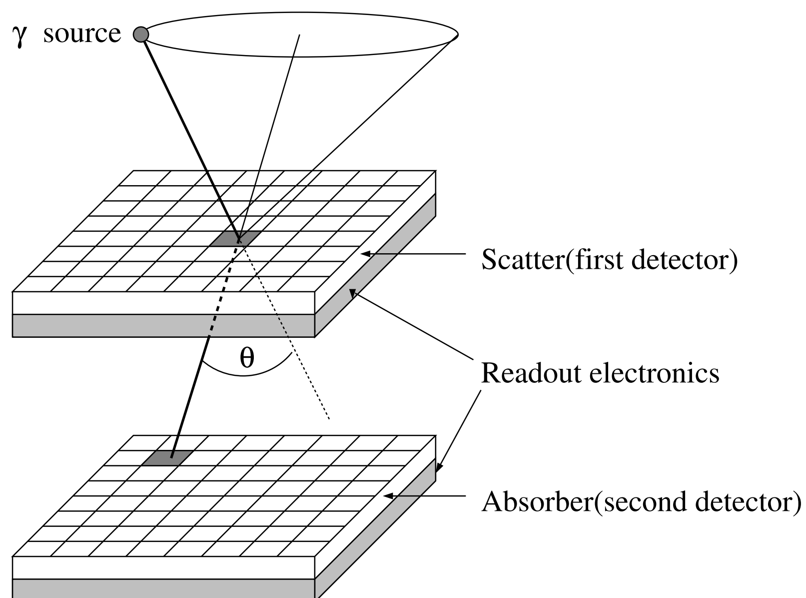

Figure 3.2: Principle of the Compton camera

axis defined by the line drawn through the interaction points and the half-angle equal to the scattering angle, as shown in Figure 3.2. Thickness of the cone shell is determined by the error in the calculated scattering angle. Knowing the distance between the camera and the organ, the source position can be reconstructed from the intersection of many such cones.

From equation 1.1 which assumes the struck electron unbound and at rest the half-angle of cone for one single Compton camera event can be found from the following relation:

$$cos\Theta = 1 - \frac{m_e c^2 E_{e^-}}{E_\gamma (E_\gamma - E_{e^-})} \tag{3.1}$$

where E_γ is initial photon energy, E_{e^-} is the energy of the recoil electron measured in the first detector. With E'_γ being the energy of the scattered photon, measured in the second detector, the condition $E'_\gamma + E_{e^-} = E_\gamma$ must be fulfilled.

By taking initial momentum of the struck electron into account a more complicated dependence arises, where for each scattered photon energy there is a diversity of scattering angles. This phenomenon is referred to as Doppler broadening and will be discussed in detail later in this chapter.

It is noted that by measuring the direction of motion of the recoil electron the reconstruction procedure can be greatly simplified, since then the location of possible photon origins can be reduced to a cone fragment. Unfortunately the measurement is possible only with sufficiently higher energies of incident photons. As an example, in the astrophysical experiment MEGA[Kan04], detecting γ's of 0.5-50 MeV energy, a stack of Silicon strip detectors is used to track recoil electrons.

3.1 Choice of the detectors

Both the first and second detectors have to be carefully selected to construct a Compton camera prototype which can compete with existing Anger cameras. Of great importance is also an advance in the detector technology for available detector materials, since it affects the detector quality and dimensions; the production costs play also an important role. Prior to the selection the energy range of incident photons have to be specified; the range of 140.5-364.5keV is considered.

3.1.1 Scatter detector

The probability for a photon to undergo a single Compton scattering is proportional to the atomic number Z of the scattering medium; at the same time the probability for a photoabsorption is proportional to Z^5. Therefore a detector with low Z has to be chosen to have a greater part of scattered photons escaped after a single Compton interaction. Silicon(Z=14) is a good candidate, since Si-detectors provide excellent energy resolution at room temperature; they are widely available and also cheap. The pixellation of a Si-detector can be done very fine, so that its contribution to the overall position resolution of the camera can be neglected. As will be discussed in section 3.2.3, since the atomic

number of silicon is small the Doppler broadening, which worsens the energy resolution, is also small. Disadvantages of silicon are its low density and small atomic cross section for Compton scattering in the 20-100keV energy range. As a consequence, only about 1% of photons will undergo a Compton interaction in the detector with a typical thickness of $300\mu m$. Multiple layers of silicon detectors can help to overcome this problem.

Detection sensitivity can be increased by either placing the detector close to the patient's body or by enlarging the detector area; the choice of the method depends on the application.

In the current application a Si-pixeldetector was chosen as a scatter detector. It consists of an array of 24×24 quadratic pixels of 200 μm size and has the thickness of 280 μm. This detector[Hue01] was designed and produced in collaboration with the University of Dortmund for imaging purposes. In this work, hovewer, it was found that despite of a very low dark current, the detector has a poor isolation between the punch-through bias network and pixels and therefore its application is doubtful.

3.1.2 Photoabsorber

The photoabsorption detector has to fully absorb the scattered photon. Silicon, obviously, is not a good choice since it has a very low stopping power. Its absorption efficiency together with absorption efficiencies of other compound semiconductor materials is given as a function of incident photon energy in Figure 3.3a. Typical thickness of materials of $300\mu m$ was used in the calculations.[2]

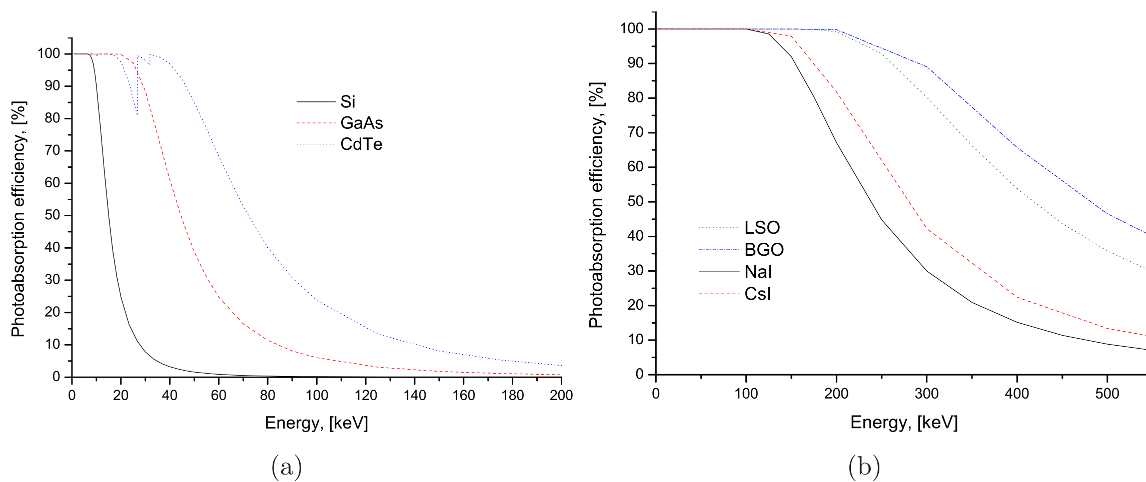

Figure 3.3: Photoabsorption efficiency as a function of energy[NIST04] for a) $300\mu m$ thick semiconductors b) 1.5cm thick scintillator crystals

One can see that even for CdTe only about 80% of 50keV photons will be detected. Also CdTe detectors are expensive and the detector technology is still under development.

[2]Larger thicknesses are also possible but other problems may arise since then a larger HV bias is required to fully deplete the detector. Because the outer guard ring is also biased with the high voltage a short between the detector and the bump-bonded electronics becomes probable.

This lead to searching for the alternatives such as, for example, scintillator crystals, which can be grown of almost any size. Photoabsorption efficiency for different scintillator materials, currently used in medical imaging applications, is shown in Figure 3.3b for the crystal thickness of 15mm. One can see that much more better stopping power can be achieved. The drawbacks are unavoidable losses due to indirect conversion of the photon energy into electron-hole pairs and difficulties with the light collection; both these factors worsen the energy resolution.

From the existing available scintillator detection systems that could be adapted as a photoabsorber in the Compton camera prototype the CsI detector[Sch00] from the MEGA experiment in astrophysics drew our attention. The detector consists of an array of 10×12 CsI(Tl) crystals of $5mm \times 5mm$ section read out by silicon PIN photodiodes. In the MEGA experiment the length of the crystals was chosen to absorb photons with the energy of several MeV; for our purposes shorter crystals of 15mm length were used instead. After manual polishing of the crystals the detector was assembled at the MPI for Extraterrestrial Physics.[3] More detailed description of the CsI detector and its performance will be given in Chapter 6.

3.2 Position uncertainty

In this section various factors, which have an influence on the position resolution of the reconstructed source will be considered. To this factors belongs first of all the energy resolution of the scatter detector, which is worsened at low energies by a Doppler broadening due to the motion of electrons. Also the arrangement of the Compton camera prototype, which defines the position of detectors relative to the patient's body and to each other and their dimensions, has impact on the resolution. Contribution of each factor to the total resolution will be given as FWHM of the uncertainty in the scattered angle $\Delta\theta_{FWHM}$. Position uncertainty can be easily found then by knowing the distance z_1 between the source and the detector: $\Delta x_{FWHM} = z_1 \cdot tan(\Delta\theta_{FWHM})$.

[3] Max Planck Institute for Extraterrestrial Physics, 85741 Garching, Germany

3.2.1 Geometry considerations

Uncertainty in the angular resolution due to geometrical factors depends on the following parameters:

- a_1 - position resolution of the first detector
- a_2 - position resolution of the second detector
- t_1 - thickness of the first detector
- z_1 - distance between the source and the first detector
- z_2 - distance between the detectors

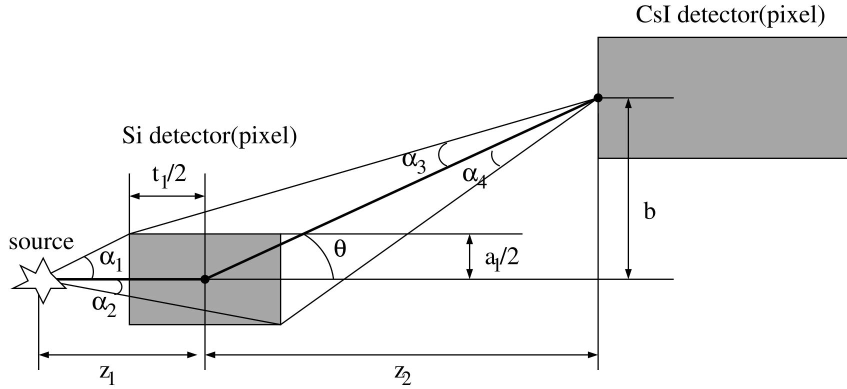

Figure 3.4: Impact of the first detector geometry on angular uncertainty

Impact of parameters of each detector can be found separately by solving of the system of simple trigonometric equations arising from Figure 3.4 for the first detector and from Figure 3.5 for the second, respectively. The following variables are introduced:

$$\Delta\theta_1 = \alpha_1 + \alpha_2 + \alpha_3 + \alpha_4 \quad b = z_2 \cdot tan\theta \quad d = \sqrt{z_2^2 + b^2} \tag{3.2}$$

with θ being the scattering angle, $\Delta\theta_i$ - uncertainty in the scattering angle due to the i-th detector. For $b > a_1/2$ the equations below take place:

$$tan(\alpha_1) = \frac{a_1}{2z_1 - t_1} \tag{3.3}$$

$$tan(\alpha_2) = \frac{a_1}{2z_1 + t_1} \tag{3.4}$$

$$tan(\theta - \alpha_3) = \frac{2b - a_1}{2z_2 + t_1} \tag{3.5}$$

$$tan(\theta + \alpha_4) = \frac{2b + a_1}{2z_2 - t_1} \tag{3.6}$$

By using of the standard trigonometric formula

$$tan(\theta \pm \alpha) = \frac{tan\theta \pm tan\alpha}{1 \mp tan\theta \cdot tan\alpha} \quad \text{, or} \quad tan(\alpha) = \frac{\pm(tan(\theta \pm \alpha) - tan\theta)}{1 + tan(\theta \pm \alpha) \cdot tan\theta} \tag{3.7}$$

expressions for α_3 and α_4 can be found:

$$tan(\alpha_3) = \frac{a_1 z_2 + t_1 b}{2d^2 - a_1 b + z_2 t_1} \tag{3.8}$$

$$tan(\alpha_4) = \frac{a_1 z_2 + t_1 b}{2d^2 + a_1 b - z_2 t_1} \tag{3.9}$$

And the angular resolution due to the geometry of the first detector is:

$$\Delta\theta_1 = arctan\Big(\frac{a_1}{2z_1 - t_1}\Big) + arctan\Big(\frac{a_1}{2z_1 + t_1}\Big) + arctan\Big(\frac{a_1 z_2 + t_1 b}{2d^2 - a_1 b + z_2 t_1}\Big) + +arctan\Big(\frac{a_1 z_2 + t_1 b}{2d^2 + a_1 b - z_2 t_1}\Big) \tag{3.10}$$

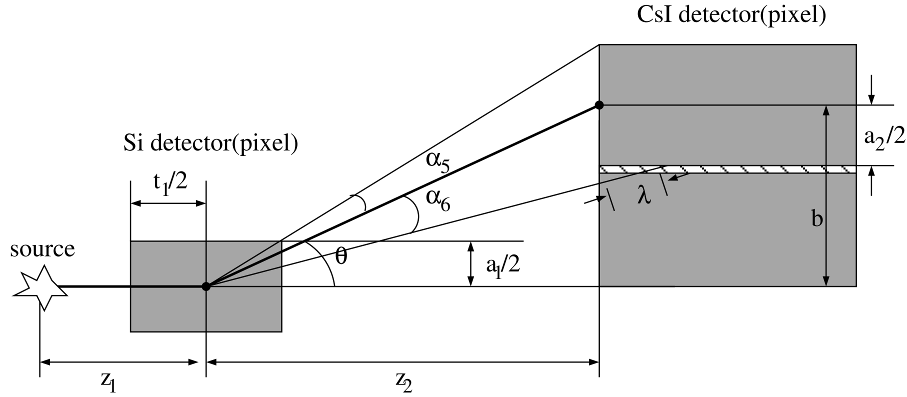

Figure 3.5: Impact of the second detector geometry on angular uncertainty

Impact of the geometry of the second detector leads to the following expressions:

$$tan(\theta + \alpha_5) = \frac{2b + a_2}{2z_2} \tag{3.11}$$

$$tan(\theta - \alpha_6) = \frac{b - a_2/2}{z_2 + \lambda cos(\theta - \alpha_6)} \approx \frac{2b - a_2}{2z_2} \tag{3.12}$$

with λ being a mean free path(reciprocal value of the total linear absorption coefficient) for photons with energy E'_γ. For the scattered photon energy of 150keV the λ in CsI is only about 0.33cm(see Figure 2.7a), which is considerably lower then the distance between detectors z_2. Therefore second term in the denominator of equation 3.12 was neglected.

By using of the formula 3.7 the angular resolution due to the geometry of the second detector is:

$$\Delta\theta_2 = \alpha_5 + \alpha_6 = arctan\Big(\frac{z_2 a_2}{2z_2^2 + 2b^2 + ba_2}\Big) + arctan\Big(\frac{z_2 a_2}{2z_2^2 + 2b^2 - ba_2}\Big) \quad (3.13)$$

Uncertainty due to the geometric factors in this configuration as a function of scattering angle is given in Figure 3.6 for the parameters of chosen detectors and with $z_1 = z_2 = 50mm$. Contribution of each of previously described detectors and also combined contribution of both $\Delta\theta_{geo} = \sqrt{\Delta\theta_1^2 + \Delta\theta_2^2}$ are shown there. It can be seen that the position resolution of the second detector dominates almost for all scattering angles in this configuration. On the contrary, the error due to the position of resolution of the first detector can be neglected. To reduce the effect of the second detector the camera have to operate with larger scattering angles; also the distance between the detectors can be reduced to cover larger range of scattering angles.

3.2.2 Energy resolution

In this subsection the impact of the energy resolution of the first detector on the calculated scattering angle will be estimated. Assuming an unbound electron at rest in scatter material one can take a derivative of equation 3.1 with respect to the scattering angle θ. The uncertainty in the scattering angle is then:

$$\Delta\theta = \frac{m_e c^2}{sin\theta(E_\gamma - E_{e^-})^2}\Delta E_{e^-} \quad (3.14)$$

where ΔE_{e^-} is the energy resolution of the scatter detector. It includes both the electronic noise and statistical variation in the number of generated electron-hole pairs. The first constituent can be made in principle very low, but the second represents a physical limit. For E_γ of 30keV the statistical component according to equation A.1 is ≈270eV, which together with $50e^-$ ENC noise(427eV) of electronics results in ΔE_{e^-} ≈0.5keV. For this energy resolution the variation of $\Delta\theta$ as a function of scattering angle is shown in Figure 3.7 for two different energies of incident photons. It can be seen that the angular resolution improves with source energy and the scattering range of 30-100° has to be chosen to keep the impact of the energy resolution small.

3.2.3 Doppler broadening

Equation 1.1 was derived under assumption that the struck electron is initially unbound and at rest. Non-zero pre-collision momentum of the electron gives rise to a variety of scattered photon energies E'_γ for a given initial photon energy E_γ and scattering angle θ. This effect is referred to as Doppler broadening. A doubly-differential cross section for scattering angle θ per differential solid angle $d\Omega$, per differential energy dE' was derived by Ribberfors[Rib75]:

$$\frac{d^2\sigma_s}{d\Omega dE'} = \frac{1}{2}m_e r_e^2\sqrt{E_\gamma^2 + E_\gamma'^2 - 2E_\gamma E'_\gamma cos\theta}\cdot\frac{E'_\gamma}{E_\gamma}\Big(\frac{E'_\gamma}{E_\gamma} + \frac{E_\gamma}{E'_\gamma} - sin^2\theta\Big)J(p_z) \quad (3.15)$$

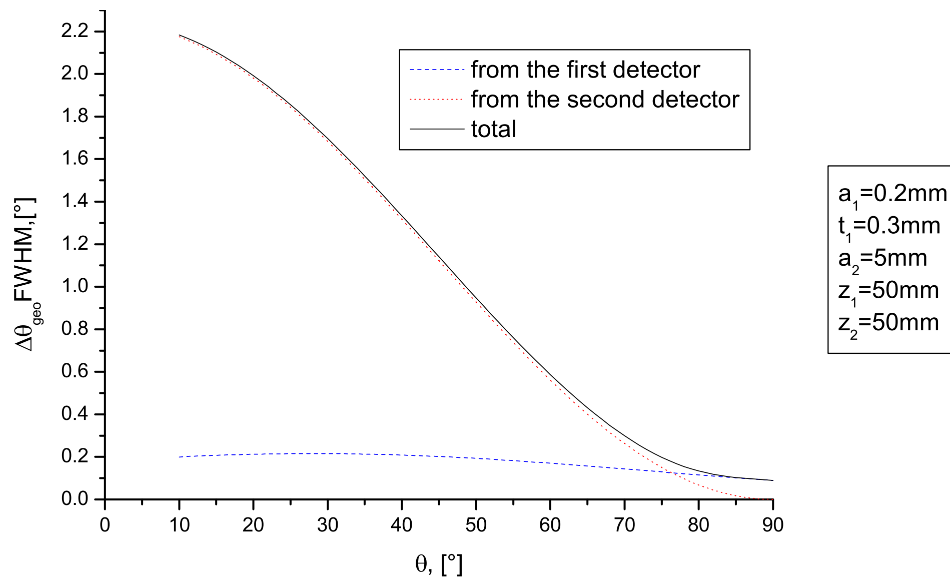

Figure 3.6: Angular resolution: impact of the geometry of detectors

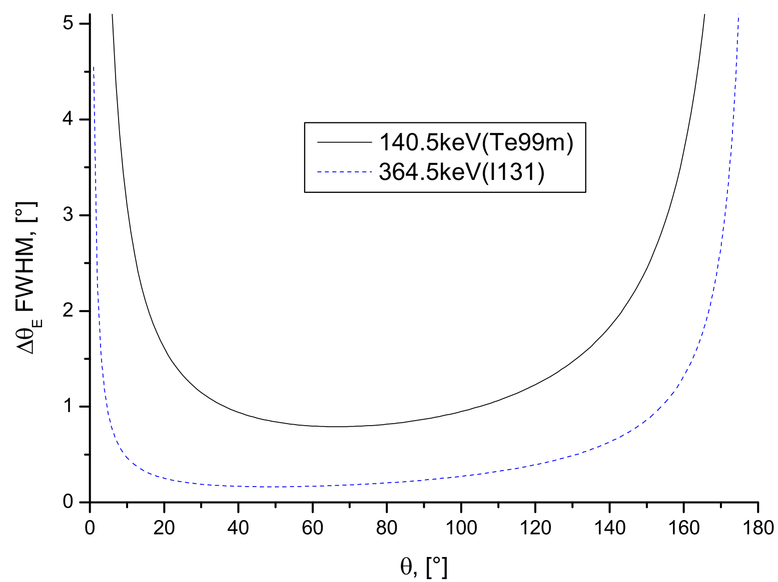

Figure 3.7: Angular resolution: impact of the scatter detector energy resolution

where $J(p_z)$ is the Compton profile of scattering material and p_z is the projection of initial electron momentum $\vec{p_e}$ onto photons momentum transfer vector $\vec{p_\gamma} - \vec{p'_\gamma}$ as shown in Figure 3.8.

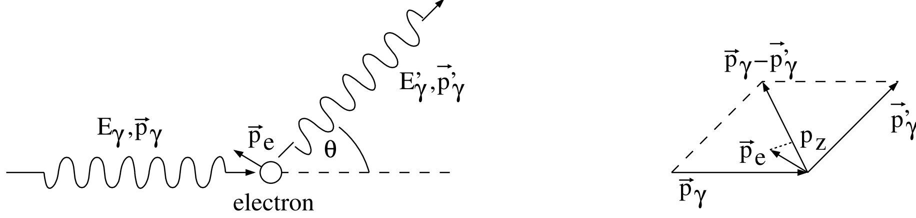

Figure 3.8: Compton effect with a vector diagram

From the energy and momentum conservation the following expression for p_z can be obtained[Mat89]:

$$p_z = \frac{E_\gamma E'_\gamma (1 - cos\theta) - m_e c^2 (E_\gamma - E'_\gamma)}{c\sqrt{E_\gamma^2 + E'^2_\gamma - 2E_\gamma E'_\gamma cos\theta}} \tag{3.16}$$

The Compton profile dominates the distribution given by equation 3.15 since other factors are approximately constant for given E_γ and θ. Therefore the intensity of scattered photons at any E'_γ is proportional to the probability of observing the corresponding momentum p_z, which is given by $J(p_z)$. This is an even function of p_z and have very narrow distribution around p_z=0, where it has a maximum. The Compton profiles for crystalline silicon, germanium and diamond were measured by Reed and Eisenberger[Ree72]; $J(p_z)$ for silicon is shown in Figure 3.9. One can distinguish between the contributions of electrons from inner and outer shells. More tightly bound electrons of inner shells cause greater broadening than four valence electrons, which show a narrow peak. It is noted that the broadening increases with atomic number since the number of possible momentum states also increases.

Differentiating equation 3.16 with respect to θ and taking p_z=0 gives rise to the following expression for the angular uncertainty:

$$\Delta\theta_d = \frac{\Delta p_z}{E_\gamma} \cdot c \cdot \frac{\sqrt{E_\gamma^2 + E'^2_\gamma - 2E_\gamma E'_\gamma cos\theta}}{E'_\gamma sin\theta} \tag{3.17}$$

The last factor, denoted as $f(E_\gamma, \theta)$, is almost constant over the range of $0 < \theta < 100°$ and nearly energy independent as can be seen in Figure 3.10. By taking $f(E_\gamma, \theta) \approx 1$ for ^{99m}Tc energy of 140.5keV and expressing errors of momentum and scattering angle in FWHM the following approximation arises:

$$\Delta\theta_{dFWHM} \approx \frac{\Delta p_{zFWHM} \cdot c}{E_\gamma} \tag{3.18}$$

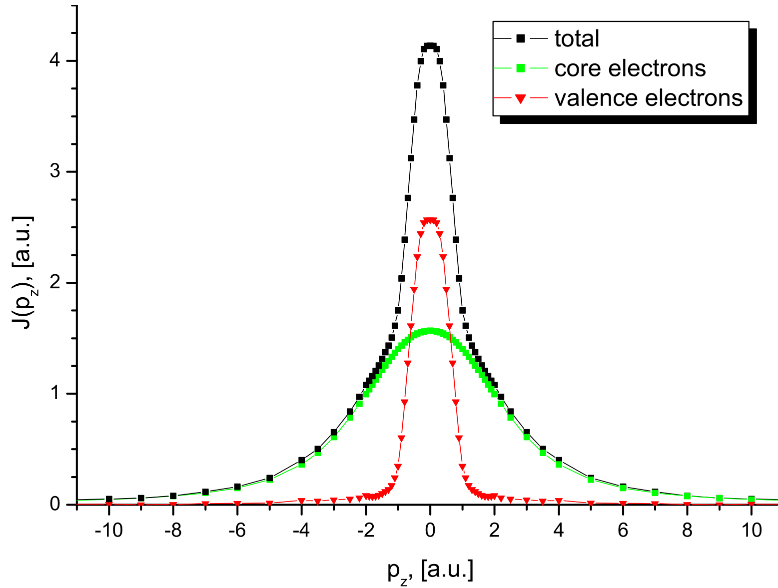

Figure 3.9: Compton profile for crystalline silicon[Ree72]

From Figure 3.9 the full width on the half maximum Δp_z of the Compton profile of silicon is about 2 a.u.[4] Therefore for ^{99m}Tc energy the angular uncertainty is $\Delta\theta_{FWHM} \approx 7.4keV/140.5keV = 53\ mrad = 3^\circ$. For the ^{131}I energy it is only 1.2°.

Contribution of all effects described above to the total angular uncertainty is given in Figure 3.11 as a function of scattering angle. It can be seen that the Doppler broadening is the dominating factor with the 140.5keV energy of incident photons. Since Doppler broadening together width the statistical variation in number of generated electron-hole pairs belongs to the fundamental physical limits of the camera the overall position resolution cannot be significantly improved. With the 3.3° angular resolution and 50mm distance between the camera and the patient's body it will be ≈2.9mm.

[4] In the atomic unit system e=m=$\hbar$ =1, c=137, the unit of energy is 27.21eV, the unit of momentum is 3.73keV/c or 1.99×10^{-24} kg m/s.

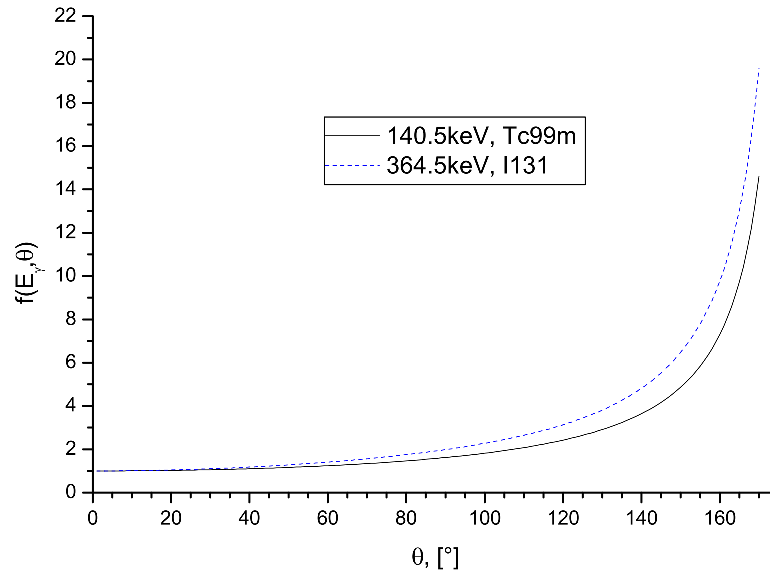

Figure 3.10: $f(E_\gamma, \theta)$ as a function of scattering angle for two different energies

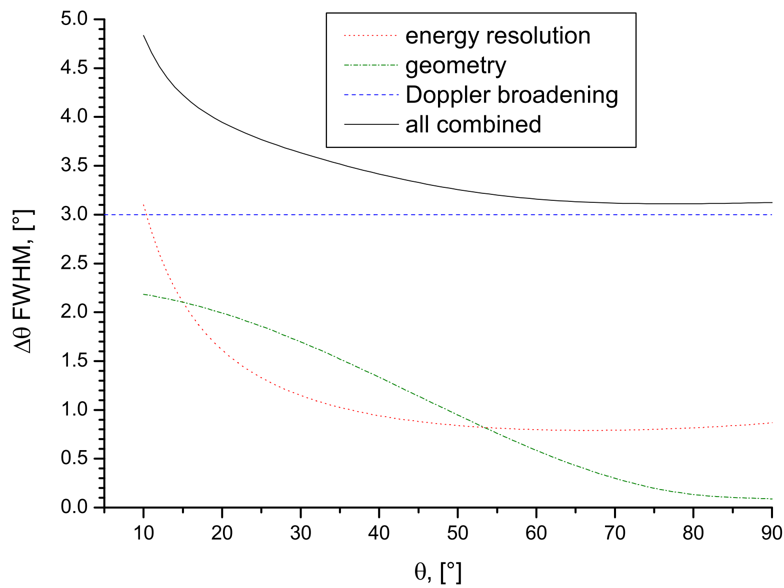

Figure 3.11: Total angular resolution: contribution of individual effects

Chapter 4

Readout electronics for scatter detector

A Si-pixeldetector was decided to be used as a scatter detector in the Compton camera prototype in order to achieve good position and energy resolution. As was discussed in Chapter 3 precise measurement of energy of the recoil electron is of great importance for the image reconstruction. Therefore much attention must be given to the low noise readout, especially to the low noise design of the first readout stage - a charge sensitive amplifier. In order to assign Compton- to photo-events off-time the absolute time of a trigger have to be measured. Also the multichannel readout giving information about the hit position and energy must be provided. Some additional readout characteristics that have to be taken into account will be discussed below.

The fine segmentation of the detector places area constraints on the readout electronics. The analog readout of one channel has to fit a detector pixel area which is very small - 200μm $\times$200μm. For this purpose an ASIC[1] was designed. The AMS[2] 0.6μm CMOS[3] process was chosen for the implementation. With three metal layers available in this process the required high integration density was achieved. The connection between the ASIC and the pixel detector will be made with a special flip chip bump-bonding technique. This technique has an advantage of adding only a small stray capacitance to the amplifier input which is important, as will be shown later, for the low noise. A relative large bump-bond pad has to be foreseen for the successful bonding.

There are two methods of coupling the detector signal to the electronics: ac- and dc-coupling. The ac-coupling requires additionally a relative large resistor and a capacitor whose implementation in the CMOS technology would occupy a large area. Because of the small pixel area the dc-coupling was realized. The drawback of this method is that the detector leakage current will flow into the electronics and can saturate the amplifier. But because of the small pixel area the expected leakage current is also small - about 20pA/pixel.

The expected low rate of events offers the implementation of the sparse-scan readout of the pixel array. In such a readout scheme only the hit pixel is read; all other pixels

[1] Application Specific Integrated Circuit

[2] Austria Micro Systems

[3] Complimentary Metal Oxide Semiconductor

are active during the readout. This implies less digital activity on the chip while the energy is measured. This fact is very important because analog and digital parts of the readout electronics are integrated on the same substrate. Also this kind of readout offers a possibility of saving power if no events occur. Power-consuming circuits such a buffers are switched on only during the readout.

The architecture of the dedicated readout chip called RAMSES is shown in the Figure 4.1. It consists of an array of 2x32 pixels with a pixel area of 200μm$\times$200μm, a readout control logic and 16 D/A converters. The D/A converters provide digitaly controlled current bias for the chip circuits, the readout control logic organises multiplexed readout of the pixel array.

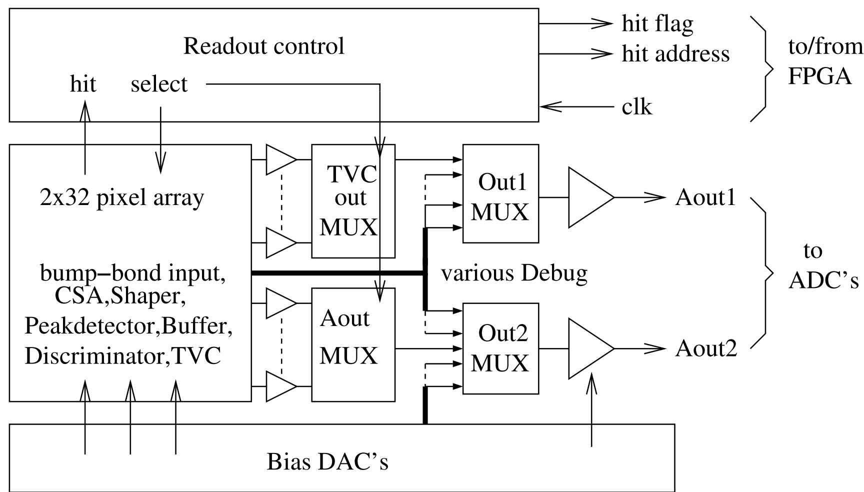

Figure 4.1: The architecture of the RAMSES chip

Every pixel contains a low noise charge sensitive amplifier(CSA), a CRRC-shaper, a discriminator, a peak detector, a time-to-voltage converter(TVC), a buffer, a 20-bit shift register(SR) and four debug buffers. The block diagram of the pixel electronics is shown in the Figure 4.2.[4] The CSA, connected with the detector by using of the bump-bonding technique, accumulates a charge pulse from the detector on its feedback capacitor C_f. To test the readout electronics without the detector a charge pulse is generated by applying a test voltage pulse to the inject capacitor C_{inj}. The shaper forms the CSA output signal for the signal-to-noise ratio optimisation. If the CSA output signal exceeds an adjustable threshold the discriminator fires, the Pixel-Control-Logic(PCL) sets a hit flag and starts the time measurement in the TVC. At the same time the peak detector samples the maximum output voltage of the shaper and holds it on the dedicated capacitor. This voltage is delivered to the analog bus through the buffer which drives a relative large capacitance of the bus. With external CLK-pulses the hit pixel is selected; the time measurement is stopped and the measured energy and the time information are available at the chip outputs as analog voltages. By programming the pixel SR one can enable

[4]The debug buffers are not shown for clarity. They are used to monitor CSA, shaper, peak detector and TVC analog outputs. Each buffer can be enabled by setting an appropriate SR-bit.

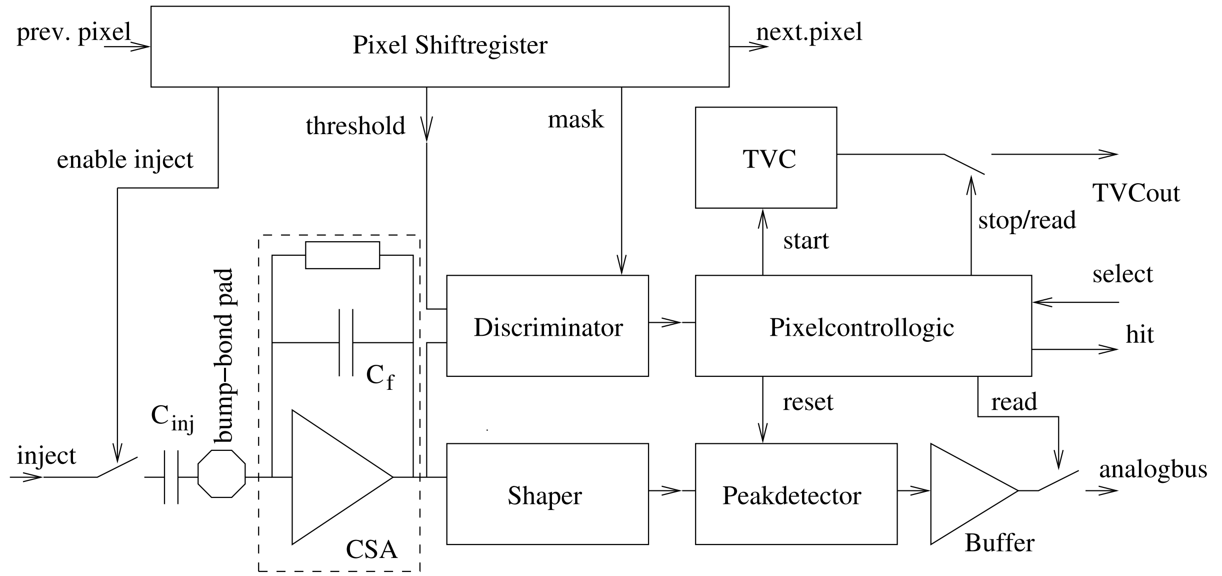

Figure 4.2: The block diagram of the pixel

injection, set 5-bit discriminator threshold, mask the discriminator and connect the four debug buffers to the output.

In the following sections each stage will be analysed in detail.

4.1 Noise considerations

This section is devoted to the optimal design of the readout electronics so that it has least effect on the charge measurement. Only the amplifier and the shaper will be considered for simplicity. Noise sources of the CSA and the detector will be analysed and methods helping to reduce their effect will be given. Also the aspect of the proper filtering by the shaper will be briefly discussed.

As a noise measure in the detector readout systems the *equivalent noise charge*(ENC) is used. This implies that the integrated noise at the output of the measuring system is expressed as an equivalent number of electrons seen at the input. Basically there are three kinds of noise sources in electrical circuits: the thermal, the shot and the flicker noise.[5] These sources are not correlated because they are all of different physical origin. Therefore the contribution of each source to the output can be considered separately. The total output noise is then the sum of the squared contributions of each component:

$$ENC_T = \sqrt{ENC_d^2 + ENC_f^2 + ENC_p^2} \tag{4.1}$$

where ENC_d, ENC_f, ENC_p are the thermal, the flicker and the shot noise components, correspondingly.

[5]These sources and the corresponding noise generation mechanisms are described in detail in Appendix A

Noise sources in the analog readout are shown in Figure 4.3, where v_{ia} and i_{ia} represent respectively the equivalent input voltage and current noise generators of the amplifier. Noise associated with the detector leakage current is i_d; the noise contribution of the reset network is represented as the i_r noise generator. C_i is the stray capacitance at the input of the amplifier and C_d is the detector capacitance. The output noise is filtered by the shaper with the transfer function $T(s)$ where $s = j\omega = j2\pi f$.

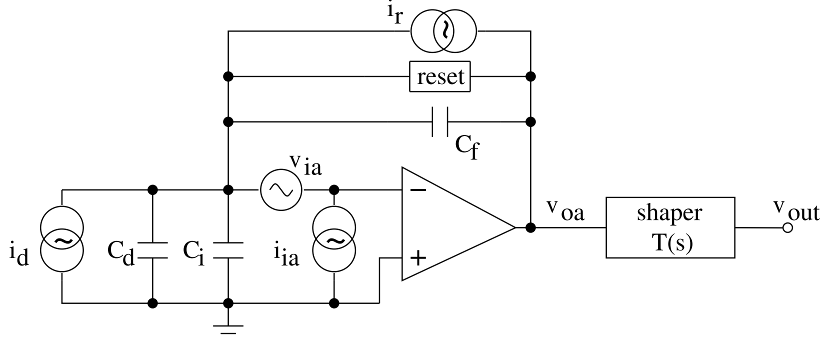

Figure 4.3: Noise sources in the analog readout

Assume that the amplifier noise is dominated by the noise of the input transistor. Then the equivalent noise generators of the amplifier can be replaced with the equivalent noise generators of the MOSFET, which have the following spectral noise power densities [San90]:

$$\overline{v_{ia}^2} = \frac{8}{3}kT\frac{df}{g_{m1}} + \frac{K_f df}{WLC_{ox}^2 f} \tag{4.2}$$

$$\overline{i_{ia}^2} = [s(C_{gs1} + C_{gd1})]^2\overline{v_{ia}^2} \tag{4.3}$$

where the first term in equation 4.2 reflects the thermal noise in the resistive channel of the transistor and the second - the flicker noise. g_{m1} is the transconductance of the input transistor, C_{gs1} and C_{gd1} are its parasitic gate-source and gate-drain capacitances. The power density of the shot noise due to the detector leakage current I_{leak} is

$$\overline{i_d^2} = 2qI_{leak}df \tag{4.4}$$

where $q = 1.6 \cdot 10^{-19}C$ is the charge of the electron. The noise contribution of the reset network will be considered in section 4.2.3. As the input voltage noise and the input current noise of the amplifier are correlated the output noise of the amplifier can be represented as [Cha97]:

$$\overline{v_{oa}^2}(s) = \left|\frac{C_t}{C_f}\right|^2\overline{v_{ia}^2} + \left|\frac{1}{sC_f}\right|^2\overline{i_d^2} \tag{4.5}$$

where $C_t = C_d + C_{in} + C_{gs1} + C_{gd1} + C_f$ is the total capacitance seen by the amplifier input. With the transfer function of the shaper $T(j2\pi f)$ the total integrated output noise voltage is

$$v_{out}^{rms} = \left[\int_0^\infty |v_{oa}(j2\pi f)|^2 |T(j2\pi f)|^2 df \right]^{1/2} \tag{4.6}$$

An optimum shaper response, which minimises v_{out}^{rms}, exists. It has a form of the cusp function[Rad88]. Since such a shaper requires very long measurement times, its implementation is impractical. Semi-Gaussian $CR(RC)^n$ shapers, consisting of one differentiation stage and n integration stages, are usually used instead. Because each capacitor occupies significant area in the CMOS technology only one integration stage was implemented in the current design. The complete description of the CRRC shaper will be given in section 4.3.

The transfer function of the CRRC-shaper with the time constant τ_0 and the amplification A is

$$T(s) = \frac{As\tau_0}{(1+s\tau_0)^2} \tag{4.7}$$

To express this voltage in ENC analog readout response to one electron charge q must be calculated. This will be done in section 4.3; under assumption of the ideal CSA the result is:

$$V_{out} = \frac{qA}{C_f e} \qquad ENC_x = \frac{v_{out,x}^{rms}}{V_{out}} \tag{4.8}$$

The thermal noise component becomes

$$ENC_d^2 = \frac{8}{3} kT \frac{1}{g_{m1}} \frac{1.57 e^2 C_t^2}{4\pi q^2 \tau_0} \tag{4.9}$$

To keep this contribution small the transconductance of the input transistor must be made large. Also total capacitance at the input must be reduced. The flicker noise component

$$ENC_f^2 = \frac{K_f}{C_{ox}^2 WL} \frac{e^2 C_t^2}{2q^2} \tag{4.10}$$

is reverse proportional to the input transistor gate area WL, C_t must be reduced as well. The shot noise

$$ENC_{p,det}^2 = 2qI_{leak} \frac{1.57 e^2 \tau_0}{4\pi q^2} \tag{4.11}$$

does not depend on CSA parameters, but on the shaper constant. It should be noted that no one component depends on the shaper amplification A. This is obvious because both signal and noise are amplified. Also the increase of transconductance helps only to some extent because it is connected with the increase of the transistor width. This in turn makes larger the total input capacitance and therefore increases the noise. So there are optimal transistor parameters for a given detector capacitance which give the lowest noise. The optimum will be found in section 4.2.1. As the shot noise component is proportional to τ_0, the thermal - reduces with τ_0, there is also an optimum for the shaping constant.

4.2 Design of the CSA

The principal diagram of the CSA is shown in Figure 4.4. It consists of an operational amplifier with the capacitive feedback C_f. The detector is represented as a diode. The charge Q generated in the detector gives rise to the current pulse $i(t)$ which is integrated by the CSA.

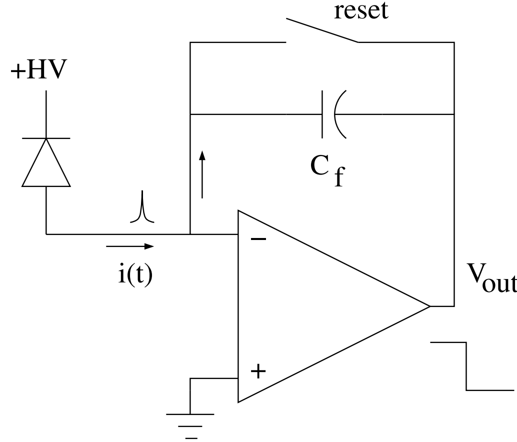

Figure 4.4: The charge amplifier

Since the input of the operational amplifier is on virtual ground its output voltage rises:

$$V_{out} = -\frac{1}{C_f}\int_0^{t_{col}} i(t)dt \tag{4.12}$$

with t_{col} being the charge collection time, which depends on the high voltage applied to the detector. As charge collection times are usually very short the current pulse can be approximated as $i(t) = Q\delta(t)$ and equation 4.12 takes a form of the step function with $V_{out} = -Q/C_f$ for $t \geq 0$ or in the frequency domain by taking the Laplace transformation: $V_{out}(s) = -Q/sC_f$.

To be ready for the next measurement a reset mechanism, shown as a switch, has to be implemented. It simply discharges the capacitor after the measurement is finished. Also the reset mechanism stabilises DC operation point of amplifier and sinks the detector leakage current.

As can be seen from equation 4.12 to have a large amplification and therefore a better resolution the feedback capacitor have to be made small. From the other hand the amplification range is limited by the output swing of the CSA. Thus the compromise has to be made between the resolution and the measurement range. As was discussed in Chapter 3 energies up to 25keV have to be measured with the analog readout. This corresponds to the up to 1.1fC of deposited charge in silicon. With CSA output swing of about 1.5V the feedback capacitance has to be at least 0.7fF. The feedback capacitance of 2fF was implemented.

Equation 4.12 is valid under assumption of the amplifier with ideal characteristics i.e with infinite gain and bandwidth. Replacing operational amplifier with an *operation transconductance amplifier*(OTA) loaded with the resistance R_L and the capacitor C_L as shown in Figure 4.5 more realistic situation is obtained. The voltage gain is now $A_v = g_m R_L$ and the bandwidth - $f_{-3dB} = 1/(2\pi R_L C_L)$.

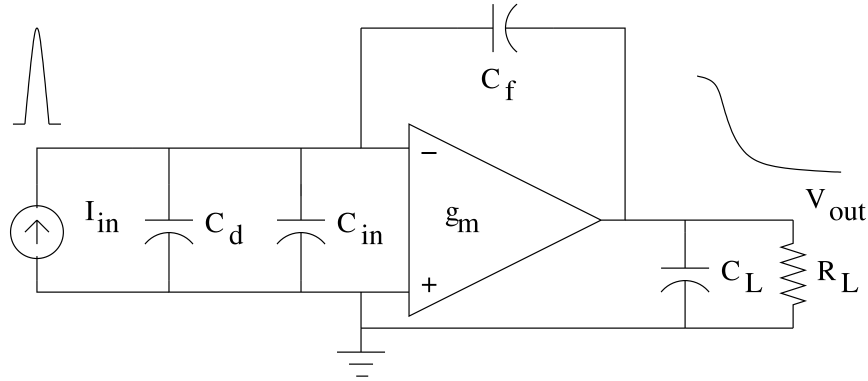

Figure 4.5: The OTA based CSA

The small-signal equivalent of the circuit in Figure 4.5 is shown in Figure 4.6. The transfer function of the CSA can be found by applying the Kirchhoff's law to the nodes of the circuit.

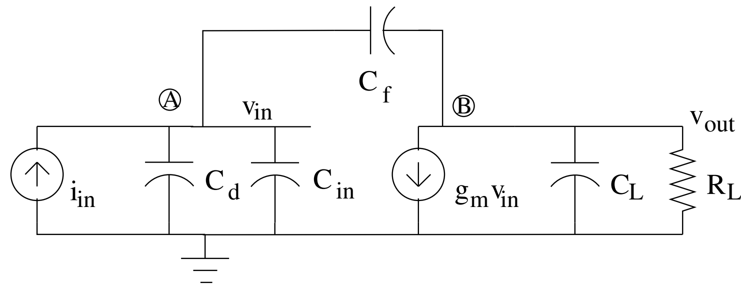

Figure 4.6: Small signal equivalent circuit of the CSA

For the node A: $$sC_f(v_{in} - v_{out}) = i_{in} - sC_d v_{in} \tag{4.13}$$

For the node B: $$sC_f(v_{in} - v_{out}) = g_m v_{in} + (\frac{1}{R_L} + sC_L)v_{out} \tag{4.14}$$

Eliminating v_{in} from these equations one obtains

$$\frac{v_{out}}{i_{in}} = -\frac{1}{sC_f}\frac{1 - s/z_0}{1 + s/p_0} \tag{4.15}$$

where $z_0 = g_m/C_f$ is the zero and $p_0 = \frac{g_m C_f}{C_t(C_L + C_f)}$ is the pole of the transfer characteristic. As the zero occurs at very high frequencies it will be neglected further. By derivation

of the above expression it was assumed that $g_m R_L \gg (C_f + C_d)/C_f$ or approximately $A_v C_f \gg C_d$. It means that the input impedance of the CSA must be much lower than the detector impedance. Under this condition the whole deposited charge is transfered to the amplifier. As the feedback capacitor is extremely small the large voltage gain is important.

Expression for the v_{out} in the time domain can be obtained by taking the inverse Laplace transform of equation 4.15.

$$v_{out}(t) = -\frac{Q}{C_f}(1 - e^{-p_0 t}) \tag{4.16}$$

Rise time of the CSA is defined as

$$t_r = \ln 9 \frac{1}{p_0} \approx 2.2 \frac{C_t(C_L + C_f)}{g_m C_f} \tag{4.17}$$

Since the C_f is very small because of the high resolution demand, the only way to decrease the rise time is to increase the transconductance of the OTA and also to keep the total input capacitance low. Having in mind expressions for the gain and the bandwidth of the OTA equation 4.17 can be rewritten as

$$t_r = 2.2 \frac{C_t}{2\pi GBW C_f} \tag{4.18}$$

where $GBW = A_v f_{-3dB}$ is so called gain-bandwidth product of the OTA. Decreasing of the rise time is now connected with the increasing GBW, so the OTA with a large GBW has to be designed. For the rise time of 200ns, C_t=600fF, C_f=2fF and C_L=50fF the OTA's gain g_m has to be 3.4mS or GBW of 525MHz.

4.2.1 Input noise matching conditions

As can be seen from equations 4.9 and 4.17 the large transconductance of the input FET is needed for both low noise and small rise time. For a MOSFET operating in the strong inversion and saturation, with width W, length L and drain-source current I the transconductance is:

$$g_m = \sqrt{2Ik'W/L} \tag{4.19}$$

Therefore minimal gate length has to be chosen for the input transistor.[6] Other options are the increase of the current or the transistor width. Because of power consumption constraints the latter is preferred. On the other hand MOSFET parasitic capacitances grow with increasing transistor dimensions. As a consequence total input capacitance increases and noise performance deteriorates. The contribution of the MOS parasitics to the total input capacitance is:

$$C_{gs1} + C_{gd1} = \frac{2}{3} C_{ox} W L + C_{ox} W L_D = \frac{2}{3} W \alpha L C_{ox} \tag{4.20}$$

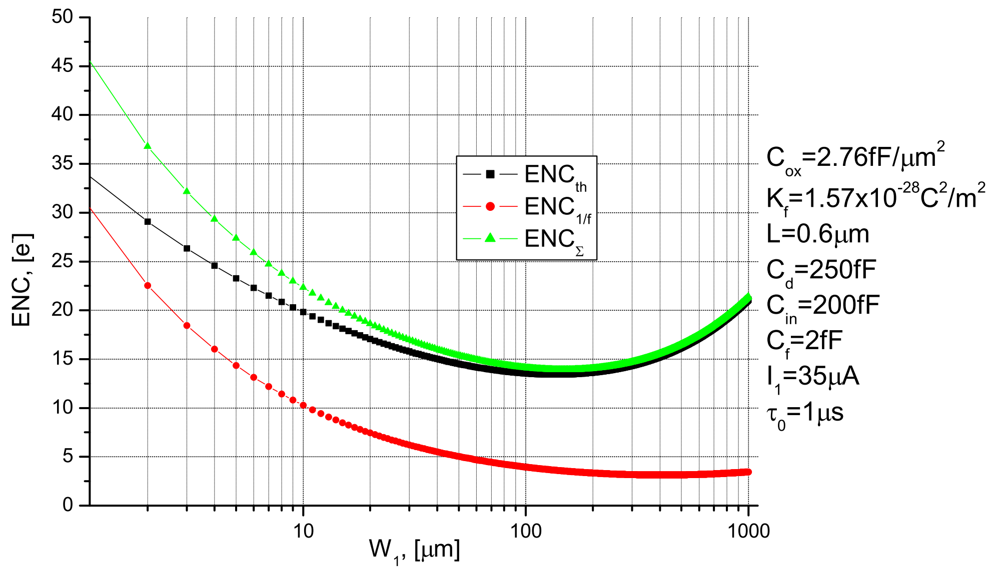

Figure 4.7: Dependence of thermal and flicker noise components and their sum on the gate width of the input transistor

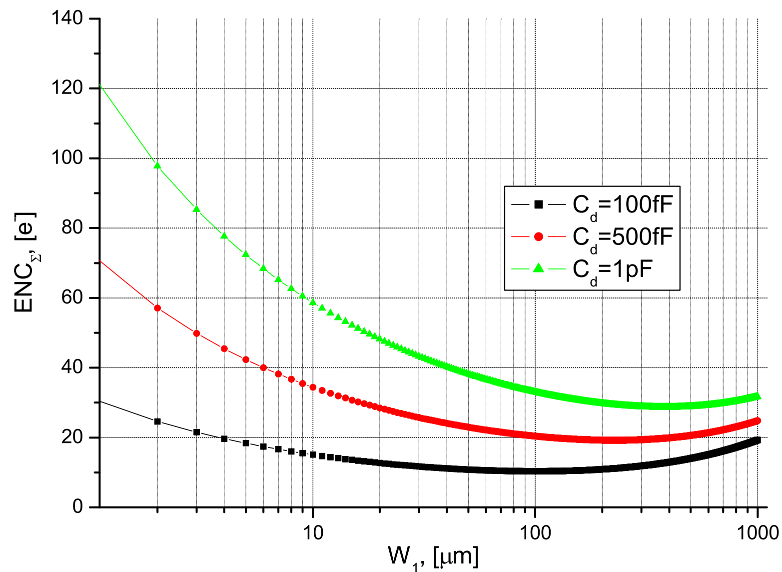

Figure 4.8: Dependence of total noise on the gate width of the input transistor at different detector capacitances

where $\alpha L = L + 3L_D$ with diffusion length L_D. Substituting 4.19 and 4.20 into 4.9 and solving the equation of its derivative with respect to the gate width results in the optimum for the thermal noise component:

$$W_{opt,th} = \frac{C_d + C_{in} + C_f}{2\alpha L C_{ox}} \tag{4.21}$$

Similar procedure can be performed for the flicker noise component given by equation 4.10, resulting in the optimal gate area. Because the gate length was already chosen this results in optimal width for flicker noise:

$$W_{opt,1/f} = \frac{3(C_d + C_{in} + C_f)}{2\alpha L C_{ox}} \tag{4.22}$$

which is three times larger then $W_{opt,th}$. The optimal width for total noise was found graphically from Figure 4.7 and is about $150\mu m$.

The variation of the optimal gate width with the detector capacitance is shown in Figure 4.8. For the input transistor with the $100\mu m$ width an increase in 0.5pF of the input capacitance (e.g. due to test wire-bonding) results in more than 50% larger noise.

4.2.2 Large GBW amplifier

A cascode amplifier is often used in the detector readout electronics because it allows to achieve a large amplification in one stage. GBW products of several GHz can be realised[Cha97]. But on the cost of large power consumption and occupation area, which are critical in the multichannel readout. By using of the regulated cascode stage[Sae90] in the amplifier instead of the simple cascode the power and the area can be reduced.

The functional diagram of the cascode and the regulated cascode(RGC) amplifiers[7] are shown in Figure 4.9. The input transistor T_1 biased with the current I_{inp} acts as a transconductance element: it converts small signal input voltage into current, which is flow into the transistor T_2 biased with the constant gate voltage V_{casc}. Small signal input impedance of this transistor is low so the drain-source voltage of the input transistor remains almost unchanged whereas the output voltage experiences large swing. This has two positive effects: firstly the output resistance increases; secondly the amplifier becomes more resistant to the Miller effect[San87].

An additional common source stage formed by the transistor T_3 and the current source I_{reg} in Figure 4.9b improves the cascoding effect. The drain-source voltage of the input transistor is regulated now to the fixed value by using of the negative feedback. The input impedance looking into the source of T_2 drops and the output impedances rises. These impedances of both amplifiers are given in Table 4.1 for the comparison. As can be seen from the table by choosing r_{load} a compromise between low input and high output impedance has to be made. As the voltage gain of both amplifiers $A_{v0} \approx g_{m1} r_{out}$ is proportional to the output impedance it is also larger for the regulated cascode amplifier.

[6] At the minimal gate length the equation 4.19 is not quite correct because of the effect of carriers velocity saturation in the channel. As the result the transconductance becomes smaller.

[7] To be more precise the adjective *folded* has to be added to the amplifier names as the ac signal current is folded back to the power supply

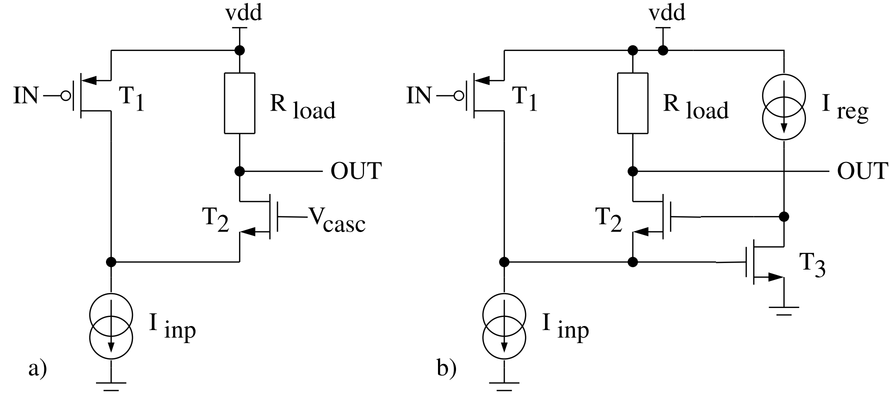

Figure 4.9: The functional diagram of the cascode a) and the regulated cascode b) amplifiers

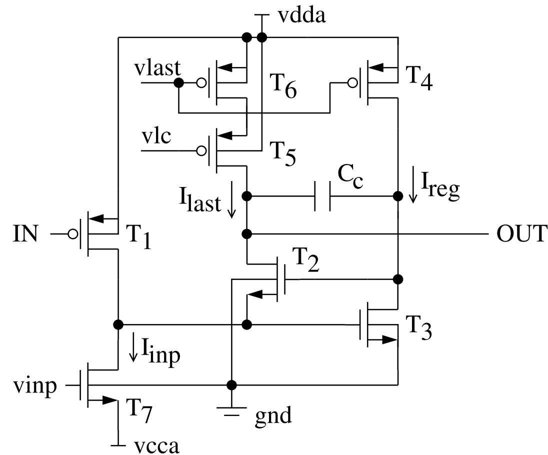

Figure 4.10: Schematic of the regulated cascode amplifier

The implemented regulated cascode amplifier is shown in Figure 4.10. The transistors T_4 and T_7 were used as the current source I_{reg} and the current sink I_{inp}, respectively. The transistors were made longer in order to reduce Early effect[Sed98], i.e. to increase their output impedance. To achieve both the high output swing and the large output impedance a high swing cascode current source[All02] formed by the transistors T_5 and T_6 was implemented as the load. The output impedance of this source is equal to $r_{ds6}\frac{g_{m5}}{g_{ds5}}$ which ensures the compromise discussed above. The variable bias voltages for the current source transistors are generated on-chip by the current steering DACs described in section 4.8. To save one current reference the ratio between I_{last} and I_{reg} was fixed to 3:1. The compensation capacitor C_c is used to prevent high-frequency oscillations. The high-frequency analysis of the amplifier with the explanation of the compensation technique is given in [Nic03]. The effect of C_c can be seen in Figure 4.11 where AC analysis of the RGC amplifier, performed by using the Cadence SpectreS simulator, is shown. With

Parameter\Configuration	Cascode amplifier	Regulated cascode amplifier
input impedance	$\frac{r_{load}+r_{ds2}}{\frac{g_{m2}}{g_{ds2}}}$	$\frac{r_{load}+r_{ds2}}{\frac{g_{m2}}{g_{ds2}}\cdot\frac{g_{m3}}{g_{ds3}}}$
output impedance	$r_{load}\|\|\frac{g_{m2}r_{ds1}}{g_{ds2}}$	$r_{load}\|\|\frac{g_{m2}g_{m3}r_{ds1}}{g_{ds2}g_{ds3}}$

Table 4.1: Small signal parameters of the cascode and regulated cascode amplifiers

the compensation capacitor the phase margin $\Phi_m = 45°$.[8] The negative effect of C_c is a reduction of the amplifier bandwidth which results in the larger rise time.

It is important to design the amplifier so that its noise will be dominated by the input transistor and thus the noise considerations made before will be correct. For this purpose the low-frequency noise analysis of circuit in Figure 4.10 was performed. The noise contribution of each transistor was modelled as a noise current source connected between its drain and source terminals. Then the contribution of each noise source to the output noise was calculated and the total output noise was found by the superposition principle. The output noise was recalculated into the equivalent input voltage noise by using $v_{in} \approx i_{out}/g_{m1}$ which is resulted in the following equation:

$$\overline{v_{in}^2} \approx \frac{\overline{i_{n1}^2}}{g_{m1}^2} + \frac{\overline{i_{n7}^2}}{g_{m1}^2} + \frac{\overline{i_{n2}^2}}{g_{m2}^2\left(\frac{g_{m1}}{g_{ds1}}\right)^2\left(\frac{g_{m3}}{g_{ds3}}\right)^2} + \frac{\overline{i_{n3}^2}+\overline{i_{n4}^2}}{g_{m3}^2\left(\frac{g_{m1}}{g_{ds1}}\right)^2} + \frac{\overline{i_{n5}^2}}{g_{m5}^2\left(\frac{g_{m1}}{g_{ds6}}\right)^2} + \frac{\overline{i_{n6}^2}}{g_{m1}^2} \tag{4.23}$$

where $\overline{i_{ni}^2}$ is the current noise contribution of the i-th transistor. Firstly consider noise from the "basic" transistors $T_1 - T_3$. As $g_{mi}/g_{dsi} \approx 100$ noise of T_2 and T_3 are significantly lower than input transistor noise. The current sources $T_4 - T_7$ mirror the currents generated from the on-chip reference. It can be shown[Lak94], that if the ratio between output(mirrored) and input(reference) current in a current mirror is B_i, the relationship between their noise currents is

$$\overline{i_{ni}^2} \approx B_i^2\overline{i_{ref}^2} + \frac{8kT}{3}(B_i+1)g_{mi}df \tag{4.24}$$

The first term comes from the reference, the second - from the transistor itself. Keeping in mind equation 4.23, the inherent contributions of transistors $T_4 - T_7$ can be kept low by increasing their transconductance and gate area. A low-noise reference has to be designed. Also to reduce the influence of the reference noise B_i has to be lower than one. Since the current through T_7 is the largest it will suffer more from noise of the reference.

Noise behaviour of the noise-free biased amplifier was analysed with the SpecteS simulator. The equivalent input voltage noise of the amplifier together with the contribution

[8] The compensation was made for the worst case feedback, i.e. for the feedback factor equal to one. In the implemented CSA the feedback factor is determined as a ratio of the feedback to the input capacitance and much lower than one. Thus the true phase margin will be noticeably larger.

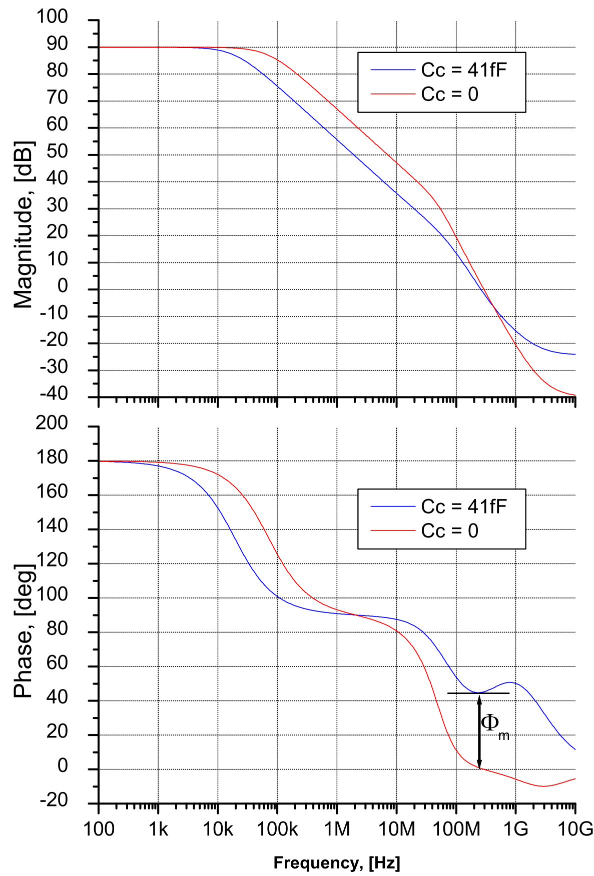

Figure 4.11: Open loop transfer characteristics of the RGC amplifier

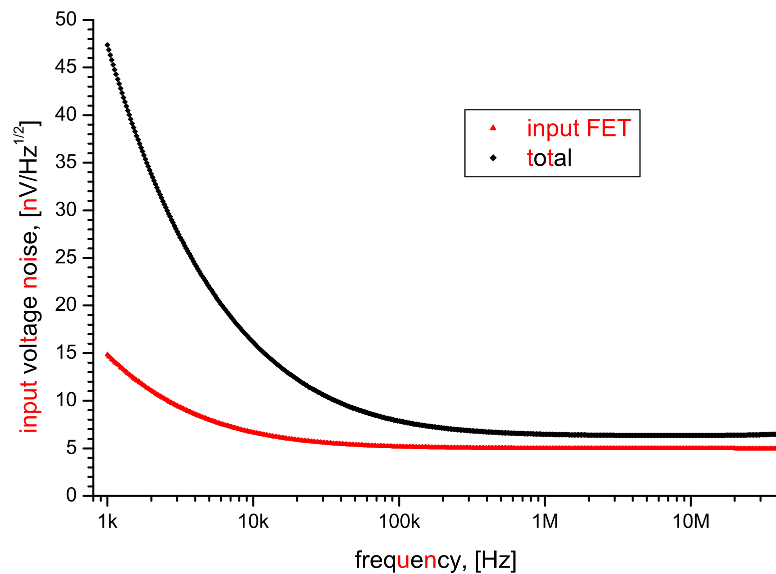

Figure 4.12: Noise contribution of the input FET to the total input noise

of the input transistor is shown in Figure 4.12. As can be seen the voltage noise of the input transistor is dominating in the frequency range of interest(100kHz-1MHz). At lower frequencies the flicker noise of the NMOS transistors dominates.

4.2.3 Feedback

The feedback mechanism is responsible for the discharge of the feedback capacitor, setting the amplifier into the operation point and sinking detector leakage current. The reset mechanism can be discrete or continuous. In the first case the feedback capacitor is discharged by a pulse after energy measurement is finished, in the second - feedback capacitor discharges permanently. The pulsed discharge is usually used in the experiments where high rate of events is expected; continuous reset is more suited for low-noise applications and therefore will be discussed further. As the expected detector leakage current and consequently its noise contribution are small, it would be clever to keep noise contribution of the feedback small too. The simplest solution would be a large resistor, but it cannot be implemented in the CMOS process. Two other methods implementing transistors are shown in Figure 4.13.

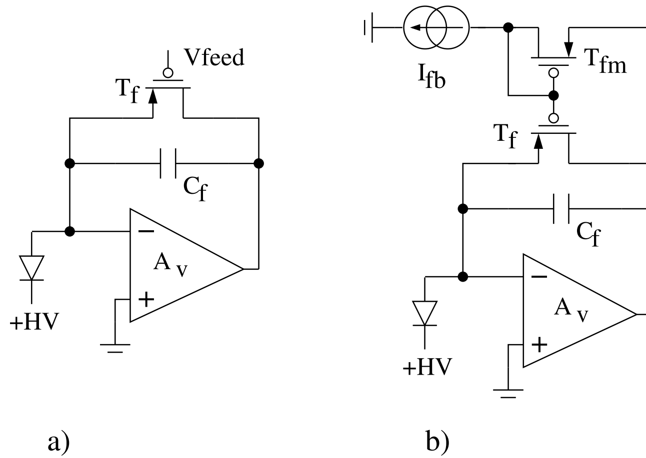

Figure 4.13: MOSFET as a feedback element: a) voltage-biased b) current-biased

In both cases the transistor T_f operating in the subthreshold region is used as a feedback element. In the case a) the MOSFET is biased with the external gate voltage V_G. Without input signal the feedback transistor is in linear region; its drain-source voltage is nearly zero allowing the detector leakage flow through. When the signal comes the drain-source voltage rises and the transistor enters saturation. Much larger current can flow through the transistor - the current that discharges the feedback capacitor. By changing the gate voltage the discharge current can be adjusted. As the equivalent feedback resistance in subthreshold is several $G\Omega$, the feedback transistor contributes little noise. Knowing transconductance of the FET in the subthreshold $g_m = qI_{leak}/nkT$[Vit77] the noise contribution is given as:

$$\overline{i_r^2} = \frac{8}{3}kTg_{m,fb}df = \frac{8qI_{leak}}{3n}df \tag{4.25}$$

where n is the subthreshold slope factor. It is interesting to note that this noise is independent of transistor geometry. With $n \approx 1.5$ for PMOS transistors $\overline{i_r^2} \approx \overline{i_d^2}$ and the total shot noise contribution becomes approximately twice of given by equation 4.11:

$$ENC_p^2 = 4qI_{leak}\frac{1.57e^2\tau_0}{4\pi q^2} \tag{4.26}$$

The main drawback of this feedback configuration is that proper gate voltage depends both on the threshold of the feedback transistor and the DC input voltage of the amplifier. These parameters can vary in CMOS process by about 10%. To be less sensitive to these variations the W/L ratio of the feedback transistor is made small. Another solution of this problem is presented in Figure 4.13b. This is PMOS implementation of the method firstly proposed by Blanquart[Bla97]. Here the gate-source voltage of the feedback transistor is set, therefore it tracks DC voltage variation of the amplifier input. The feedback capacitor will be discharged with the current I_{fb}. As the transistors T_f and T_{fm} are layouted close to each other the threshold difference between them is small. Therefore variation of the discharge current between the pixels is expected to be low. The noise is the same as in the first case.

4.2.4 Inject capacitor

To have the possibility of testing of readout electronics without bonding it to a detector, a capacitor connected to the CSA input is used. A test pulse, applied to this capacitor, injects charge into the amplifier.

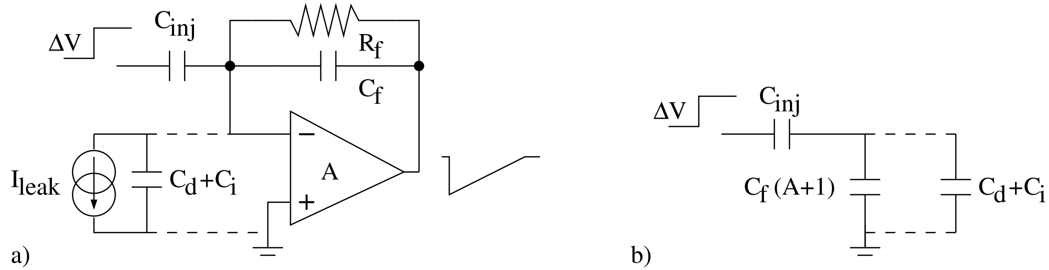

Figure 4.14: a) CSA test circuit b) Its equivalent according to the Miller theorem

The CSA test circuit and its equivalent according to the Miller theorem are shown in Figures 4.14a and 4.14b respectively. The case where the CSA is bonded to a detector is shown with the dashed line. Charge injected into the unconnected CSA can be easily found from Figure 4.14b:

$$Q_{in} = C_{inj}\Delta V_{inj}\frac{1}{1+\frac{C_{inj}}{C_f(1+A)}} \tag{4.27}$$

To have voltage step developed fully over the inject capacitor the latter has to be smaller than the dynamic input capacitance, i.e. $C_{inj} \ll C_f(1+A)$ with A being the open-loop gain of the amplifier. This is true in our case with $A = 10^4$, $C_f = 2fF$,

$C_{inj} = 20fF$. In the presence of the detector and the stray capacitance associated with the wire-bonds only a fraction of charge is injected into CSA. With $Q_{in} = C_{inj}\Delta V_{inj}$ the charge seen by the CSA is:

$$Q_{CSA} = \frac{Q_{in}}{1 + \frac{C_d + C_i}{C_f(1+A)}} \tag{4.28}$$

With 1pF of additional capacitance(detector+stray) only 95% of the input charge is detected with the CSA. The same situation will be also in the case of testing the electronics with a gamma source.

If a detector is connected to the CSA input the test circuit still can be used. The detector capacitance will lead to the rise time increase and the leakage current will cause the shift of the operation point of the amplifier, which can in turn slightly change its gain. A SPICE simulation of the two considered cases is presented in Figure 4.15. It shows about 9% increase in the gain and about 100% increase in the rise time in the case when the CSA is bonded to the detector.

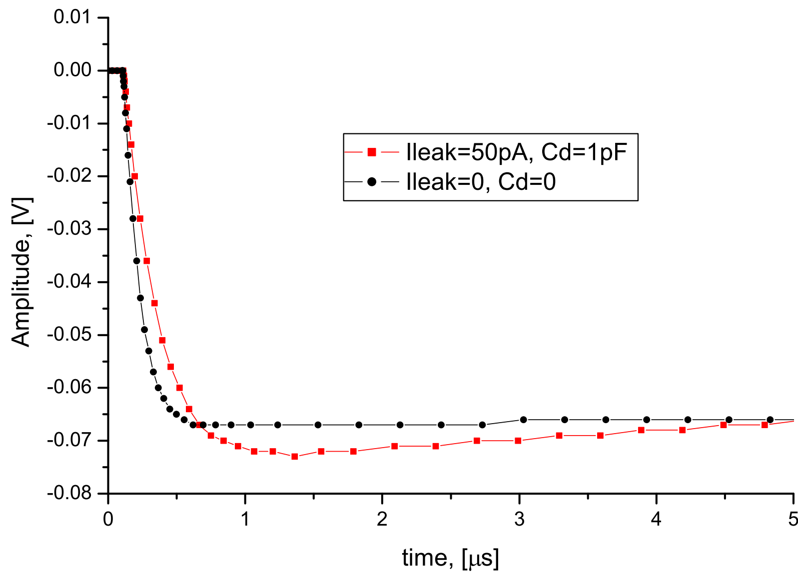

Figure 4.15: CSA response to the inject pulse

4.2.5 Implementation

The complete CSA schematic and layout are shown in Figures 4.16 and 4.17. To buffer the RGC amplifier output prior to connection with the shaper a source follower[Sed98] was used. It is formed by two PMOS transistors: "main" T_8 and the current source T_9. The PMOS variant was chosen because source and bulk terminals of T_8 can be connected in the process; this eliminates the bulk effect[Sed98] and thus, comparing with the NMOS follower, a better linearity can be achieved.

With $W = 107.2\mu m$ and $L = 0.6\mu m$ the input transistor is the largest. The special finger structure was used for the layout: eight narrower transistors were connected in

parallel with drain and source terminals shared by the adjacent transistors. This structure has two benefits: firstly the occupied area is smaller, secondly the parasitic drain-bulk and source-bulk capacitances are lower. On the right hand side of Figure 4.17 a part of the bump-bond pad of $\phi = 45\mu m$ is seen. The pad and also partially the input transistor are surrounded by a p^+ guard ring to protect them form lateral currents in the substrate. The extreme small feedback capacitor C_f of 2fF was made by the overlap of the two tiny metal pieces of adjacent metal layers. Two inject capacitors of 1.8fF and 17.4fF were implemented in the same way under the bump-bond pad. It should be noted that values of these capacitors were extracted from the layout and generally cannot be used for precise calculations as for example the noise calculation.

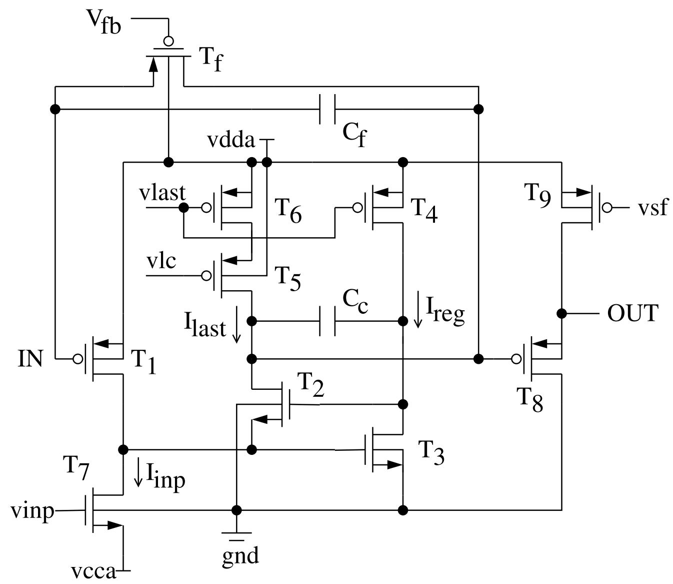

Figure 4.16: The implemented CSA

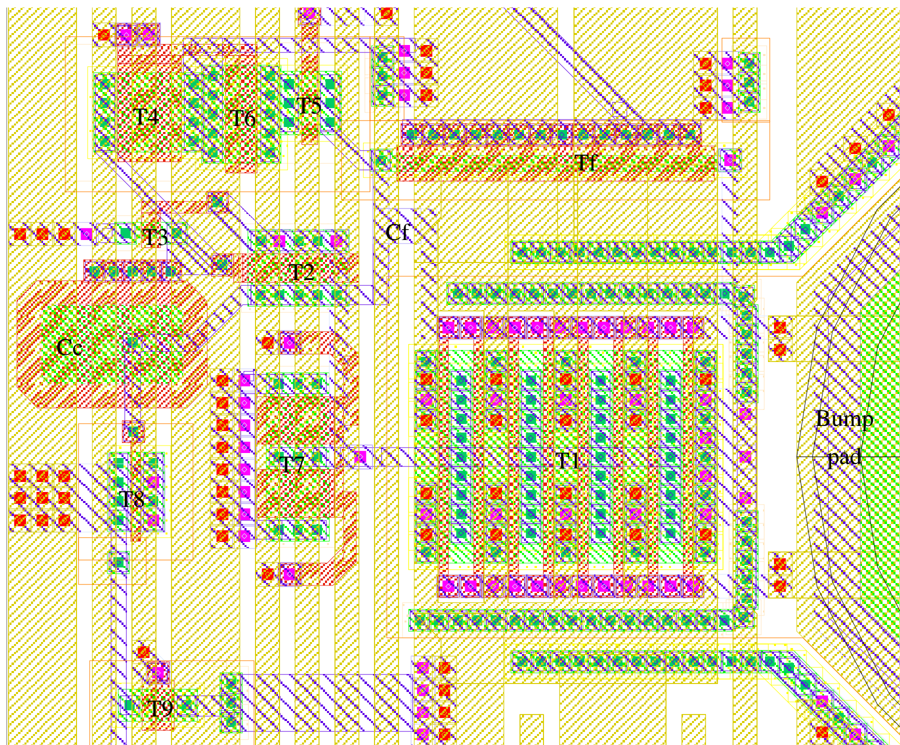

Figure 4.17: Layout of the CSA($50\mu m \times 45\mu m$)

4.3 The CRRC shaper

The next stage in the analog signal processing is the CRRC shaper. It optimises signal-to-noise ratio of the CSA output signal by limiting the frequency bandwidth.

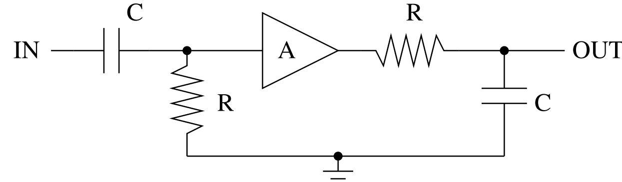

Figure 4.18: The functional diagram of the CRRC shaper

The functional diagram of CRRC-shaper is shown in Figure 4.18. It consists of two filters isolated by a buffer with the gain A. The first filter is a high-pass filter formed by a capacitor C and a resistance R. The second filter is a low-pass filter formed by the same elements. Using the high-pass filter as a first stage keeps the shaper independent of the DC output variations of the CSA. The transfer function of the CRRC shaper is

$$T(s) = \frac{As\tau_0}{(1 + s\tau_0)^2} \tag{4.29}$$

with $\tau_0 = RC$ called the shaping time. In the readout shaping times about one microsecond have to be realised. It means that for the capacitor of 1pF the resistor has to be $1M\Omega$ which cannot be realised as a passive component in the CMOS technology. The possible implementation of a large resistance by using of active components is given in [Ste91]. The circuit shown in Figure 4.18 has also the disadvantage of having the shaping time fixed. The shaper proposed and realised by Hausmann[Hau02] was used in the current design. It is shown in Figure 4.19.

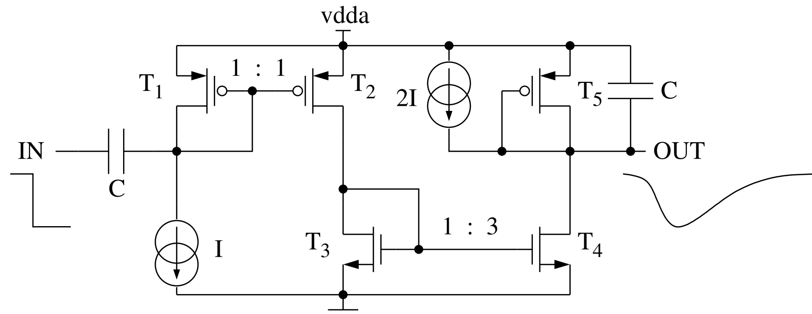

Figure 4.19: The CRRC shaper schematic

The transistor T_1 biased with the current source I acts as a resistance, forming high-pass with the input capacitor C_1. Change in voltage on this resistance is transformed into ac current by T_2. This current is multiplied by a factor three in the current mirror formed by T_3 and T_4. As the DC current is also multiplied by the same factor twice of

the current must be subtracted for correct biasing of T_5. The transistor T_5 acts also as a resistance and forms together with C_2 the low-pass filter. More detailed analysis can be gained from considering the small-signal model of the shaper is shown in Figure 4.20 with C_L being load capacitance of the shaper.

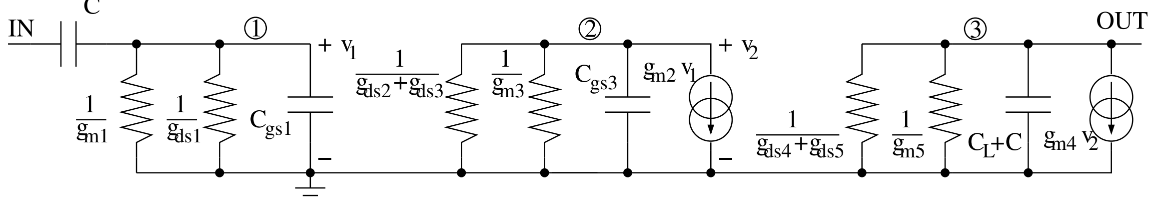

Figure 4.20: Small-signal model of the shaper

$$\text{For the node 1:} \qquad v_1 = \frac{sCv_{in}}{g_{m1} + g_{ds1} + sC_{gs1} + sC} \tag{4.30}$$

$$\text{For the node 2:} \qquad v_2 = -\frac{g_{m2}v_1}{g_{m3} + g_{ds2} + g_{ds3} + sC_{gs3}} \tag{4.31}$$

$$\text{For the node 3:} \qquad v_{out} = -\frac{g_{m4}v_2}{g_{m5} + g_{ds4} + g_{ds4} + s(C + C_L)} \tag{4.32}$$

Eliminating subsequently v_1 and v_2 from the equations and taking into account that $g_{mx} \gg g_{dsx}$ and C is considerably larger than any parasitic capacitance one can obtain

$$v_{out} = \frac{g_{m2}}{g_{m5}} \frac{g_{m4}}{g_{m3}} \frac{\frac{sC}{g_{m1}}}{1 + \frac{sC}{g_{m1}}} \frac{1}{1 + \frac{sC}{g_{m5}}} v_{in} \tag{4.33}$$

With $g_{m1} = g_{m2} = g_{m5}$, $g_{m4} = 3g_{m3}$ and $\tau_0 = C/g_{m1}$ the shaper transfer function takes the form of equation 4.29 with the gain $A = 3$. As $g_{m1} = \sqrt{2Ik_pW/L}$

$$\tau_0 = \frac{C}{\sqrt{2Ik_p\frac{W}{L}}} \tag{4.34}$$

Thus the shaping time can be changed by adjusting the bias current I. But also ac current affects the shaping time. To employ the small-signal approximation model also for larger input signals the transistors T_1 and T_5 are made narrow and long. But, of course, the linearity of this shaper will be worser than that of the shaper build with the passive components. For the ideal CSA response of Q/sC_f the response of the shaper is:

$$V_{out}(s) = \frac{As\tau_0}{(1 + s\tau_0)^2} \frac{Q}{sC_f} \tag{4.35}$$

Or in the time domain by taking the inverse Laplace transformation:

$$V_{out}(t) = A\frac{Q}{C_f}\frac{t}{\tau_0}e^{-\frac{t}{\tau_0}} \tag{4.36}$$

The output voltage has a maximum at $t = \tau_0$ and the overall readout gain remains about Q/C_f as the gain $A = 3$ compensates internal $1/e$ gain loss of CRRC shaper. Now since the parameters of the CSA and the shaper are known optimal shaping time and total noise can be calculated. The optimal shaping time was found by solving the equation for the derivative of ENC_T:

$$\tau_{opt} = C_t \sqrt{\frac{2kT}{3qI_{leak}g_{m1}}} \tag{4.37}$$

For the $I_{leak} = 10pA$, $g_m = 0.7mS$, and $C_t = 1pF$ the optimal shaping time is equal to $1.6\mu s$. And the total minimal noise is $32e^-$.

The contributions of the different noise mechanisms were calculated as a function of shaping time by using equations 4.1,4.9,4.10,4.26 and are shown in Figure 4.21.

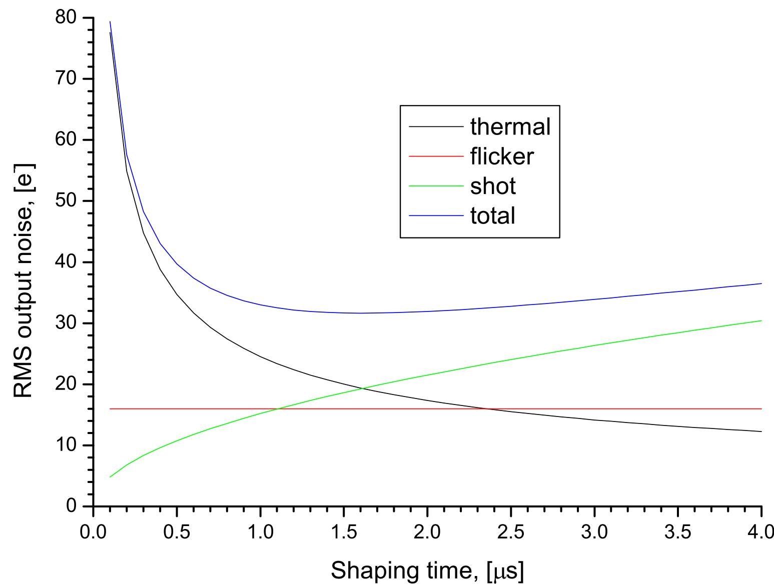

Figure 4.21: Noise contribution as a function of shaping time

It should be noted that the noise calculated above was obtained under assumption of ideal voltage and current sources. In reality noise contribution of these sources can considerably degrade noise performance. The most sensitive stage is the CSA, especially the input transistor. As the source terminal of the input transistor is connected to the power supply, variations in the power supply will be seen as an input signal. Therefore the power supply noise can be added directly to the input voltage noise of the amplifier. Let power supply noise be neglected if it contributes only 1% to the total integrated output noise. It corresponds to 14% of the total spectral noise density. As the bandwidth will be limited by the CRRC shaper with the time constants about $1\mu s$, we are interesting in noise densities in the 100kHz-2MHz range. By analysing the input voltage noise in Figure 4.12 the power supply noise density can be specified to $1nV/\sqrt{Hz}$, which is very small. Same conditions applied to the output current noise without the input transistor contribution give $1pA/\sqrt{Hz}$ for $g_m = 1mS$.

4.4 Peak detector

The task of a peak detector is to detect and to hold the maximum of a shaper signal, which gives information about deposited energy in the detector. The block diagram of the peak detector together with its characteristic response are shown in Figure 4.22.

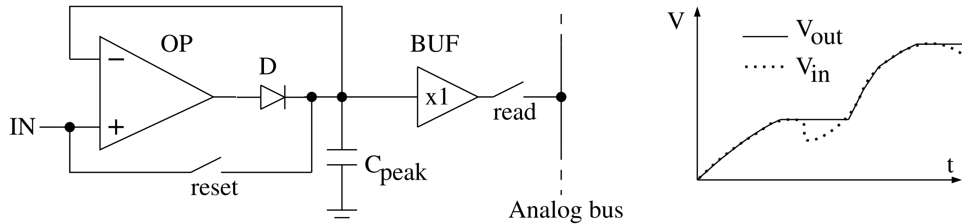

Figure 4.22: Functional diagram of the peak detector

In the beginning the reset switch is closed and the capacitor C_{peak} is discharged. With opening of the switch the peak detector samples the input voltage. If the input voltage is larger than the voltage across C_{peak}, the capacitor is charged until the difference vanishes. The diode protects the capacitor from discharge if the input voltage drops below the output. The operational amplifier provides a high input impedance and large slew rate to quickly charge the capacitor. The negative feedback helps to compensate for the diode leakage current and for the diode drop voltage, which otherwise would make impossible the detection of small signals. The unity gain buffer is required to drive the analog output bus.

This principle was implemented in the CMOS technology by Hausmann[Hau02] for shaper signals of the negative polarity. In the application the readout logic opens the reset switch when the discriminator signalises a hit; the peak value is read when the pixel is selected by the readout logic. After the value is acquired the peak detector is reset by de-selection of the pixel. Since the peak detector input is DC-connected with the shaper the pre-charged value of C_{peak} capacitor, called a pedestal, depends on the shaper bias. To measure the signal amplitude the pedestal has to be measured prior to the data acquisition and then subtracted from the data.

4.5 Discriminator

Since the readout electronic is supposed to be self-triggered, a discriminator circuit must be implemented. This circuit produces a logic pulse if the input signal is above a certain value, which is called threshold. Threshold helps to separate useful events from background and can be normally adjusted.

In the current implementation[Hau02] the discriminator circuit is watching CSA output. If CSA signal crosses the threshold the discriminator fires. It sets a hit flag, which signalises to the readout logic that a readout cycle must be organised(see section 4.7). Discriminator signal also enables the peak detector and triggers the time measurement. It can be observed at the *hitbus* output of the chip which is a wire-ored combination of all unmasked discriminator outputs.

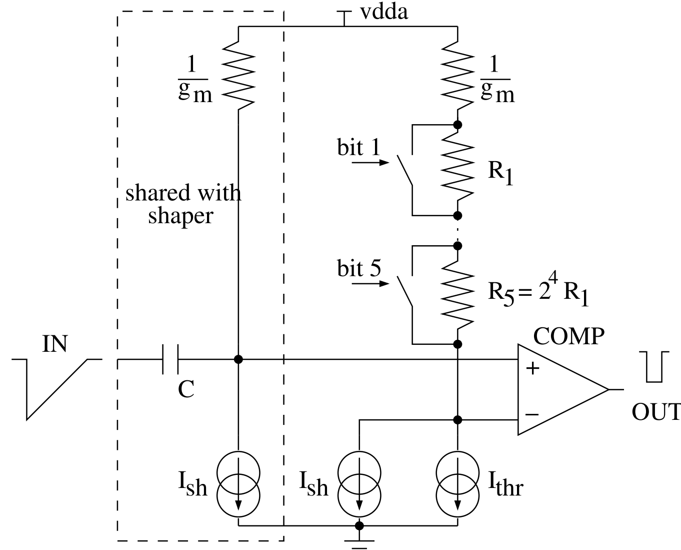

Figure 4.23: Block diagram of the discriminator

A block diagram of the discriminator is shown in Figure 4.23. It consists mainly of a comparator(COMP) and a circuit which provides a constant voltage drop between its inputs. Once the signal overcomes this drop an output pulse is produced. The discriminator is AC-coupled to the CSA to get rid of differences in CSA DC output voltage between the pixels. This differences occur because of the process parameters and detector leakage current variations. For the AC-coupling the differentiation stage of the shaper was used in order to reduce the layout area. This has a drawback of having threshold dependence on the shaper bias current and therefore on the shaping time.

The threshold is set by a current I_{thr}, common to all pixels and generated by the on-chip DAC7. If all switches in Figure 4.23 are closed the input voltage must exceed $\Delta V = I_{thr}/g_m$ to trigger the discriminator. Having low threshold would allow the measurement of small scattering angle events which can increase the statistics. The minimal threshold is determined by the noise. Expected $30e^-$ noise give rise to about $2.5mV$ standard deviation of CSA output voltage. To have the noise hits rate low the threshold has to be at least 3σ, which is $7.5mV$ or about $90e^-$.

The comparator is implemented as a differential amplifier[Hau02] and therefore has a differential pair as an input. The variation of threshold voltage of MOSFET's in the pair along with bias current variation can cause the threshold shift of up to 20mV. To compensate for this value or to adjust the thresholds of different channels five binary-weighted resistors were implemented. They are connected serially and can be shorted by switches. These switches are controlled by the five bits, provided from the pixel shift register - in total 32 adjustment steps are possible. Every resistor was implemented as a PMOS operating in linear region, with a resistance:

$$R = \frac{1}{k_p' \frac{W}{L}(V_{gs} - V_{th})} \tag{4.38}$$

Binary-weighting of resistances was achieved by doubling the length of transistors as shown in Figure 4.24. In practice the doubling is not exact due to the process induced variations of the effective transistor length and threshold. Also the voltage drop on the upper(closer to VDDA) resistors or on the "on" -resistance of NMOS switches reduces the source voltage of lower(closer to comparator) transistors. This leads to lower V_{gs} voltage and larger V_t voltage due to the bulk effect[9][Sed98], which both increase the resistance according to equation 4.38.

Figure 4.24: Implementation of the resistor chain

As an example a simulated dependence of the threshold ΔV on the threshold code is shown in Figure 4.25 for DAC7=3, DAC6=100 and VDDA=3.6V. The threshold is $\approx 700e^-$ and can be adjusted in the interval of $700 - 2100e^-$. As can be seen, the threshold step per bit is not equal - especially by transition from 15 to 16 the large gap of $100e^-$ exists.

Figure 4.25: Sample of the discriminator threshold set

[9]Bulk effect can be avoided by placing every PMOS in its own N-well, biased with its source voltage. But due to the process specified minimal distance of $5.6\mu m$ between different biased N-wells the occupied area will be considerably larger.

4.6 Time measurement

As an alternative to the hardware coincidence between Compton- and photodetectors a software coincidence approach can be used. This approach requires the recording of a hit moment in both detectors for a later matching. Because of the readout complexity it is not straightforward. In the present solution the time information consists of three components: an elapsed time between the hit and the moment of its readout, measured directly in pixel, a timestamp of the readout moment, recorded locally in the FPGA, and a time moment when the FIFO is read recorded by a PC.

Because readout moment of a hit is determined by the readout logic, as, for example, in the case of many simultaneous hits, it is necessary to measure time between hit and readout directly in a pixel. For this purpose an analog method of a time measurement is the best choice[Ibr00]. By this method during the measured period of time a capacitor is charged with a constant current; the elapsed time is then proportional to the change of the voltage across the capacitor.

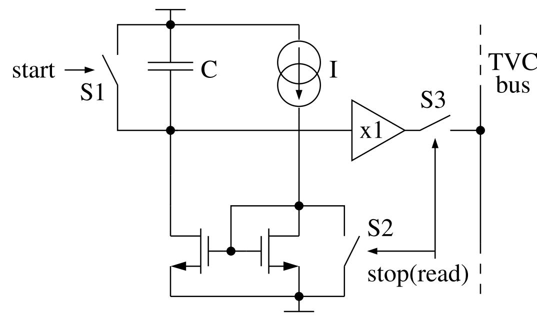

Figure 4.26: Principle of the time measurement in a pixel

The principle diagram of time measuring circuit, called also a Time-to-Voltage Converter(TVC), is shown in Figure 4.26. Initially the switch S1 is closed and the switches S2,S3 are open and the capacitor C is discharged. A *start* signal opens S1 and the capacitor charges with a current I. A *stop* signal closes S2, turning off the current. At the same time S3 is closed and voltage across the capacitor can be read from the bus. An additional unity gain buffer is used to drive a bus capacitance. After the voltage is read S1 is closed, discharging the capacitor, and S2 is opened allowing the next measurement.

In the implemented circuit the discharge current was supplied from DAC1 to have a possibility of the adjustment of a measurement range. The unity gain buffer was implemented as a source follower[Sed98], biased with a current from DAC0. Due to the inherent offset of the source follower, a time measurement range is shortened. Also the non-linearity of the source follower due to the bulk effect have to be considered by performing a TVC calibration. The TVC layout occupy a moderate area; during the time measurement the digital activity in the chip is low, which is very important for extremely sensitive charge measurement, running in parallel.

A timestamp value in the FPGA, recorded in the FIFO together with digitised time and energy information, is the state of 24bit counter in the moment of a hit readout. The counter is permanently clocked with 5MHz; thus it has 3.4s period and 200ns time

resolution. A PC timer resolution depends on a PC clock speed; for a modern computers 1ms resolution is easily achievable. It is noted that for the second(photo) detector same time measurement scheme with synchronised clocks must be used. Only in this case a correct assignment of Compton- and photo-events is possible.

4.7 Readout logic

Since the expected rate of events is rather low, there is no need to read out the full pixel matrix after detection of a single hit. With large number of pixels this procedure can take a considerable time; during this time new events cannot be acquired. Also the high digital activity is an issue. Therefore a *sparse scan* scheme was implemented, which is based on the following principles:

☞ it reads only pixels with hits

☞ it does not interrupt acquisition of new events

The block-diagram covering the whole readout structure is shown in Figure 4.27.

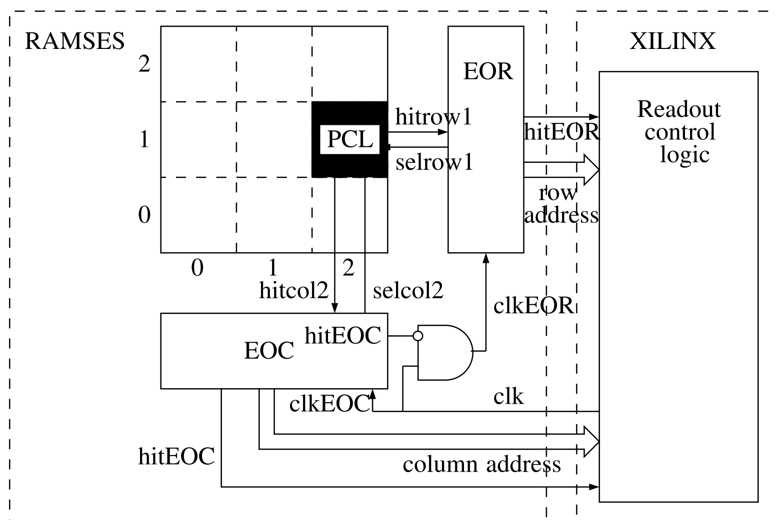

Figure 4.27: Block diagram of the readout logic

For the hit report and control of signal processing in the pixel a pixel control logic(PCL) is responsible. Hit pattern from the pixel matrix is transferred to End-Of-Row(EOR) and End-Of-Column(EOC) logics which choose a hit for the readout. These logics notify with *hitEOR* and *hitEOC* flags a Readout Control Logic(RCL) that the hit is present. The RCL implemented in the XILINX FPGA[10] generates clock pulses to complete the hit selection. Then this logic organises the readout of the selected hit by starting A/D conversion and storing the event data in the FIFO. In the following sections each component of the readout logic will be described in detail, finally the complete flow of the control signals during the readout will be given.

[10]Field Programmable Gate Array

4.7.1 Pixel control logic

The PCL implemented by Hausmann[Hau02] is shown in Figure 4.28. Initially the RS flip-flop is in a reset state: it means that its output Q is in a high state and $\overline{Q}$ is, correspondingly, low. It is also assumed that there is no other hits in the row or column to which the considered pixel belongs. It means that the $\overline{hitrow}$($\overline{hitcol}$) signal which is common to pixels from the same row(column) is pulled-up with a resistor(not shown) to a high state. Also it is assumed, that the considered pixel is not selected; with $\overline{Q}$ low it means that the peak detector is reset.

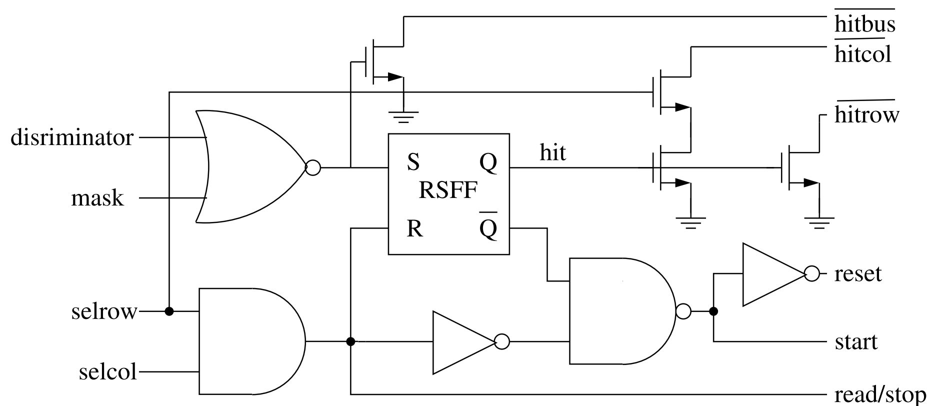

Figure 4.28: The pixel control logic

The discriminator signal, if not masked by a *mask* bit, reports a hit by setting the RS flip-flop. The $\overline{hitrow}$ signal goes immediately low, notifying the EOR logic. The $\overline{hitcol}$ signal will be reported after the row selection. The reasons for that will be explained in the following section. The peak detector is now active and the time measurement in the TVC is started.

After a certain time the hit pixel is selected by other logics resetting the RS flip-flop. The hit information is cleared, the time measurement is stopped and the output buffers are enabled, routing analog values of time and energy out of the chip. After these values are acquired the pixel will be de-selected, resetting peak detector and TVC, and thus becomes ready for the next event.

The *mask* bit is set by programming the pixel shift register. It helps to switch off discriminator outputs of noisy pixels. It is also useful for a threshold scan(see section 5.5), where the threshold of the discriminator is determined.

4.7.2 End-of-row and end-of-column logics

A detailed description and implementation of these logics is given in [Hau02]. Here only the explanation of their functioning will be given by considering of an example. The situation illustrated in Figure 4.29 shows the subsequent readout of three hits.

In the beginning the hit pattern is transferred to the EOR- and EOC-logics, a *hitEOR* signal, which is a wired-OR combination of all *hitrow* signals, reports a hit to the RCL(Figure 4.29a). Then the hit row with the largest address(3 in this case) is selected

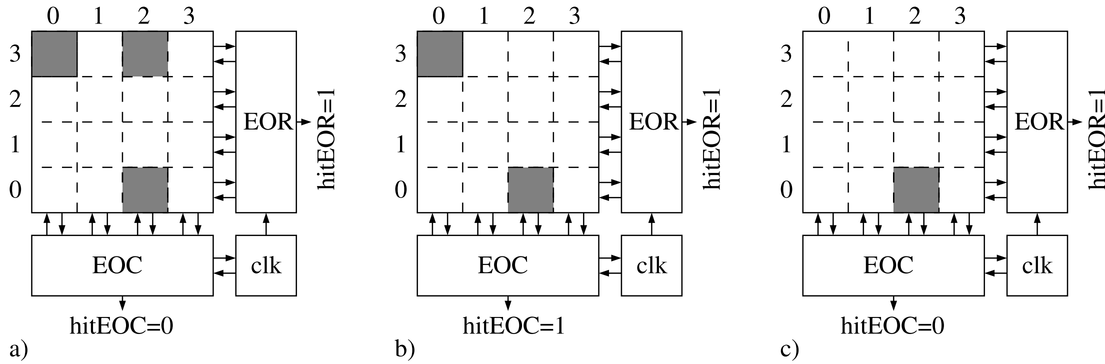

Figure 4.29: An example of a sequential readout of multiple hits

by a clock pulse. The hit column pattern from this row is sent to the EOC logic. This logic reports a hit to the RCL with the *hitEOC* signal, which is in turn a wired-OR combination of all *hitcol* signals. With the next clock pulse the column with the largest address(2) is selected. Thus the selection of the first hit - (3;2) in this example - is completed and its data and address can be acquired. Since the EOC is still reporting a hit (Figure 4.29b)- there is still one more in the row - the next hit (3;0) will be selected with only one clock pulse because the corresponding row was already selected. The last hit (0;2)(Figure 4.29c) will be selected again with two clock pulses.

To provide the readout sequence described above the readout clock, generated by the FPGA, has to be properly distributed between the EOR- and EOC-logics. The following scheme, which can be seen in Figure 4.27 is implemented. The *hitEOC* signal prohibits the clock distribution in the row as long as the EOC reports a hit. Thus no other row can be selected until all the hits from the selected row has been read.

Also the debug possibility for watching only the pixel of interest was foreseen. By loading the pixel address(row and column) into the dedicated shift register and completing the selection by a clock pulse the addressed pixel will be always selected independent on the hit pattern in the pixel matrix. The debug mode is entered by setting an *enable* signal in a high state.

4.7.3 Readout control logic

The readout control logic generates either one or two(if the hit row has to be selected) clock pulses for the hit selection, depending on the *hitEOR*, *hitEOC* signals, provided by the EORC-logic. After a certain delay, which is required for buffers to settle, the RCL initiates A/D conversion. A serial data stream coming from two ADC's is transferred into an 8-bit parallel stream and together with timestamp information and hit address is stored in the FIFO. The whole event occupies eight bytes: 12 bit energy value, 12 bit pixel time value, 24 bit time stamp and 10 bit hit address. Finally the pixel must be de-selected by an another clock pulse. The implementation of this logic in the FPGA is quite straightforward and therefore will not be described here. The whole signal run during the readout of a single hit is shown in Figure 4.30.

At the moment t_1 the CSA output signal reaches the threshold and the discriminator

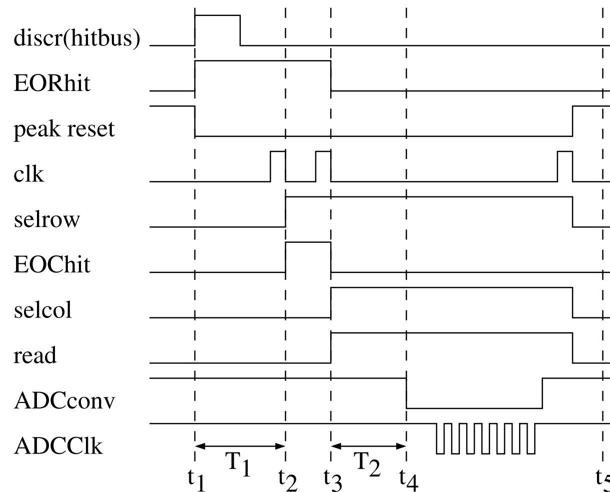

Figure 4.30: Readout of a single hit: control signals

fires, informing the EOR-logic, starting the time measurement and activating the peak detector. The readout control logic senses the *hitEOR* flag and generates a clock pulse. With the falling edge of the clock pulse at the moment t_2 the hit row is selected and the EOC is reporting a hit. With the second clock pulse(t_3) the hit selection is completed, the time measurement is stopped and analog values of the hit time and energy are routed out of the chip where they are sampled with the ADCs. It is important to this moment that the peak detector has really measured the maximum, which takes place when the time equal to the shaping time was elapsed after the hit(see section 4.3). Therefore a programmable delay T_1 was introduced which postpones generation of the readout clock. Another adjustable delay T_2 controls the moment of A/D conversion, which is started by applying *convert* and *clk* signals to the ADCs. After the conversion is completed and data are stored in the FIFO an additional clock is pulse de-selects the pixel, resetting the peak detector and TVC at the moment t_5.

4.8 The Digital-to-Analog Converter

Bias currents for the integrated circuits are supplied by 16 DACs, implemented on the chip[Hau02]. The block diagram of one DAC is shown in Figure 4.31. From the current, generated in the reference cell, eight binary-weighted current sources are created. These currents can be summed in various manners, depending on the 10-bit value held in the latch. This value can be changed by rewriting the DAC shift register and applying a *LOAD* signal. Eight from the 10-bits control the binary-weighted current sources and the last two serve for the coupling of the summed current to the DAC output. With these two bits three states are possible: no output current, the output current is equal to the summed current and the output current has some(maximal) value dependent only on the power supply. With the eight bit the output current I_{out} can be set from 0 to 160μA by a 625nA steps. The maximal current is about 230μA for 3V VDDA. The output current

can be monitored with an IMON structure which will be described later. To adapt the DAC current to the required value in the pixel a set of current mirrors was used.

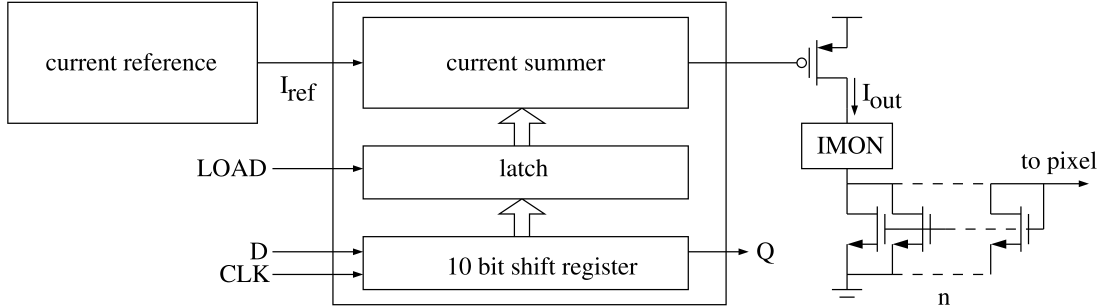

Figure 4.31: Block diagram of the Digital-to-Analog Converter

4.8.1 Current reference

The current reference cell without cascode transistors and start-up circuit is shown in Figure 4.32. To have a reference independent of the power supply bipolar transistors are usually used. In the CMOS process only lateral bipolar PNP transistors are available. A layout of such transistor is supplied with the process as a standard cell which dimensions cannot be changed. Nine lateral bipolar transistors were used in the reference cell - eight of them(T_{11}-T_{18}) have common terminals.

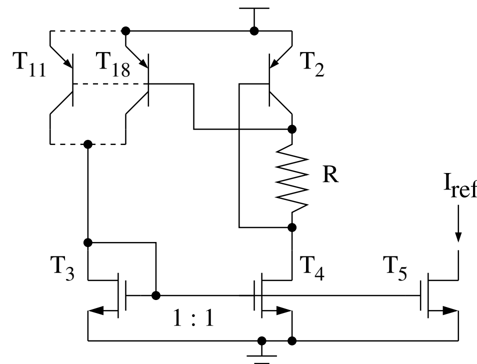

Figure 4.32: Simplified diagram of the current reference cell

The collector current I_{C1i} of each of transistors T_{11}-T_{18} and the collector current I_{C2} of T_2 are given by the following equations:

$$I_{C1i} = I_S e^{\frac{V_{BE1}}{V_T}} \tag{4.39}$$

$$I_{C2} = I_S e^{\frac{V_{BE2}}{V_T}} \tag{4.40}$$

where I_S is a saturation current of the base-emitter junction and $V_T = kT/q$ is a thermal voltage. Because the condition $8I_{C1i} = I_{C2}$ is forced by a MOSFET current mirror T_3-T_4 the reference current can be easily found:

$$I_{ref} = \frac{V_{be1} - V_{be2}}{R} = \frac{V_T(ln\frac{I_{C2}}{I_S} - ln\frac{I_{C1i}}{I_S})}{R} = \frac{kT}{qR}ln8 \tag{4.41}$$

Beside of the temperature it depends only on the resistance R, which for a $40\mu A$ current at room temperature was chosen to be $\approx 1.4k\Omega$.

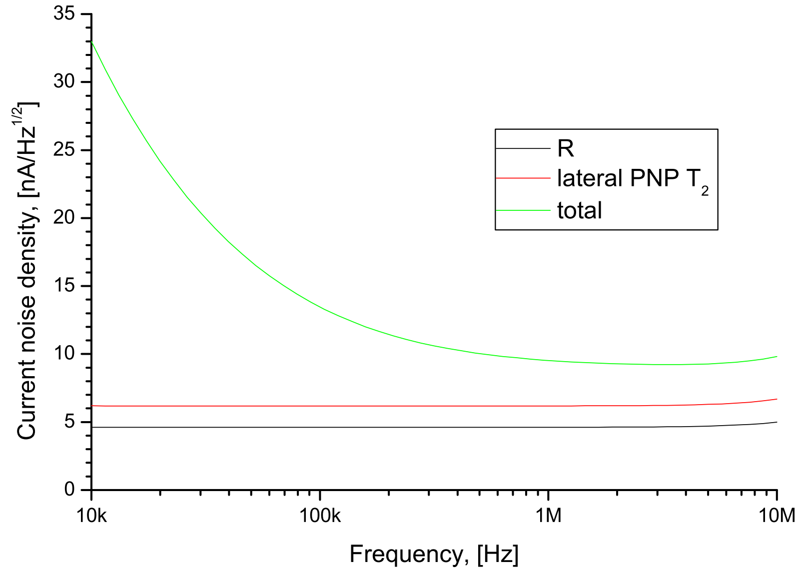

Figure 4.33: Noise of the reference current

The noise simulation of the reference cell shown in Figure 4.33 was performed with the SPICE simulator. It showed a quite large noise of $10pA/\sqrt{Hz}$ in the bandwidth of interest(100KHz-2MHz). The main contribution comes from the lateral PNP transistor T_2: the shot noise due to the collector current and the thermal due to the parasitic base resistance. As the geometry of the transistor is fixed and the reference current is set by the circuit demands, there is no way to reduce the noise in this configuration. It should be noted, however, that the simulation results are not completely reliable because of the parasitic nature of the lateral PNP transistor.

4.8.2 IMON structure

With an IMON structure two selectable DAC output currents can be monitored simultaneously. Also two different currents can be supplied externally, instead of using the DAC, to the selectable current mirrors. This is done by interrupting of the current path from the DAC to the current mirror with switches as shown in Figure 4.34. The switches are controlled by the two bits of the IMUX shift register. Sourcing or measuring external devices can be connected by using of four IMON pads.

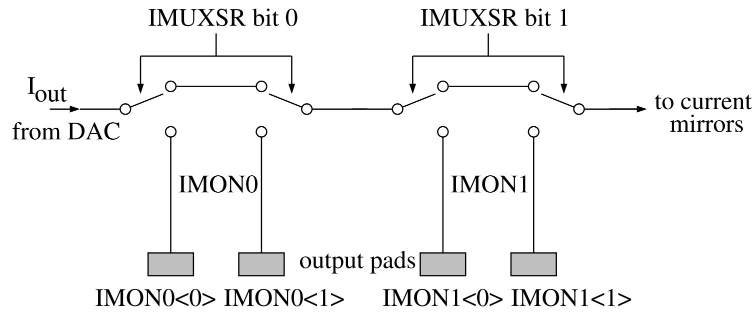

Figure 4.34: IMON structure

External current bias of RAMSES circuits is organised according to Figure 4.35. A current sourcing device has to be connected between VDDA terminal and the IMON0$<1>$ or IMON0$<0>$ pad. It has to be mentioned that the noise of the sourcing device, unless carefully filtered, will be also coupled to the circuits. By knowing the supply current and the pad voltage the current source I_{bias} can be replaced with an external resistor R_{ext}. Since there are only two IMON structures only two current biases can be supplied simultaneously in this way.

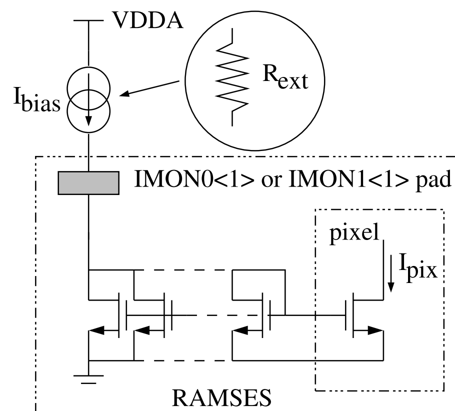

Figure 4.35: External current supply scheme for RAMSES circuits

Chapter 5

Measurements

In this chapter the setup used for test of the readout chip and for data acquisition is presented. Then the results of performance tests of each component of the RAMSES chip are given. The final section of this chapter presents spectra of γ-ray sources acquired with the RAMSES chip bonded to a Si-pixeldetector.

5.1 Setup for data acquisition

The setup for data acquisition mainly consists of the integrated electronics(RAMSES), two circuit boards(called supplementary PCB[1] and Silicon Solutions Blueboard), power supplies and a PC. A block diagram of the setup is shown in Figure 5.1.

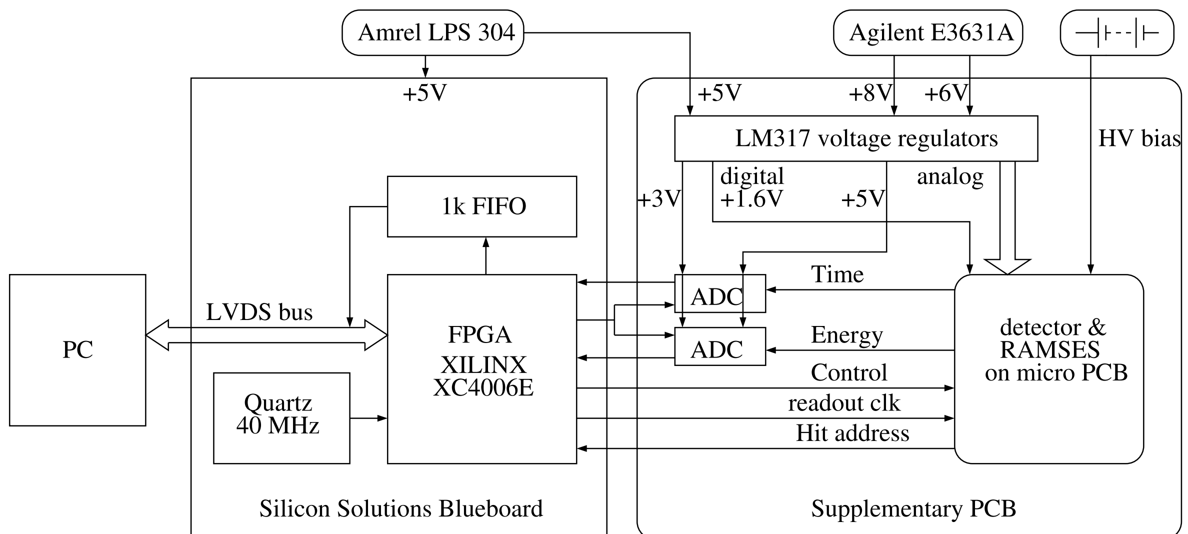

Figure 5.1: Setup for data acquisition

[1]Printed Circuit Board

The detector and its associated signal processing electronics(the RAMSES chip), shown in the lower right hand corner of Figure 5.1 are mounted on a micro PCB. A detailed photograph of this micro PCB is seen in Figure 5.2 The detector and the RAMSES chip are glued on separate metal layers and are connected via bond wires. Actually only one channel was connected due to difficulties with wire bonding. A total of 54 signal lines of the RAMSES chip are fanned out to a connector. The fanout has a pitch of $200\mu m$ on the bond side and of $1.27mm$ on the connector side.

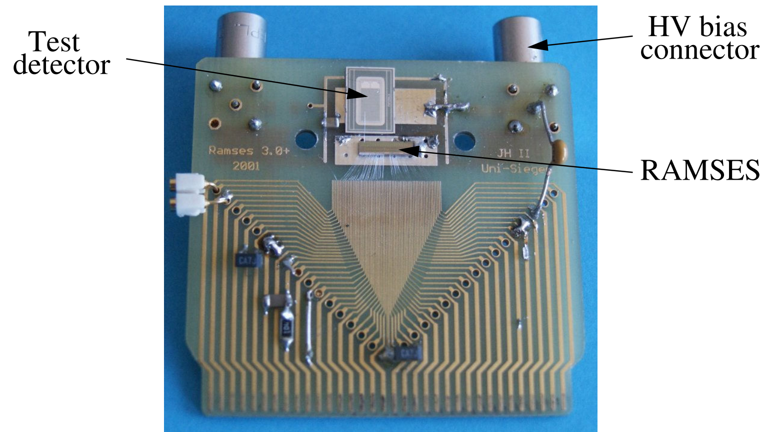

Figure 5.2: Micro PCB with the RAMSES chip and the detector

The micro PCB is attached to another board(supplementary PCB) which is housing two A/D converters, five voltage regulators, bypass capacitors and a 1:10 voltage divider for inject pulses.

The A/D converter is a high-speed, low-power, successive-approximation AD7495 from Analog Devices. It has 2.5V analog input voltage range and 12 bit resolution which corresponds to about 0.6mV/bit. Conversion error of one bit is equivalent to about $8e^-$ ENC which is far below the expected noise. With 1MHz throughput rate the ADC speed is more than sufficient for our application. The ADC's have a separate digital voltage supply. They operate correctly with the voltage set as low as 2.7V, minimising the disturbance to the analog electronics during a conversion cycle.

Stable voltages for the RAMSES chip, as well as for the ADC's are provided by LM317 voltage regulators powered by E3631A Agilent linear power supplies. The voltage can be regulated between 1.25V and a maximum, which is 2V below the voltage provided by the power supply. Several bypass capacitors are used with the voltage regulators for noise reduction and rejection of transients.

The supplementary PCB is plugged into the Blueboard. This board from Silicon Solutions was specially designed to test ASICs. It consists of a main board and an interface card. The main board houses a XILINX 4006E FPGA, an EPROM[2], a 1k FIFO, a 40MHz quartz and bus drivers. Through a LVDS[3] cable this board communicates with the PC at a maximum data transfer rate of 4MByte/s.

[2]Erasable Programmable Read-Only Memory
[3]Low Voltage Differential Signal

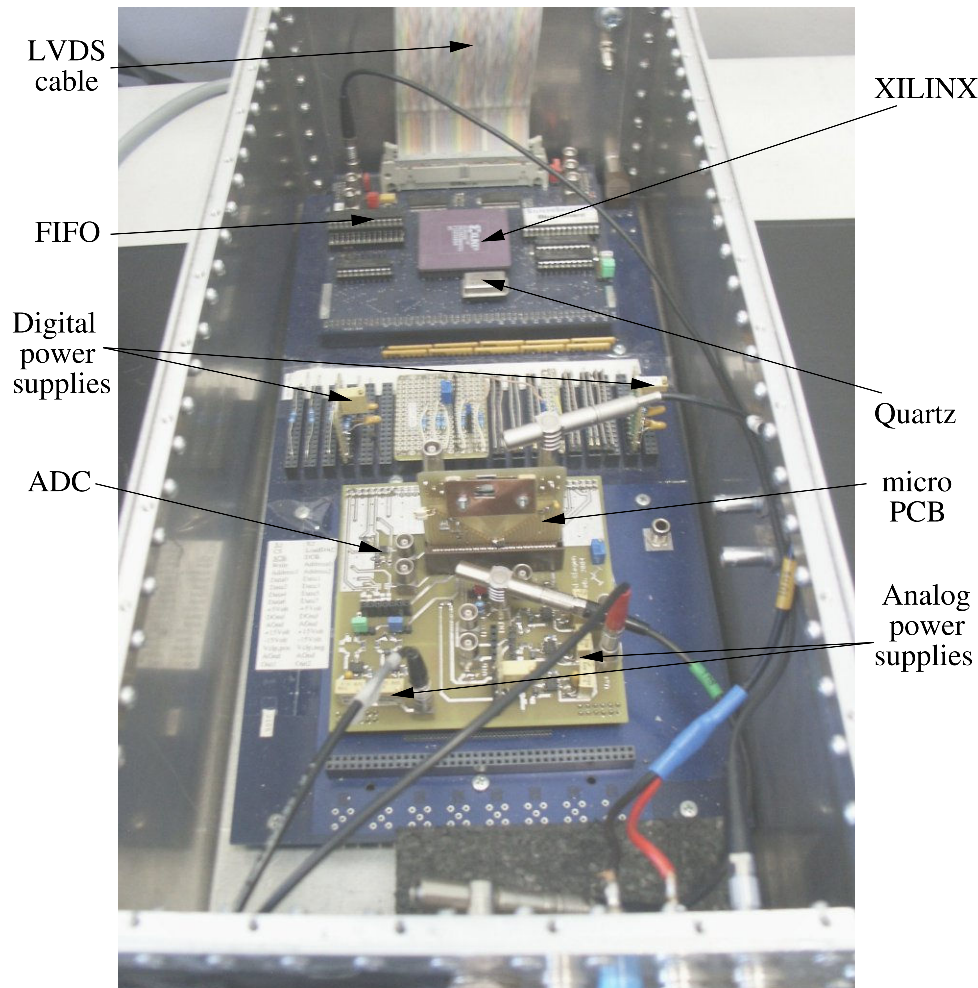

Figure 5.3: Blueboard and PCBs in Faraday cage

The digital power supply voltage(VDDD) of the RAMSES chip has to be as low as possible to prevent crosstalk of the digital signal to the analog circuitry. This is discussed in more detail in section 5.7. Typical voltages and current bias settings for the RAMSES chip are given in Appendix C. They are used throughout the measurements unless different values are mentioned in the text.

To ensure stable, spikes-free supply, high voltage bias for the detector was provided with batteries. The whole setup was placed in a Faraday cage. A photograph of the setup is shown in Figure 5.3. During data acquisition the Faraday cage is additionally covered with a black cloth to protect the detector from light.

For the purpose of chip test and data acquisition a custom software was developed; it is briefly described in Appendix D.

5.2 Performance of the CSA

The setup for testing the CSA is shown in Figure 5.5. The test channel is selected by an appropriate programming of the pixel shift register and the analog output multiplexer. The charge is injected into the CSA by a voltage step V_{inj} applied to the inject capacitor C_{inj}. The injected charge is then given by $Q = C_{inj}V_{inj}$. This charge is transferred by the amplifier to the feedback capacitor C_f. The discharge mechanism of C_f can be controlled by V_{feed}. The buffered output signal of the CSA is viewed and measured with a digital scope.

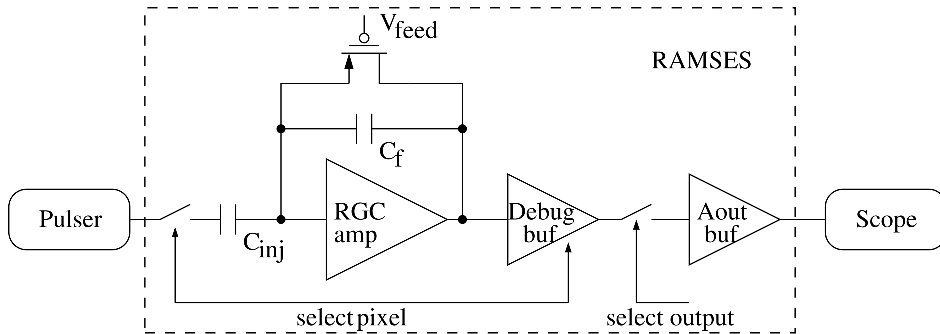

Figure 5.4: Block diagram for CSA test

It was found that the bias current of the CSA's input transistor, generated with the on-chip DAC10, is noisy, in agreement with the noise simulations of the current reference circuit in section 4.8.1. As an alternative the bias current was set by an external resistor between VDDA and the IMON0$< 1 >$ input (see Figure 4.35). The resistor value($10k\Omega$) was chosen to supply exactly the current used in the simulations. This remedy lead to about 20% of noise reduction.

The CSA response for different bias voltages of the feedback transistor is shown in Figure 5.6[4]. An expected linear discharge of the feedback capacitor can be seen. If the feedback bias is lower than 1.8V the CSA gain decreases because the discharge sets in before the pulse has reached its maximum; also the noise becomes larger. For a very high feedback bias($\approx 2.1V$) the equivalent feedback resistor becomes very large and the feedback cannot maintain the operating condition for the RGC amplifier. It should be noted that in the presence of a detector leakage current the maximal feedback bias is lower. The leakage current has to flow through the feedback transistor; therefore its resistance cannot be too high. From the slope of the discharge curve the discharge current can be calculated: $I_{dis} = C_f \Delta U/\Delta t$. For *Vfeed*=1.85V and C_f=2fF we obtain $\approx 7pA\ I_{dis}$.

Also the fall time dispersion among the pixels was analysed. The reasons for the dispersion are variations of threshold voltages of the input and feedback transistors and also variations of the bias current of the input transistor. The fall time was measured in 16 pixels with the same *Vfeed*=1.85V. The results are shown in Figure 5.8a. The relative variation is about 13%; no dependence on row and column number was observed.

[4]four time averaged data are shown

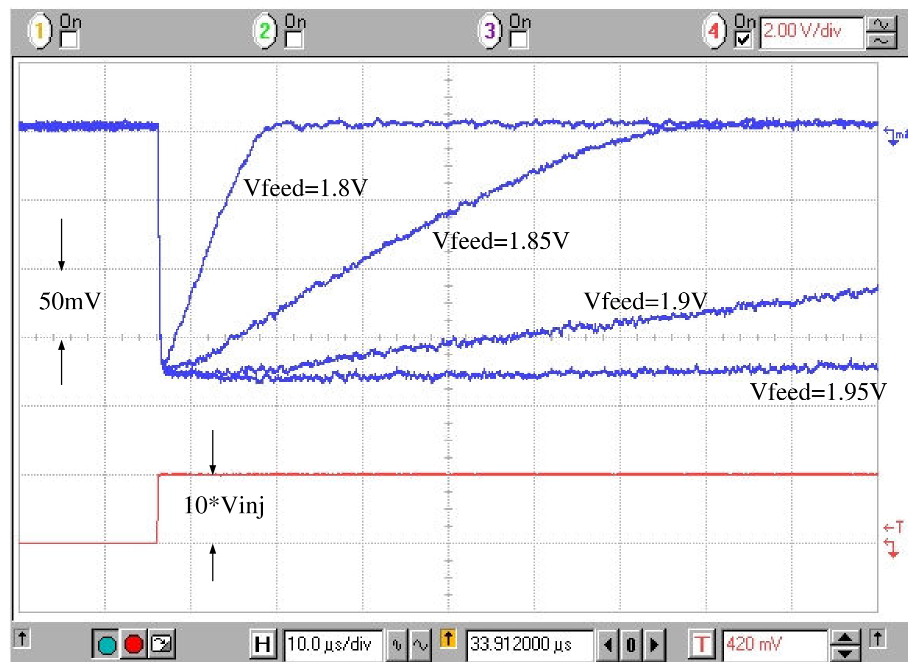

Figure 5.5: CSA output signal for different bias voltages *Vfeed* of the feedback transistor

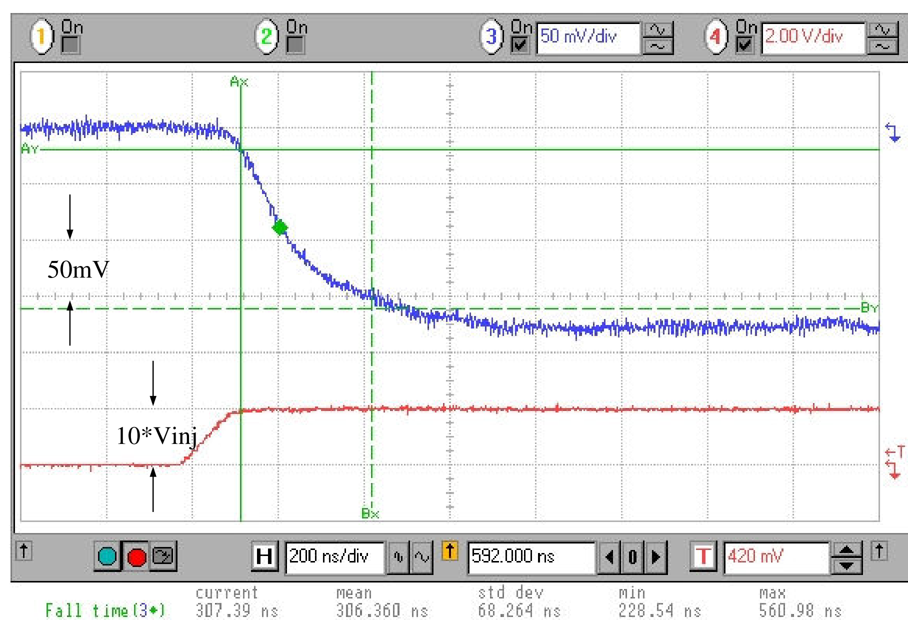

Figure 5.6: CSA output voltage for a voltage step input signal. The rise time is measured between the vertical green lines at 10%(90%) of the signal

The rise time was measured from the CSA response to a voltage step at the input. It is customly defined as the time required for a signal to change from 10% to 90% of its amplitude. With the highest possible *Vfeed* the rise time was measured to be $(306 \pm 68)ns$ as shown in Figure 5.7; it is consistent with the simulations. As was already mentioned in Chapter 4 this value is larger than calculated by equation 4.17 because of the effect of the compensation capacitor in the RGC amp.

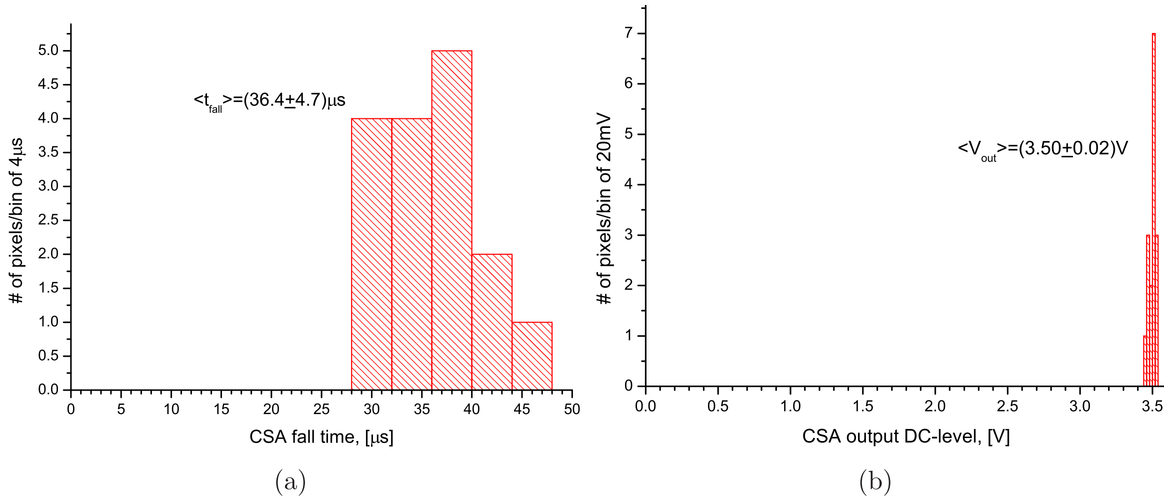

Figure 5.7: a) Fall time variation and b) DC-level variation of the CSA for 16 pixels

Also the spread of the CSA DC-output voltage among the pixels was measured as shown by a histogram in Figure 5.8b. This gives also information about the variation of the CSA DC-input voltages.

For noise measurements with the pulser it is important to know how much charge is injected into the CSA. Both the amplitude of inject pulse and the value of the inject capacitor have to be known precisely. Pulse amplitude can be easily measured with the scopes probe close to the chip, the value of the inject capacitor is known only from the layout extraction. It is also known that the extracted value can vary by about 10% due to process variations. The CSA was wire-bonded to a detector and calibrated with γ-ray sources.

For the wire-bonding an aluminium wire of $\phi = 17\mu m$ was used. The value of the inject capacitor can be calculated from the response to a voltage step pulse if the amplifier is calibrated. Calibration was made by wire-bonding the CSA to a detector illuminated with γ-ray sources. As can be seen in Figure 5.9a both the bump bond pads with $\phi = 45\mu m$ on the chip side and with $\phi \approx 10\mu m$ on the detector side are too small for wire-bonding. The structures in their neighbourhood can easily be damaged by the bonding process.

After successfully bonding one pixel the response to the inject pulse was recorded together with ^{109}Cd source spectrum. The found value of the inject capacitor is compared to the extraction from the layout and given in Table 5.1.

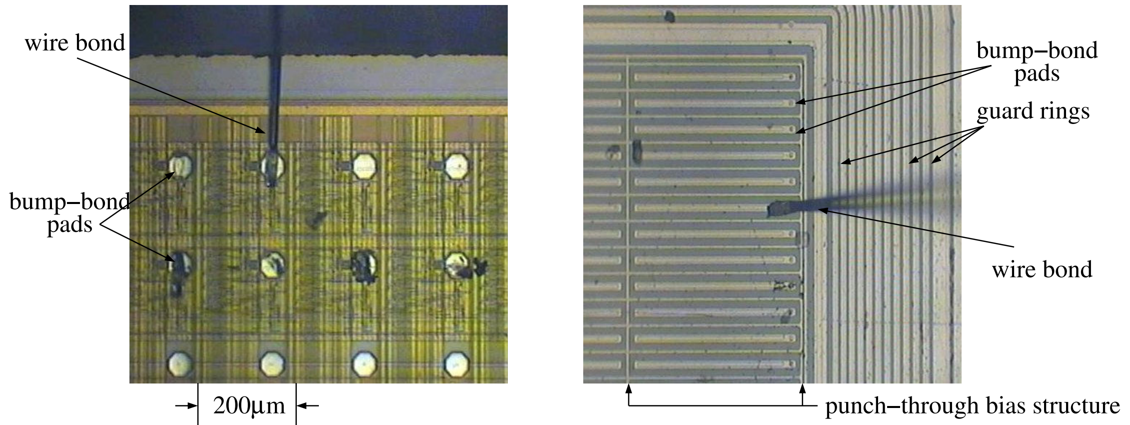

Figure 5.8: Microphotograph of the wire-bond connection: a) chip side b) detector side

Measurement	extracted	γ source
value, [fF]	1.80	1.55

Table 5.1: Value of the inject capacitor

5.3 Performance of the shaper

Test setup for the CRRC shaper test is shown in Figure 5.10. The test channel is selected by the program. A 200mV voltage step is applied to the inject capacitor, which corresponds to the injection of about 1900 e^- into the CSA. The shaper response for different shaping times(set by DAC6) is shown in Figure 5.11.[5] As can be seen, the shaping time is adjustable in the $(0.4 \div 2.9)\mu s$ range.

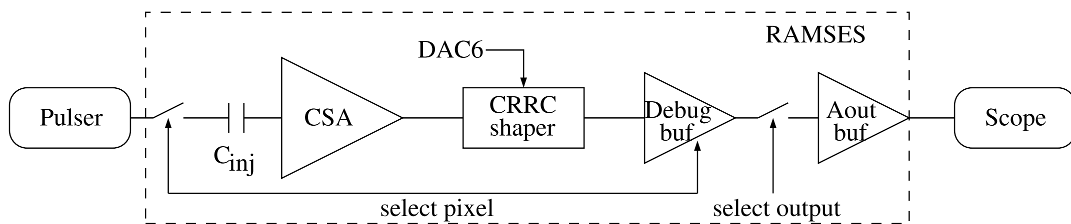

Figure 5.9: Block diagram for shaper testing

Variation of the shaping time among pixels for the same DAC6 setting(DAC6=5) and the same injected charge is shown in Figure 5.12. The relative deviation is 13% r.m.s.

Long shaping times, however, can be obtained only for small pulses. For large pulses, as expected from the circuit analysis, the shaping time remains small.

Because of the difficulty to obtain large shaping times an external shaper amplifier ORTEC 572 was used to analyse the noise performance of the CSA. Its gain can be

[5]Four times averaged data are shown for better viewing of the shaping time

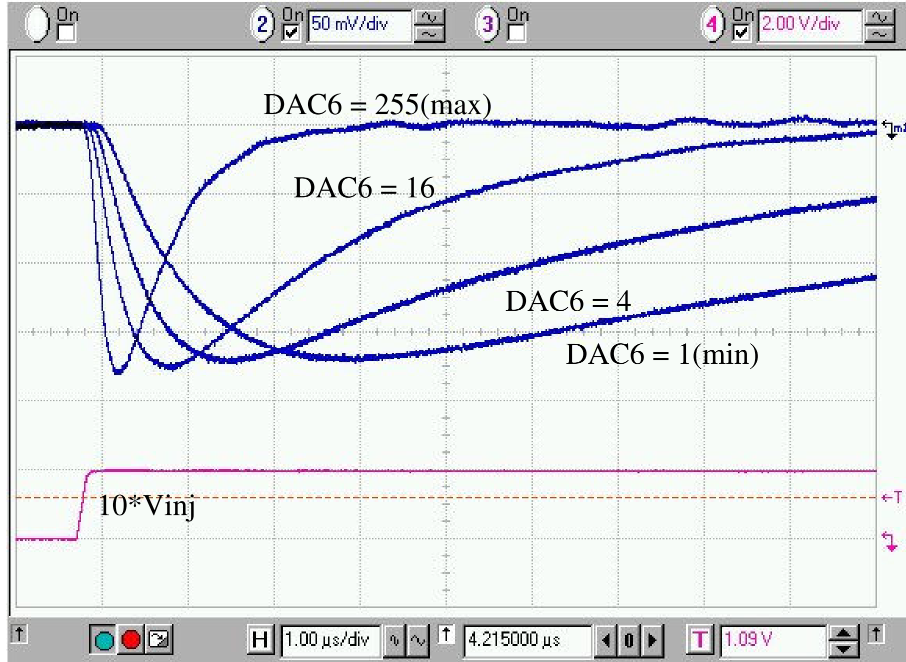

Figure 5.10: Shaper output signal for different DAC6 settings

adjusted in the range from 10 to 1500 and the shaping time can be set to $1.2\mu s$, $2.2\mu s$, $4.4\mu s$, $6.6\mu s$, $13.2\mu s$ and $22\mu s$. The setup employing the external shaper is shown in Figure 5.14 where an additional external buffer[Nic03] was used in order to drive $1k\Omega$ input impedance of the shaper.

The following method of noise measurement was employed. A continuous pulse train of the same amplitude V_{in} was applied to the inject capacitor and the amplitude of shaper output signal V_{amp} was measured with the scope. The injected charge, multiplied with the ratio of the output amplitude variation to its mean value yields the equivalent noise charge Q_n, given as:

$$Q_n = \frac{C_{inj}V_{in}}{q}\frac{\sigma_{Vamp}}{< V_{amp} >} \tag{5.1}$$

The noise measurement was performed for different shaping times for the CSA, once with open input and once with the CSA wire-bonded to the detector. Then the measured data were corrected for noise of the buffers. Noise contribution of buffers was found by switching off the CSA(either by increasing V_{feed} beyond the CSA's operation range or by switching off the current bias of the CSA's source follower) and measuring with the scope the ac r.m.s. voltage at the output of the external shaper. Knowing amplification of the test chain from the previous measurement a noise figure of $Q_{n,buff} \approx 4e^-$ was obtained. The corrected data were then fitted with the following function:

$$Q_n = \sqrt{a\tau + \frac{b}{\tau} + c} \tag{5.2}$$

This function reflects different dependencies on shaping time of the three main noise

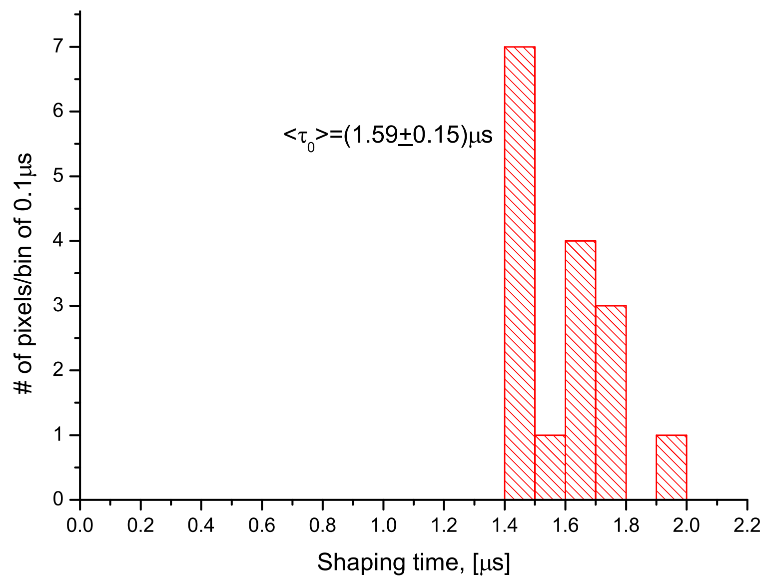

Figure 5.11: Shaping time variation for 16 pixels

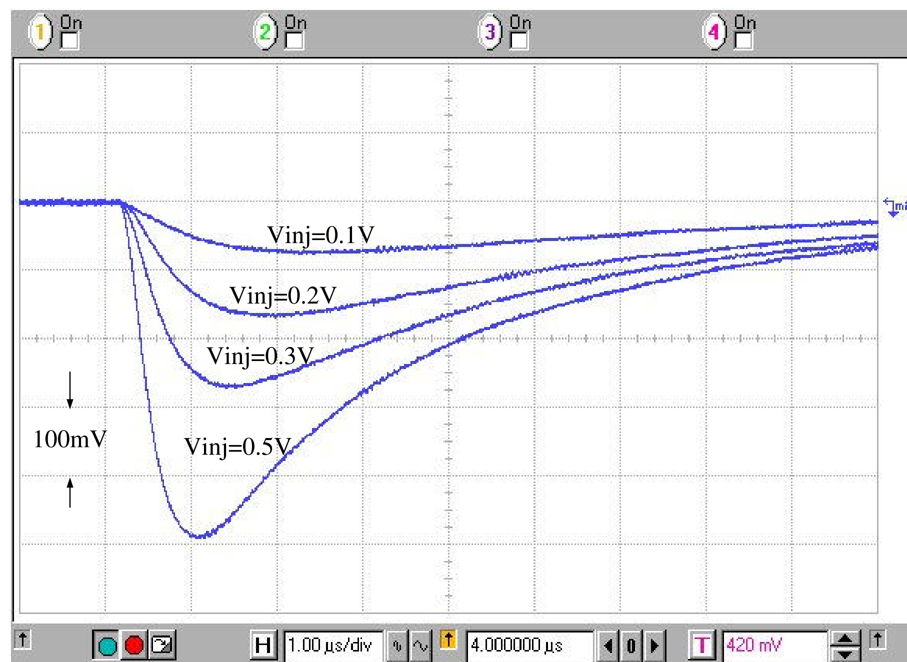

Figure 5.12: Shaper output signal for different amplitudes of the inject pulse

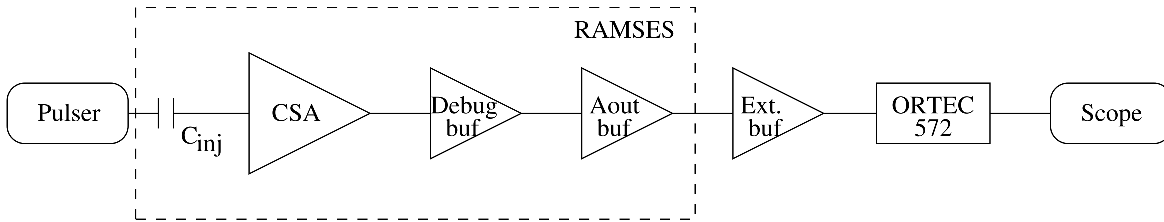

Figure 5.13: Setup used for the measurement with the external shaper

mechanisms as given by equations 4.9,4.10 and 4.26. Measured data together with the fits are shown in Figure 5.15. For the bonded CSA the noise is larger because of the additional capacitance at the input. The linear increase of the noise at longer shaping times reflects the presence of the detector leakage current. From the parameter a_b the leakage current was calculated using equation 4.26[6]. The value of (8.7 ± 1.3)pA is in agreement with expectations. The minimal noise, $\approx 50e^-$, is about 60% larger than estimated in Chapter 4. From the parameter c_b the flicker noise contribution can be calculated, it is $33.8e^-$, 68% of the minimal noise.

Both curves show larger than expected serial and flicker noise. Larger serial noise causes the shift of the optimal shaping time to about $5\mu s$.

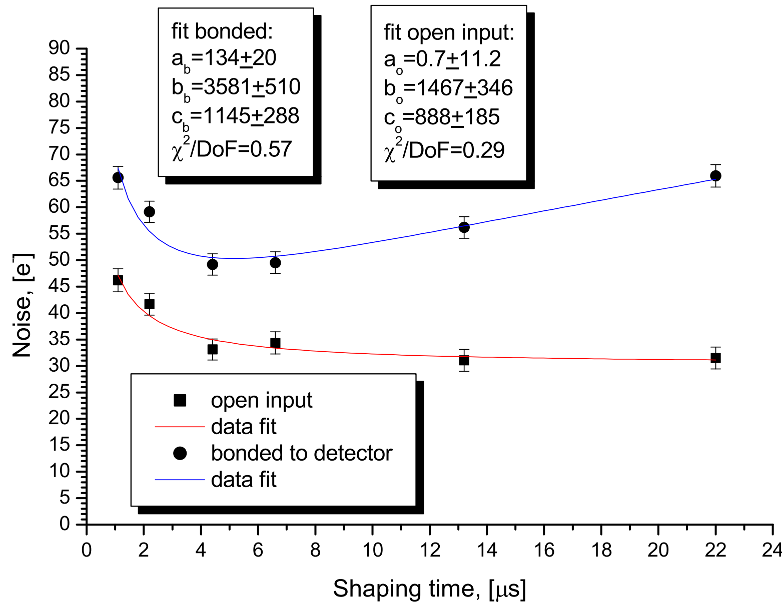

Figure 5.14: Noise as a function of shaping time for the CSA with open input and for the CSA bonded to the detector

The reason for the discrepancy is probably the layout of the power supply for the CSA

[6]This equation was derived assuming a CRRC-shaper(first order Semi-Gaussian) but the ORTEC shaper is a second order Semi-Gaussian. Therefore coefficient of 1.07 was used instead of coefficient 1.57 in the calculations - more about S-G shapers can be found in [Cha97]

in the readout chip. As was already discussed in Chapter 4 it is very important to have low-noise supply for the input stage. The supply is provided with LM317 regulator(see section 5.1) which is actually not optimal in terms of noise. But the real problem may be that the CSA's use the global analog power supply bias VDDA. This voltage is common to all other analog circuits and even small variation in current consumption somewhere in the chip can affect the input stage. A separate voltage supply for the CSA would therefore seem appropriate.

5.4 Performance of the peak detector

The peak detector detects the maximum of a shaper signal and holds it on the dedicated capacitor. The speed of the peak detector response is determined by its bias DAC3; setting of 200 is sufficient for the whole range of signal amplitudes and shaping times used. For confirmation the peak detector output to two different input signals from the shaper is shown in Figure 5.16.

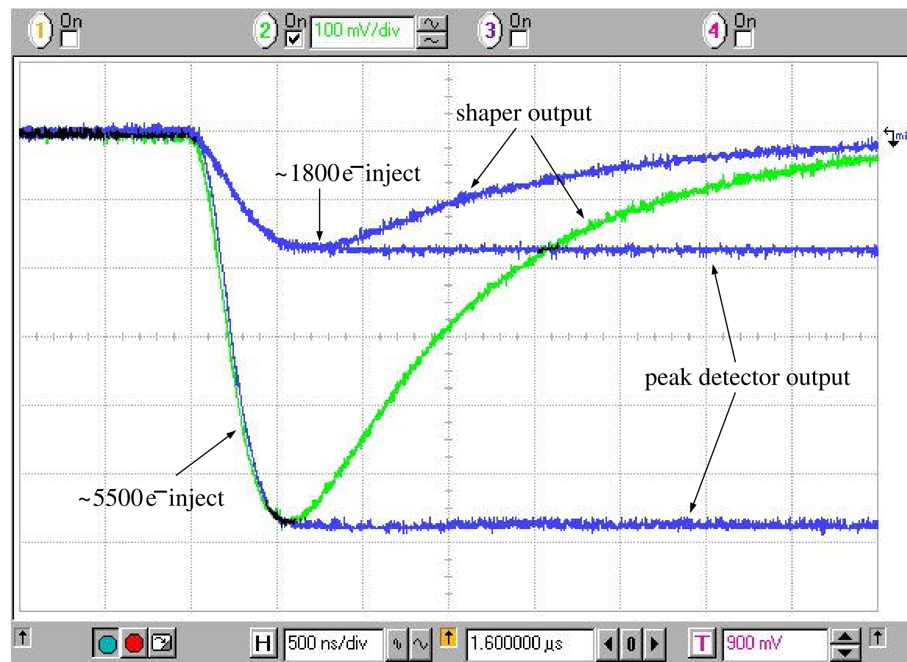

Figure 5.15: Peak detector response for two different input signals

It is important to know how long the peak detector can hold the detected value, because leakage current of the reset switch causes a drift. The drift was measured for two cases: with the readout chip exposed to the light and covered with a black cloth. From the measurement shown in Figure 5.17 the leakage current I_L was estimated assuming 548fF(524fF designed + 24fF parasitics) peak detector capacitance. In the case with light the leakage current(I_L = 6.9fA) is slightly larger than in the case without light(I_L = 4.6fA). The difference comes from additional electrons generated by the light in the tiny

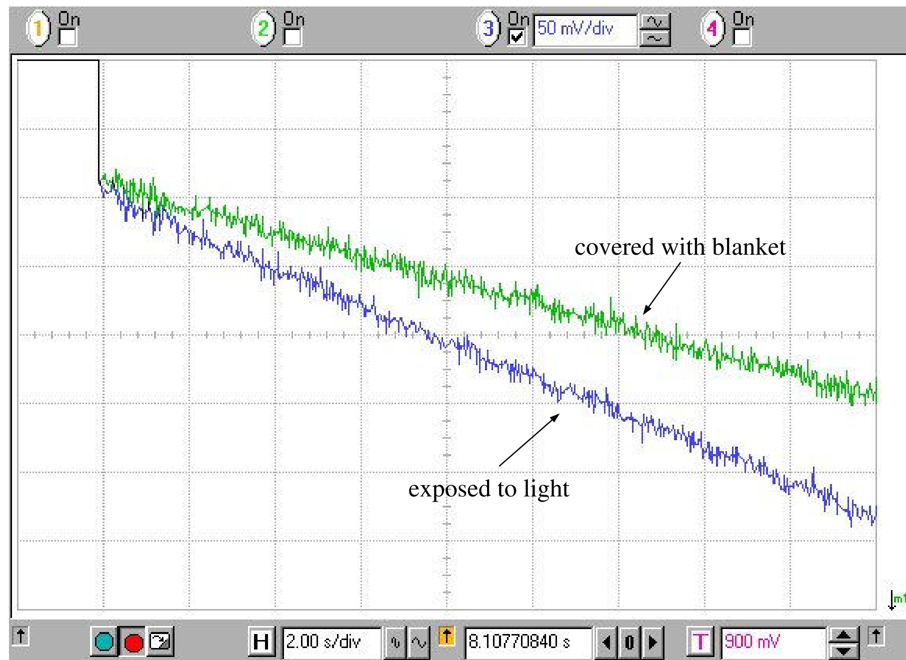

Figure 5.16: Drift of the peak value

parasitic diode of the NMOS switch. For the relevant time scale of $10\mu s$ the drift will be only 0.2μV, which is negligible.

5.5 Performance of the discriminator

Each discriminator of the RAMSES chip can be tested separately. For the test the charge injection into selected pixel has to be enabled and a voltage pulse applied. If the injected charge is above a preset threshold the discriminator will produce a logic pulse. This pulse can be seen on the *hitbus* output of the RAMSES chip with all other discriminator outputs masked.

In total three on-chip bias DACs and a five-bit threshold adjustment circuit affect the discriminator performance. The comparator bias DAC8 determines the response speed of the discriminator, which is about $200ns$ for a DAC8 setting of 200. Because of the constant level discrimination the response speed slightly varies with input charge. For example for a 150mV inject pulse($\approx 1450e^-$) the rise time is $\approx 30ns$ larger than for a 800mV inject pulse.

The threshold level is set by DAC7. Unfortunately low thresholds cannot be set by DAC7 because the range of DAC7 was not well chosen. Different methods were therefore applied to obtain low thresholds.

- for short shaping times DAC7 is switched off, threshold is set and adjusted by a five bit threshold code
- for long shaping times DAC7 is switched off, threshold is set with the external

current supplied by a resistor (10MΩ) connected to IMON1 structure(see Figure 4.35). Almost no adjustment is possible.

The measurement of thresholds is commonly done by a so-called threshold scan. By this method a fixed number of pulses of same amplitude is applied to the CSA and the number of the discriminator responses is counted. Then this procedure is repeated with a continuously increasing amplitude of the inject pulse. The percentage of triggered events as a function of input charge is measured. Ideally one would expect a step function with zero counts below the threshold and 100% above. Due to the presence of noise the step function is smeared. Because the noise has a Gaussian origin the resulting distribution will have a form of the Gauss' error function, which is given by equation 5.3.

$$erf(x) = \frac{1}{\sqrt{2\pi}\sigma} \int_{-\infty}^{x} e^{-\frac{(t-\mu)^2}{2\sigma^2}} dt \tag{5.3}$$

with μ being the threshold and σ being the r.m.s. noise.

To perform the threshold scan the setup shown in Figure 5.18 is used. Firstly the pixel of interest is selected and the threshold is set. All other pixels are masked. A pulse train of 127 pulses generated in the XILINX is used to trigger the pulse generator. It is programmed to deliver a single pulse with the amplitude set by the program through IEEE interface. Once the discriminator fires, the counter value increases. After a single measurement the counter is read and reset; the percentage of hits is calculated. A dead time of about $100\mu s$ is introduced in the chain to exclude possible additional hits due to noise or crosstalk. An example of a threshold scan is shown in Figure 5.19.

Generally to find out threshold and noise from the scan plot it has to be fit with the Gauss' error function. To simplify the calculations the threshold is taken as the input charge corresponding to a 50% value; the noise is found by the following formula: $\sigma = 1/\sqrt{2\pi}k$, with k being the slope of the function $erf(x)$ at $x = \mu$. The parameter k is found as a slope of the line drawn through the points of the closest approach to 20% and 80% respectively, as shown in Figure 5.19.

By using of the threshold scan method the threshold dependence on a five-bit threshold adjustment code was measured with DAC6=100,DAC7=0 for a single pixel. The dependence is shown in Figure 5.20; it is similar to the simulated one(Figure 4.25). An inherent threshold of about $400e^-$ can be seen; also a quite large gap of $\approx 350e^-$ between the codes 15 and 16 has to be mentioned, which can make difficult an accurate threshold adjustment.

The minimum threshold, which corresponds to the threshold code of 31 was measured for 16 pixels with DAC6=50(corresponds to the $\approx 0.75\mu s$ shaping time). The results are shown in Figure 5.21a. It can be seen that except for the pixel 57 all other pixels have an inherent threshold which in the extreme case(pixel 25) can be as large as $1250e^-$(4.5keV in Si). The inherent threshold is caused mainly by the voltage drop on the "on" -resistance of the NMOS switches as was already discussed in section 4.5.

Then by change of the threshold code the individual pixel thresholds were adjusted to $\approx 1160e^-$ and threshold scan was performed again. From the results, shown in Figure 5.21a, it can be seen that for some pixels(25 and 60) no adjustment is needed, whereas for the other(57) the adjustment is not sufficient - in the case of the large noise this pixel

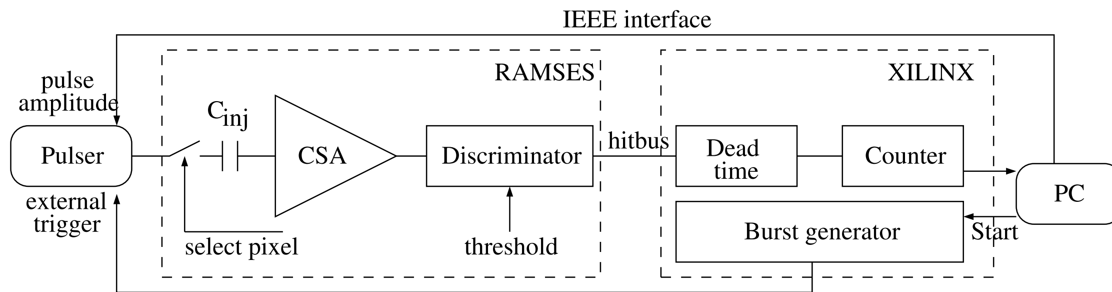

Figure 5.17: The setup used for threshold scan

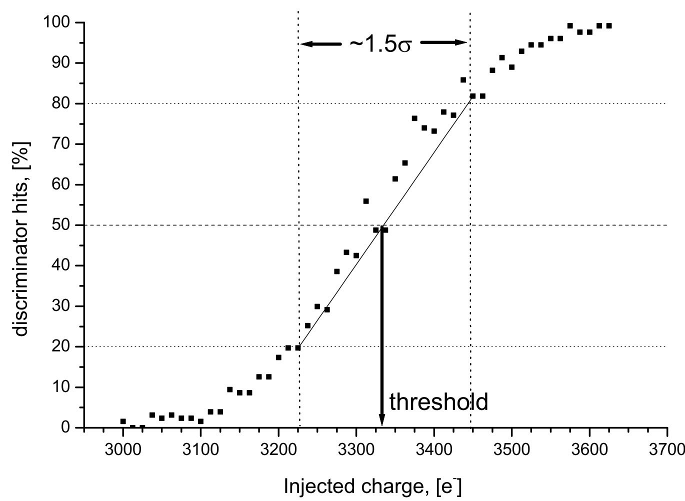

Figure 5.18: Threshold scan of a pixel; determination of the threshold and the noise

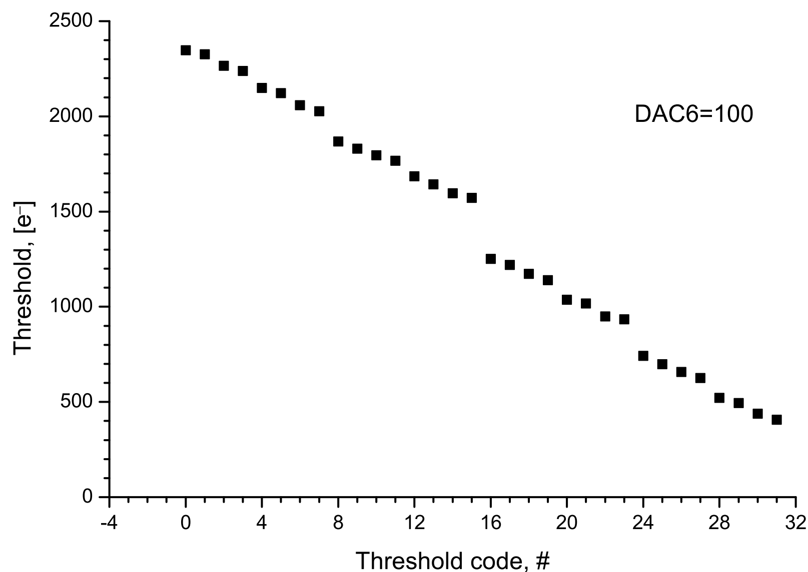

Figure 5.19: Threshold dependence on the adjustment code with DAC6=100

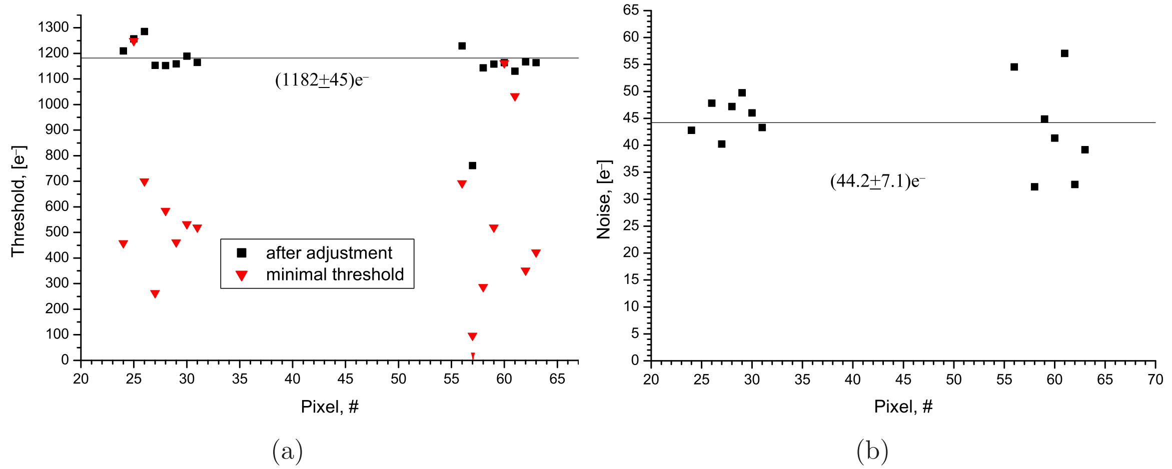

(a) (b)

Figure 5.20: a) Minimum threshold with DAC6=50 for 16 pixels; threshold after adjustment to 1200e^- for 16 pixels b) Noise obtained from threshold scan for 16 pixels

should be masked. For the pixel 26 a good adjustment could not be achieved because the threshold lied in the gap between the codes 15 and 16.

The noise found from the threshold scan is shown in Figure 5.21b. Mean value of 44.2e^- is in good agreement with the result previously obtained with the external shaper.

5.6 Performance of the Time-to-Voltage Converter

Time measurement range depends on the expected hit rate; if the rate is high a larger measurement range has to be chosen; for low rates a smaller range is sufficient. The range depends on the discharge current, which is set by DAC1. The discharge of the TVC capacitor for different DAC1 settings is shown in Figure 5.22, where the input charge sufficient to trigger the discriminator was applied without a *stop* signal.

From the slope of the discharge curve and by knowing the discharge current the value of the TVC capacitor can be calculated. For DAC1=10 the measured output current is I_{out} = 6.076μA, which correspond to the discharge current in the pixel: $I_{dis} \approx I_{out}/128$ =47nA. Thus $C_{TVC} = I\Delta t/\Delta U \approx$ 998fF which is 92% of the extracted value(1085fF). It is noted that with increasing of the range the time resolution becomes smaller. With 0.6mV corresponding to an ADC bit the resolution is 13ns on the 50μs interval. So the optimum between the range and resolution have to be found.

Because of the offset introduced by the source follower used as a buffer in the TVC the output range is about 1V shorter; this is also limits the time measurement range. Signal flow during the measurements of the two different time intervals in the same pixel is shown in Figure 5.23. As can be seen the TVC capacitor discharge starts about 200ns after the charge injection since the signal needs some time to cross the discriminator threshold. With the application of the *stop* signal the TVC output voltage is available on the analog TVC bus where it can be sampled and converted by the ADC. Once again the time of about 200ns is needed for the output to settle because of the switching of the buffers.

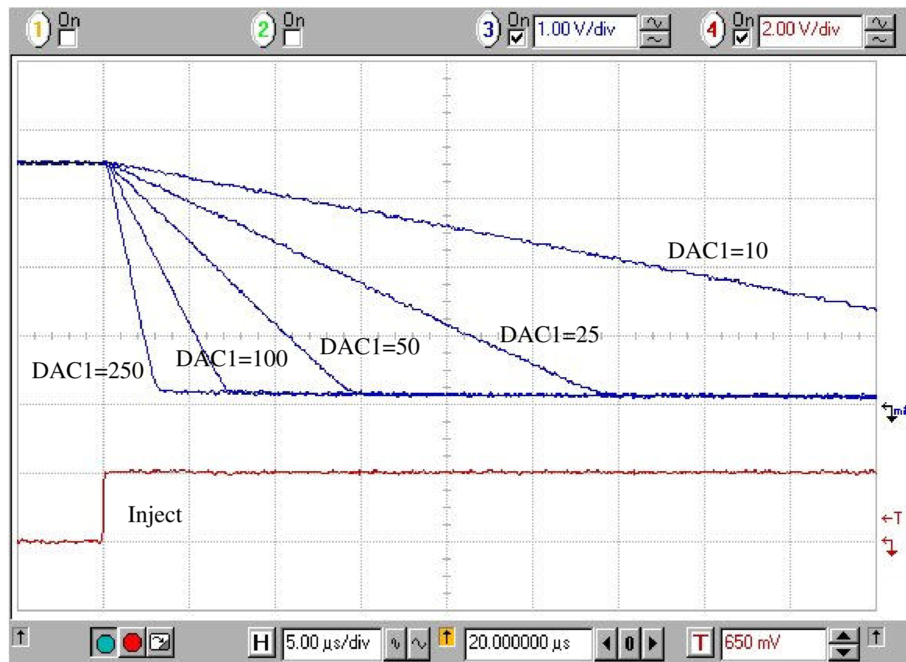

Figure 5.21: TVC range selection

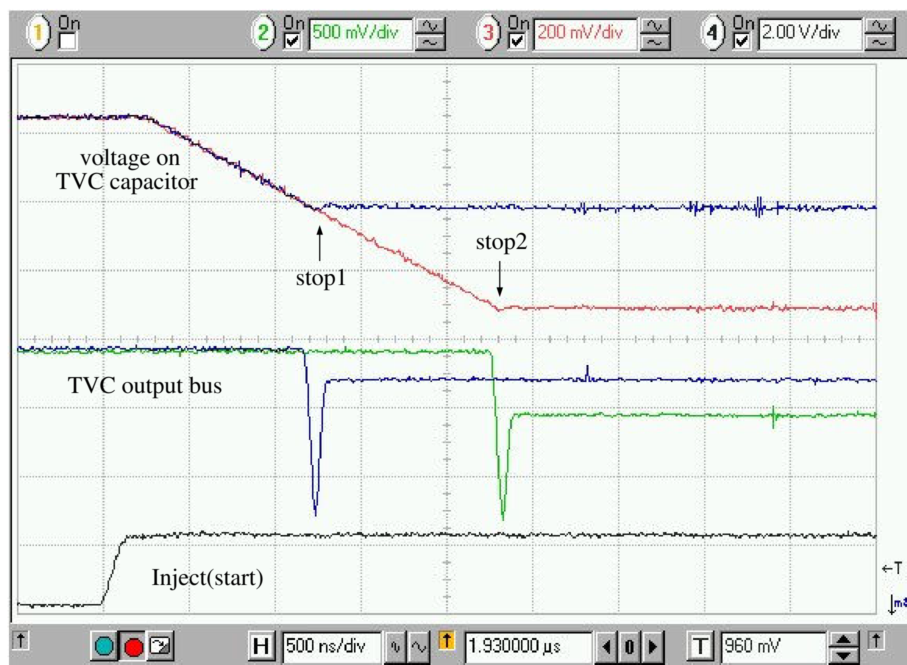

Figure 5.22: TVC output for two measured time intervals

5.7 Performance of the data acquisition circuitry

First of all the functionality of the data acquisition circuitry was checked. For that purpose an acquisition channel was selected by the program, the discriminator threshold was set and charge was injected into a CSA. If the injected charge was above the threshold, a hit was recognised and acquired. The signal flow during the readout of a single hit is shown in Figure 5.24[7].

As soon as the discriminator fires, the *hitrow* flag is set and the peak detector samples the shaper output. The *hitrow* flag initiates generation of readout clock pulses(*clk*) by the FPGA after an adjustable delay. With the falling edge of the first clock pulse the hit row is selected, setting the *hitcol* flag. This flag triggers the second clock pulse, which completes the hit selection; the *read* signal goes high and the saved analog value of hit pixel appears at the *analog output* of the chip. Because of switching of the buffers(large spike on the analog output) the output voltage needs some time to settle, therefore an another adjustable delay is introduced. Then the analog value is sampled by the ADC and converted. After the end of conversion the pixel is de-selected with an additional clock pulse; thus it becomes ready for the next event.

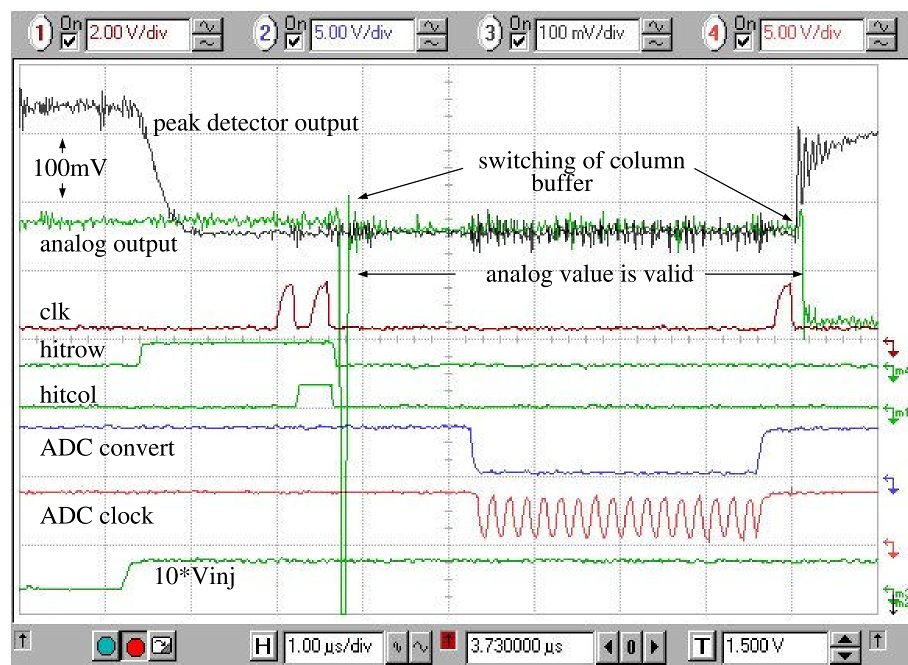

Figure 5.23: Signal flow during readout of a single hit

Prior to the energy measurement a peak detector must be reset. It means that its capacitor is pre-charged to some value, called a pedestal, which is equal to the DC-output value of the shaper. This value have to be subtracted from the measured one to find out the true signal amplitude. Pedestals were measured as a function of shaper bias for 16

[7]the same scale and offset for the analog signals(peak detector output and analog output) are used

pixels and the results are shown in Figure 5.25. As can be seen, for large shaping bias the output range becomes shorter.

Also the linearity of the data acquisition circuitry was investigated by measuring the voltage, acquired by the program, as a function of input charge. A sample of this measurement[8] in one pixel is shown in Figure 5.26a, where a good linearity up to about $6500e^-$ of input charge can be observed. From the slope of the straight line fit the gain of the data acquisition circuitry can be obtained. The same measurement was performed for 16 channels and for each channel the gain was calculated; a histogram of the gain variation for 16 pixels is shown in Figure 5.26b. It should be mentioned that the linear range can be increased by increasing the analog power supply voltage VDDA.

An especially important and critical point is the crosstalk between readout channels. Here under the crosstalk any activity connected with a signal processing in a hit pixel and its readout, leading to a signal in neighbouring pixels is meant. Three components of the crosstalk can be distinguished: the crosstalk caused by the pixel electronics, the crosstalk owing to the digital signals during readout and the crosstalk due to the analog signal processing outside of the pixel array in the RAMSES chip.

The crosstalk due to the pixel electronics can be measured by a procedure similar to the threshold scan, described in section 5.5; the only difference is that the charge is injected in one pixel and the threshold is measured in the neighbouring. Since the response of the discriminator is obviously dependent on the preset threshold, the threshold value is used for the normalisation. For example, if in the pixel with the preset threshold of $1000e^-$, a threshold of $10000e^-$ is measured by injection in the neighbouring pixel, it means that 10% of the charge from the neighbouring pixel was transferred. Applying this procedure a very small crosstalk below 2% was obtained. However, this measurement have to be performed again after the bump bonding of the RAMSES chip to a detector, since the coupling capacitance between pixels will increase and therefore the crosstalk is expected to be larger.

Other two crosstalk effects were studied by the analysis of data, taken by the program, at different thresholds, all far above the baseline noise. To have equal conditions in all channels the thresholds in different pixels were adjusted and charge was injected in only one selected channel.

Effect of digital readout signals was investigated by change of the fall time of some digital signals(*hitcol, hitrow*), which can be regulated by DAC13, and by variation of the digital power supply VDDD. The obtained crosstalk was found to be very small and could be neglected.

Another disturbance increasing with injected charge and independent on the distance to the inject pixel was discovered. It is connected with the switching of the column buffers used to drive the analog output bus; once a pixel from the column is selected for the readout the corresponding buffer is enabled. Switching of buffers results in the fast recharge of the analogbus capacitance, as seen in Figure 5.24, which cause crosstalk to the CSA's through the substrate. Re-layouting of the analogbus and the shielding of the bump-bond pads is the only way to reduce this crosstalk. Anyway it was found that the threshold of $1500e^-$ is sufficient for the operation in the whole energy range without

[8]This measurement was performed with 3V VDDA power supply

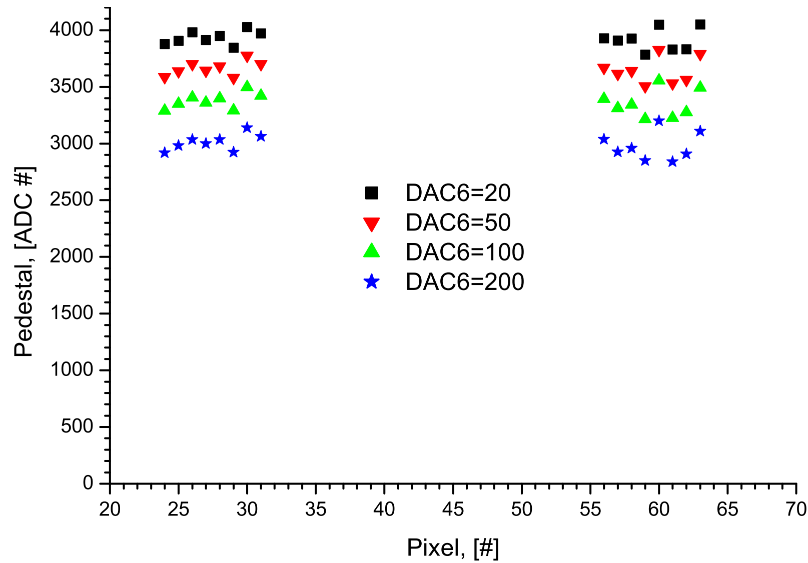

Figure 5.24: Change of pedestals with shaper bias for 16 pixels

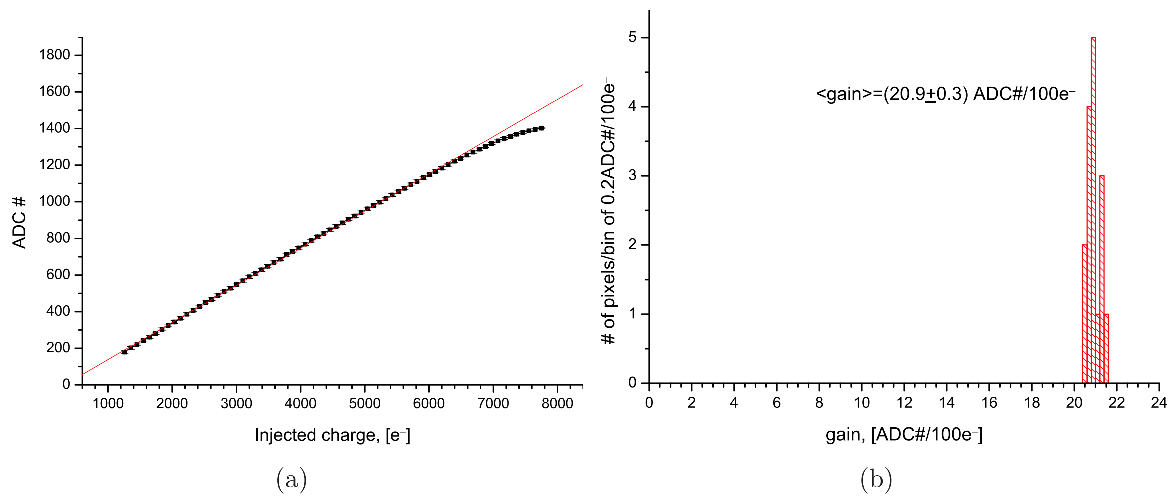

Figure 5.25: a) Sample of the linearity scan b) Gain variation for 16 pixels

having any parasitic hits.

With the wire-bonding of the RAMSES chip to the detector the crosstalk increases since the parasitic capacitance between the CSA input and the substrate becomes larger. Because of the damage caused by wire-bonding to the bump bond pad this phenomenon was not studied in detail. Since the effect of digital readout signals becomes also more pronounced, the digital power supply VDDD has to be set to the lowest possible value - 1.6V, which makes the digital crosstalk negligible.

5.8 Performance of the test detector

To test the readout electronic a silicon p^+n pixeldetector was used. The detector consists of an array of 47×10 rectangular pixels, each of $\approx 400\mu m \times 50\mu m$ size with the diameter of the bump-bond pad of about $10\mu m$. A corner of the pixel array together with a part of the multiple guard ring structure is shown in Figure 5.27a. The detector has also a so-called punch-through bias network, which consist of many connected with each other p^+ implantations. These implantations are situated close to the pixels and surround also the whole pixel array; this network helps to test the detector prior to the bonding to readout electronics. Principles of punch-through biasing and guard ring operation are explained in Chapter 2. A schematic cross section view of the detector and its bias scheme are shown in Figure 5.28.

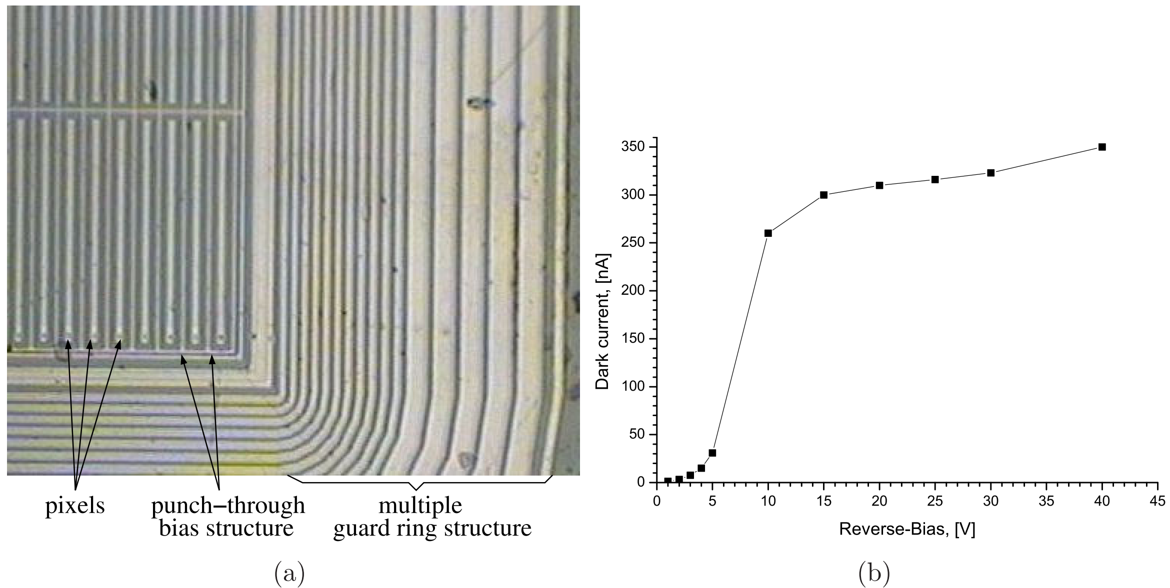

Figure 5.26: a) Microphotograph of a part of the detector b) Detector dark current as a function of applied bias

For the purpose of testing the detector was glued to a micro PCB board and then wire-bonded to provide the contact to bias connectors. The board was placed in a Faraday cage to protect the detector from electromagnetic fields and light.

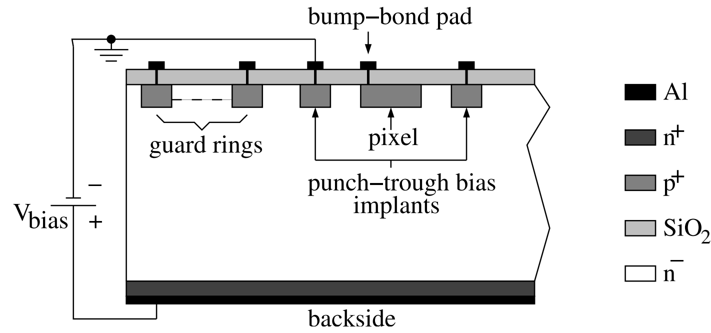

Figure 5.27: Schematic cross section view and bias scheme of the detector

The I-V characteristic of the detector, measured by biasing of the punch-through network, is shown in Figure 5.27b. It was found that the guard ring structure of the detector was damaged and could not be employed. Without biasing of the outer guard ring the dark current was unstable beyond 40V; therefore 35V bias was chosen for the operation. With that voltage applied between a single pixel and the backside the dark current of 220nA into the pixel was measured. Such a large current is caused by the lateral extension of depletion region. Therefore for tests with only a few bonded pixels the presence of a biased punch-through network is inevitable. In this case the punch-through network will accept the most part of the leakage current and only a small part(as under normal operation) will flow into the bonded pixels.

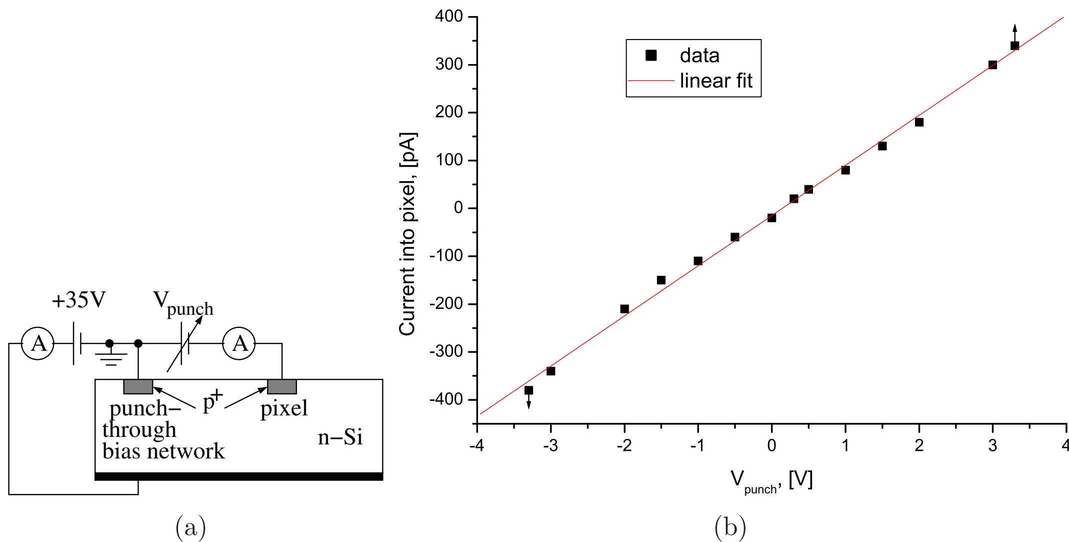

Figure 5.28: Test of the punch-through bias network a) Biasing scheme b) I-V characteristics

To test the punch-through bias network a fixed reverse bias was applied between the network and the detector backside; another variable voltage was applied between the network and a pixel and the current into the pixel was measured, as shown in Figure 5.29a.

The results of the measurement are shown in Figure 5.29b; beyond 3.3 V and below -3.3V the current rises exponentially, which is marked with the arrows. This corresponds to the onset of the punch-through(see section 2.2.4). From the linear fit the resistance of 9.5 $G\Omega$ was found, which shows a very good isolation between the pixels and the punch-trough network.

5.9 Test of the readout electronic with the detector

Generally, the electronic noise can be found by recording spectra of γ-ray sources. The broadening of photopeaks in the spectra is caused by both the electronic(ENC_e) and the statistical(ENC_s) noise components. For the total noise ,ENC_T, which can be obtained as a σ of the Gaussian fit of a photopeak, the following equations are valid:

$$ENC_T = \sqrt{ENC_e^2 + ENC_s^2} \quad (5.4)$$

$$ENC_T = \frac{FWHM}{2.35w} \quad (5.5)$$

where FWHM is Full Width on Half Maximum of the photopeak and w is a mean energy required to create one e^--hole pair. From these two equations and by using of equation 2.15 for the statistical noise, the electronic noise can be found as:

$$ENC_e = \sqrt{\left(\frac{FWHM}{2.35w}\right)^2 - \frac{F \cdot E_\gamma}{w}} \quad (5.6)$$

with the Fano factor $F = 0.12$ and $w = 3.63eV/e^-$[Ali80] for silicon.

To check noise performance under operation conditions and to calibrate the inject capacitor(see section 5.2) the readout electronic was wire-bonded to the test detector. Because of the difficulties with the wire-bonding only one pixel was bonded. The punch-through bias network was employed to keep the leakage current into this pixel small. For 3.6V VDDA, the punch-through bias voltage was set to 2.8V, which is approximately equal to the DC input voltage of the CSA. Thus the potential difference between the pixel and the punch-trough network is almost zero, which, according to Figure 5.28b, prevents the current flow between these structures.

The shaper bias, DAC6, was set to 50, which corresponds to about $0.75\mu s$ shaping time The discriminator threshold was set to about $1500e^-$. Linearity of the data acquisition circuitry was verified; it showed a linear response with up to $8000e^-$ input charge.

Two X-ray sources, ^{109}Cd and ^{55}Fe, were used for the noise test. The most important characteristic energies of these elements are given in Table 5.2. Errors in the number of generated electron-hole pairs are caused by statistical variations(Fano noise, section 2.2.6).

The recorded spectrum of the ^{109}Cd source is shown in Figure 5.30. Beside of two photopeaks corresponding to the Ag-K_α and Ag-K_β lines one can see also so-called *split events* corresponding to a partial detection of the energy deposited in neighbouring pixels.[9]

[9]Small peaks at around 550# and 820# correspond probably to X-ray fluorescent lines of Fe-K_α(6.4keV) and Au-L_β(11.5keV).

Source	Transition	Energy, [keV]	# of e-h pairs in Si
^{55}Fe	Mn K_α	5.895	1620 ± 14
^{55}Fe	Mn K_β	6.490	1783 ± 15
^{109}Cd	Ag K_α	22.103	6072 ± 28
^{109}Cd	Ag K_β	25.005	6870 ± 30

Table 5.2: X-rays from ^{55}Fe and ^{109}Cd sources

Split events cause also the larger broadening of the photopeaks towards lower energies, therefore only the right-hand side of the peaks was used for a Gaussian fit. From the positions of the Ag-K_α and Ag-K_β lines the channel-energy relation was found to be $E_\gamma = 17.4\frac{eV}{ADC\#}\cdot channel - 3424.2eV$. The FWHMs and positions of both peaks, obtained from the fits, together with the electronic noise, calculated by equation 5.6, are given in Table 5.3.

Energy, [eV]	22103	25005
peak position, ADC#	1469	1636
FWHM, [eV]	569 ± 2	597 ± 16
ENC_e, $[e^-]$	61	63.8

Table 5.3: Data from ^{109}Cd spectrum

The noise value is in agreement with that previously obtained from the measurement with the external shaper(see section 5.3). This noise value is not minimal because of the non-optimal shaping time, which unfortunately cannot be adjusted for too large signals from the ^{109}Cd source.

To test the electronic at longer shaping times a ^{55}Fe source was used; DAC6 was set to 5, which corresponds to the about $2\mu s$ shaping time. With the such a small shaper bias the discriminator threshold had to be set with the external resistor(see section 5.5).

The measured spectrum of the ^{55}Fe source is shown in Figure 5.31; evaluated from the fits data are given in Table 5.4. One can resolve Mn-K_α and Mn-K_β lines from the spectrum. The relation between channel and energy was found to be $E_\gamma = 13.13\frac{eV}{ADC\#}\cdot channel + 505.2eV$; the threshold was determined to be 2.8keV. As was expected, in agreement with the measurement shown in Figure 5.15, the lower noise was obtained.

Energy, [eV]	5895	6490
peak position, ADC#	410.5	455.8
FWHM, [eV]	434 ± 4	407 ± 17
ENC_e, $[e^-]$	48.9	45.4

Table 5.4: Data from ^{55}Fe spectrum

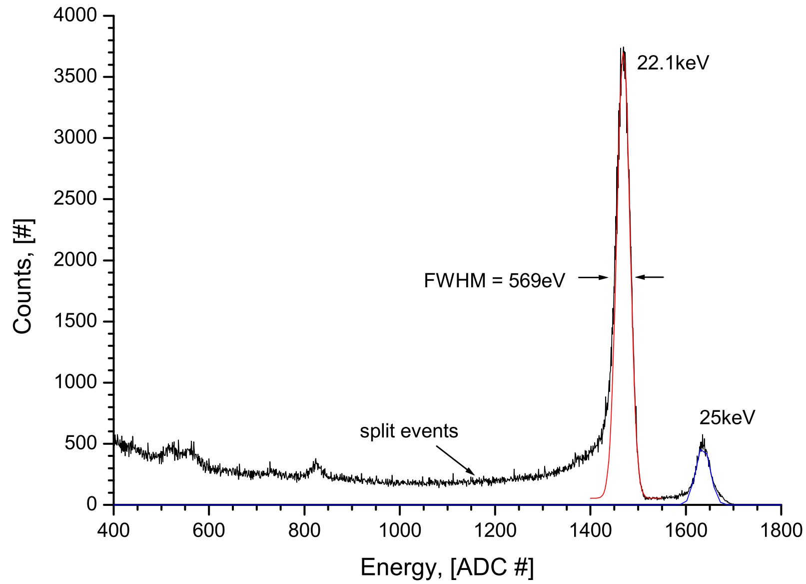

Figure 5.29: Energy spectrum of ^{109}Cd source

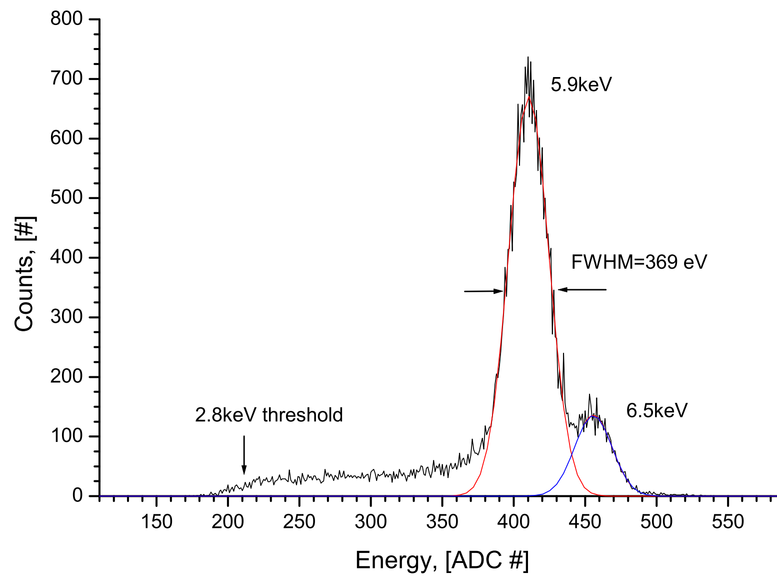

Figure 5.30: Energy spectrum of ^{55}Fe source

Chapter 6

Cesium Iodide detector

The cesium iodide detector was chosen as an absorber of scattered photons in the Compton camera prototype. The detector was developed for the MEGA experiment[Kan04] and adapted for our application by using of shorter crystals. It measures energy of photons and position of the interaction. The detector, shown in Figure 6.1, consists of an array of 10×12 CsI(Tl) crystals of $5 \times 5mm^2$ section which are optically isolated from each other with a reflective material(several layers of thin reflective paper). The crystal length of $15mm$ is more than sufficient, as was discussed in Chapter 3, to fully absorb photons of up to 150keV energy. Each crystal is optically coupled via transparent silicon to a Si PIN photodiode with the light sensitive area equal to the crystal section.

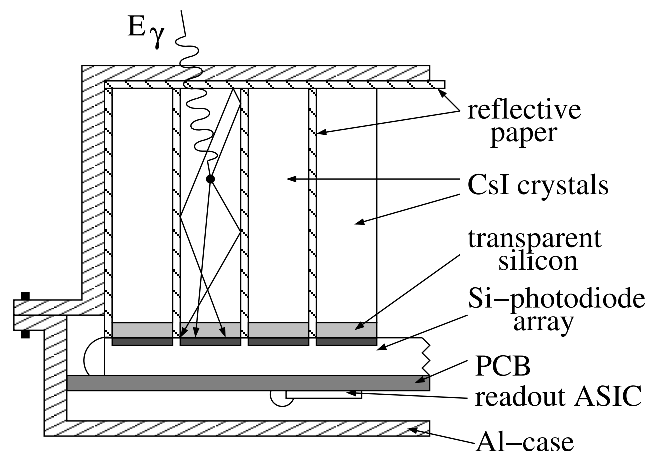

Figure 6.1: Side view of the cesium iodide detector

The photodiodes are integrated on a single wafer and form a 10×12 array with $0.7mm$ separation between single diodes. Each photodiode has its own pad at the edge of the wafer for the purpose of wire-bonding to a signal processing circuitry. The photodiode array is mounted on a PCB board, which houses also a TA1 readout chip[1] on the backside. The TA1 chip performs self-triggering serial multiplexed readout of the photodiode array. Each of its 128 channels has a charge sensitive preamplifier, a shaper, a sample and hold

[1] Product of Integrated Detector & Electronics AS, Oslo, Norway, www.ideas.no

circuit and a discriminator. Data acquisition cycle is organised by external, VME-bus based electronics and controlled by a custom-written program; these are described in detail in [And00] and [Sch02], respectively.

For the purpose of protection from light, moisture and electromagnetic distortions, the detector and the TA1 chip are placed in an aluminium box, which is $2mm$ thick on the crystal side and $1mm$ thick on the diode side. The photograph of 120 isolated CsI(Tl) crystals arranged into a 10×12 matrix together with the photodiode array covered with transparent silicon is shown in Figure 6.2. Both parts are screwed together to provide the pressure necessary for the good optical coupling.

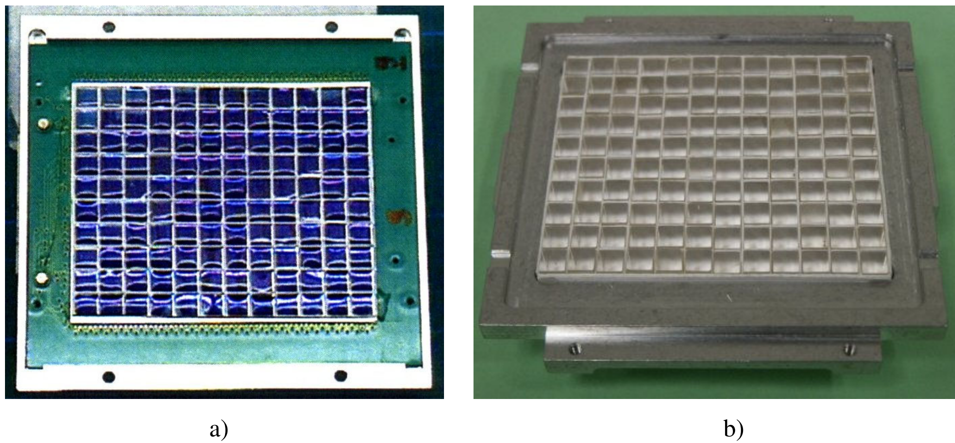

Figure 6.2: a) The photodiode array with the transparent silicon deposited on its surface(from [Sch02]) b) The array of 120 polished and isolated from each other CsI(Tl) crystals prepared for the optical coupling

In the following sections the performance of the detector relevant to the application in the Compton camera will be analysed and discussed.

6.1 Performance of the photodiode array

The total leakage current of the photodiode array was measured to be about 20nA at room temperature and 45V full depletion voltage after disconnecting broken diodes(3). This corresponds to about 171pA per pixel. The capacitance of each diode at full depletion is specified by the manufacturer[2] as 15pF. An additional input capacitance due to the stray capacitance of bonding wires and traces on the PCB was estimated to 5pF.

The noise performance of the TA1 chip is specified as $ENC_{base} + ENC_{slope} \cdot C_{inp}$, where C_{inp} is the external input capacitance seen by the preamplifier(detector capacitance plus strays). Since the TA1 chip employs a simple CRRC shaper, equation 4.26 can be used to determine the noise due to the detector leakage current. The total noise contribution of the electronics is given then by

[2]Hamamatsu Photonics, www.hamamatsu.com

$$ENC_e = \sqrt{(ENC_{base} + ENC_{slope} \cdot C_{inp})^2 + \frac{1.57e^2}{\pi q}\tau_0 I_{leak}} \quad (6.1)$$

For $2\mu s$ shaping time the typical values for ENC_{base} and ENC_{slope} are given by the manufacturer as $165e^-$ and $6.1e^-/pF$ respectively. This results in $294e^-$ total noise contribution of the electronics.

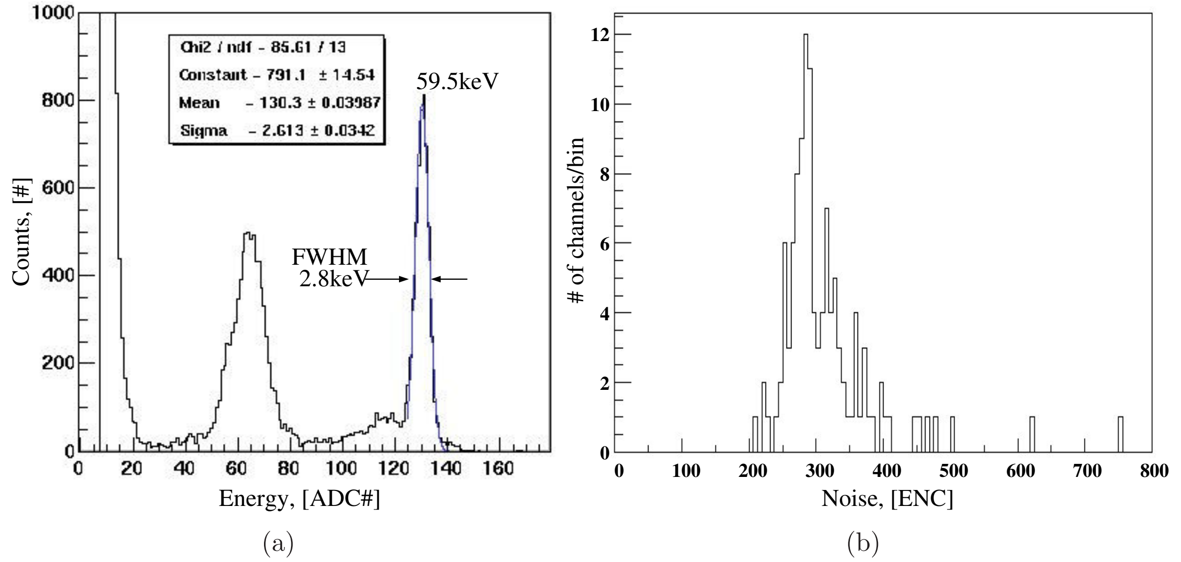

Figure 6.3: a) Energy spectrum of ^{241}Am source in a single channel b) Histogram of noise performance of the Si-photodiode array connected to the TA1 chip

The noise performance of the Si-photodiode array connected to the readout electronics was checked by illuminating the CsI detector from the diode side with an ^{241}Am source. The most important energies of γ's emitted by the source together with the number of e^--hole pairs created in silicon at full energy absorption are given in Table 6.1. The peak position of the americium's 59.6keV full absorption line and zero point are used for the calibration of each channel by the program.

Transition	Energy, [keV]	Intensity, [%]	# of e^--hole pairs in Si
Np L_α	13.9	10.7	3829 ± 21
Np L_β	17.5	12.0	4821 ± 24
Np L_γ	21.0	3.0	5785 ± 26
α-decay	26.3	2.4	7245 ± 29
α-decay	59.5	35.9	16391 ± 44

Table 6.1: γ's from ^{241}Am source

Gamma quanta coming form the source pass through a $1mm$ thick aluminium box and a $1.5mm$ thick PCB board into the photodiode matrix, where they can be directly

converted into electron-hole pairs. The typical spectrum recorded in a single photodiode is shown in Figure 6.3a. The photopeak at 59.5keV is clearly seen; L_α, L_β and L_γ transition lines of neptunium cannot be resolved. The noise calculated from such a spectrum for each channel is shown as a histogram in Figure 6.3b with the mean value of $302e^-$. Subtracting quadratically the statistical noise, which is only $44e^-$, the noise contribution of the electronics of $299e^-$ is obtained. This value is in the good agreement with the value calculated above($294e^-$).

6.2 Performance of the trigger circuitry

For the purpose of the self-triggering readout each channel of the TA1 chip possess a discriminator. The threshold voltage is set by an external DAC and common to all channels. There is no possibility of individual threshold adjustment. The outputs of the discriminators are wire-or'ed together to form a main trigger signal, which initiates a data acquisition cycle. Each individual discriminator output can be masked by the program. Since a threshold adjustment is missing this possibility is useful if low thresholds have to be set. It is interesting in our application because low energy scattered photons have to be detected.

To see which channels have to be masked, the trigger rate of each single channel was measured as a function of threshold voltage. The results are shown in Figure 6.4a; the number of channels that have to be masked to keep the total trigger rate below 100Hz as a function of threshold voltage is given in Figure 6.4b. A threshold of 2200 was chosen to test as many pixels as possible; it corresponds to about $1900e^-$.

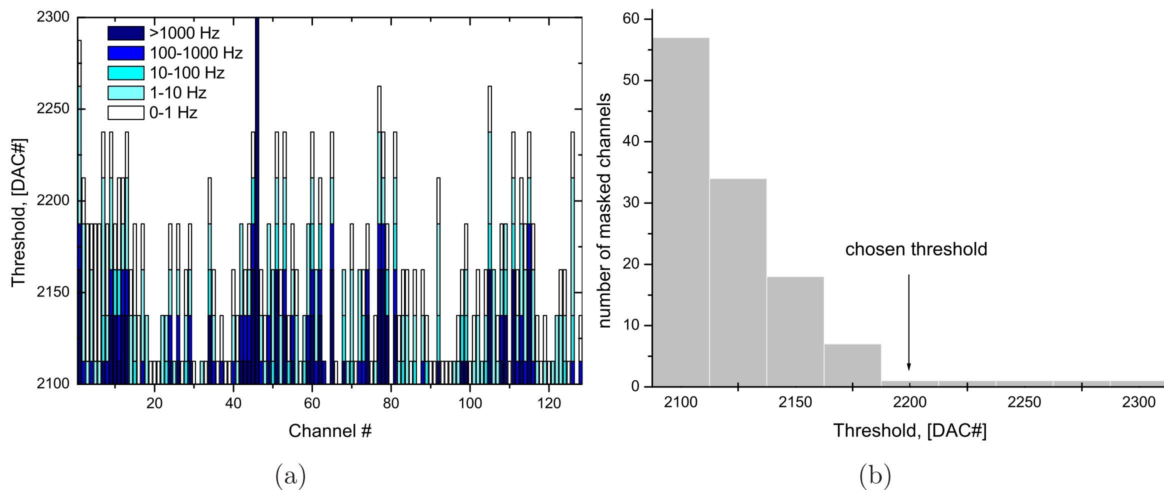

(a) (b)

Figure 6.4: a) Trigger rate for individual channels as a function of threshold b) Number of channels that have be masked to keep the total trigger rate below 100Hz as a function of threshold

6.3 Performance of the cesium iodide detector

6.3.1 Light collection

As can be seen from Figure 2.7 in Chapter 2, in the energy range of up to 500keV the energy loss of photons in CsI is dominated by the photoeffect. Since the range of 150keV electrons in CsI is about $200\mu m$, the position of the interaction can be almost considered as a point. The resulting scintillation light is reflected from the crystal wrapping until it is collected onto the photodiode. It was found by Bird et al.[Bir93] that the combination of fine polished crystals with good reflective wrapping gives the best light output. In our case all six crystals sides were polished; four sides were left as supplied by manufacturer[3] and the two other sides - facing the photodiode and its opposite - were manually polished with a $1\mu m$ AlO_2 powder.[4] The reflective property of the wrapping material was analysed by Andritschke[And00], who measured the light output as a function of the material thickness and found out the optimum.

The coupling medium between CsI(Tl) and the photodiode has to be properly chosen to avoid reflections on the boundaries between materials. The reflectance coefficient R and the transmittance coefficient T for the light incidence normal(perpendicular) to the plane boundary between the two dielectric media with refractive indexes n_1 and n_2 are given by the Fresnel formulas[Woa00]:

$$R = \frac{(n_1 - n_2)^2}{(n_1 + n_2)^2} \qquad T = 1 - R = \frac{4n_1 n_2}{(n_1 + n_2)^2} \tag{6.2}$$

Since the light crosses subsequently two boundaries, the total transmittance coefficient is the product of the two single transmittance coefficients:

$$T = \frac{16 n_1 n_2^2 n_3}{(n_1 + n_2)^2 (n_2 + n_3)^2} \tag{6.3}$$

By taking the derivative of equation 6.3 with respect to n_2 and equating it to zero the optimal refractive index of the coupler can be found: $n_{2,opt} = \sqrt{n_1 n_3}$. With the refractive index of CsI(Tl) at light wavelength of 550nm[5] $n_1 = 1.8$ and that of the SiO_2 entrance window of the photodiode $n_3 = 1.46$ the optimum coupling medium would have the refractive index of 1.62. Because of its elastomeric properties transparent silicon[6] was used, which has the refractive index of 1.41. Inserting this value into equation 6.3 results in a 0.985 transmittance coefficient for the scintillation light.

In the photodiode the scintillation light is transformed to electron-hole pairs. The effectiveness of this process is specified by the quantum efficiency of the photodiode, which is about 65% in the range around the maximum of CsI(Tl) emission spectrum. Therefore from 65 photons per one keV of the photon energy(from Table 2.2) one expects $65 \cdot 0.985 \cdot 0.65 = 42e^-$ signal in the photodiode.

[3] Hilger Analytical Limited, www.hilger-crystals.co.uk

[4] Ten crystals were additionally polished with a special de-agglomerated $0.05\mu m$ AlO_2 powder and arranged together on the same edge of the crystal matrix, but later measurements did not show any noticeable increase in the light output from these crystals.

[5] corresponds to the maximum of the CsI(Tl) emission spectrum

[6] RTV615 type from GE Silicones

Another important issue that has to be taken into account is the decay time of CsI(Tl) scintillator, which is relative large, $0.8\mu s$. Since the preamplifier of the TA1 chip employs continuous reset mechanism, similar to that described in section 4.2.3, large reset constants have to be chosen to provide integration of the signal charge without losses. The shaper constant has also to be adjusted correspondingly: it has to be much larger than the decay time of the scintillator(the charge collection time of the Si PIN photodiodes is much faster). The dependence of the light output on the shaping time was measured by Andritschke[And00] and is shown in Figure 6.5. A 20mm long crystal of $5 \times 5mm^2$ section coupled to a single photodiode, similar to that of in the Si PIN photodiode array, was used for the test. Light output was calculated by comparing the spectrum of the ^{137}Cs source[7] with the spectrum of ^{241}Am source, taken directly in the photodiode.

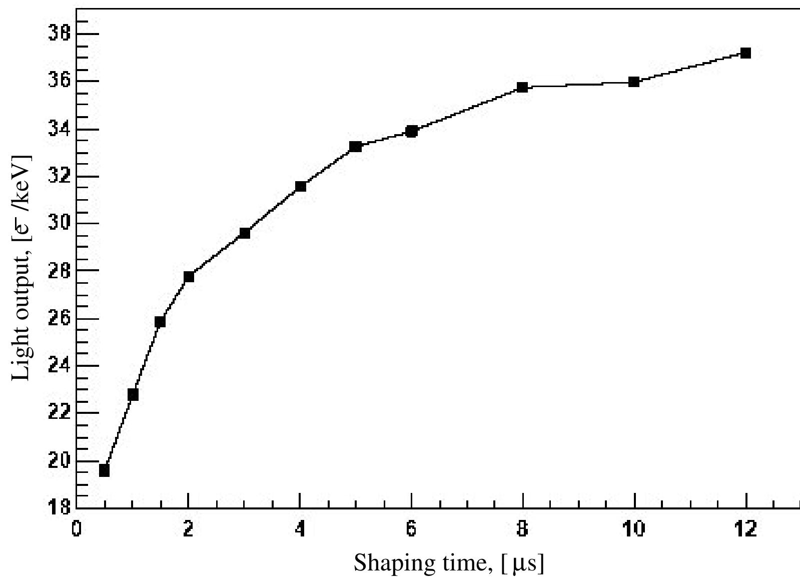

Figure 6.5: Light output as a function of shaping time(from And[00])

As can be seen from Figure 6.5 the output signal is still rising even at $12\mu s$ shaping time and the light output value of $42e^-$, calculated above, is not reached. The reason is probably the light absorption in the wrapping material. Since the maximum shaping time set by the TA1 chip is only $3\mu s$, about 25% of the signal is lost. The distribution of the light output in the CsI detector, measured as in the previous case by comparison of the spectra from the ^{241}Am and ^{137}Cs sources, is shown in Figure 6.6a as a function of the position in the crystal matrix and in Figure 6.6b as a histogram. The mean value of the light output is obtained to be about $20e^-$/keV.

6.3.2 Energy resolution

To analyse the energy resolution of the CsI detector the spectra of ^{137}Cs and ^{57}Co sources were taken. The most important energies of γ's emitted by the sources together with the

[7]Radioactive ^{137}Cs source emits photons of 661.7keV energy

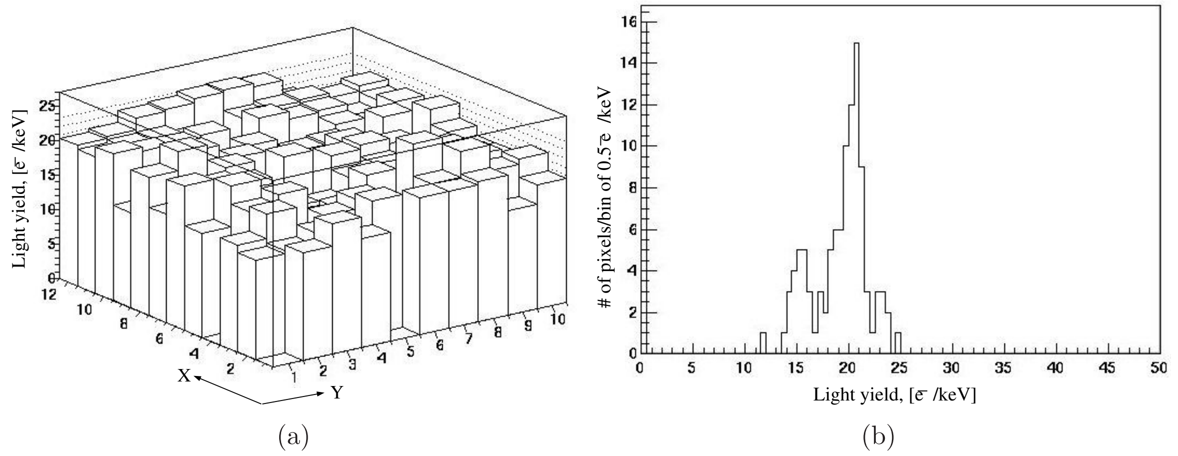

Figure 6.6: a) Distribution of light output as a function of the position in the crystal matrix b) Histogram of the distribution

expected signal at full energy absorption, calculated with the assumption of $20e^-$/keV, are given in Table 6.2. The calibration is performed by the program which uses peak positions of the 662keV full absorption line of ^{137}Cs and zero point and based on the linearity of the signal processing electronics.

Source	Transition	Energy, [keV]	Intensity, [%]	Expected signal, $[e^-]$
^{57}Co	e^--capture	14.4	9.2	288 ± 17
^{57}Co	e^--capture	122.1	85.6	2442 ± 49
^{57}Co	e^--capture	136.5	10.7	2730 ± 52
^{137}Cs	β^--decay	661.7	85.1	13234 ± 115

Table 6.2: γ's from ^{57}Co and ^{137}Cs sources and expected signal in a photodiode

The spectrum of ^{137}Cs is shown in Figure 6.7a as a sum of energy spectra in single channels. Every hit is considered as an event if its value is four times above the baseline noise(4σ cut). Since the mean free path(reciprocal value of the total linear absorption coefficient from Figure 2.7a) for a photon of 662keV energy is about 3cm in CsI it can happen that the photon will be absorbed in several crystals. In this case the summed value of energy suffers from a higher noise, since each item is measured with an error. Therefore only single events, which are the largest fraction of the total, were selected for the resolution analysis. The resolution Δ, defined as the ratio of FWHM of photopeak to its position, is given by a histogram in Figure 6.7b; it has a mean value of 11.6% FWHM. The resolution can be estimated by using the following formulas:

$$\Delta = \frac{FWHM}{E_\gamma} = \frac{2.35\sigma}{E_\gamma} = \frac{2.35\sqrt{\sigma_e^2 + \sigma_s^2}}{E_\gamma} = \frac{2.35\sqrt{ENC_e^2 + ENC_s^2}}{N_{e-h}} \tag{6.4}$$

where σ is a standard deviation of a Gaussian, ENC_e and ENC_s are electronical and statistical parts of the total noise, respectively , and N_{e-h} - is the number of e^--hole pairs

generated by photons with energy E_γ. Taking the statistical value as $ENC_s = \sqrt{N_{e-h}}$ and using the ENC_e value from section 6.1, the resolution was estimated to be 5.7% FWHM. The discrepancy can be caused by the inhomogeneity in generation, propagation and collection of light in the CsI(Tl) crystals, a known problem, which was experienced also by others[Gru98]. Insufficient optical coupling between crystal and diode, non-uniformity in the doping of CsI with thallium can be also the reasons.

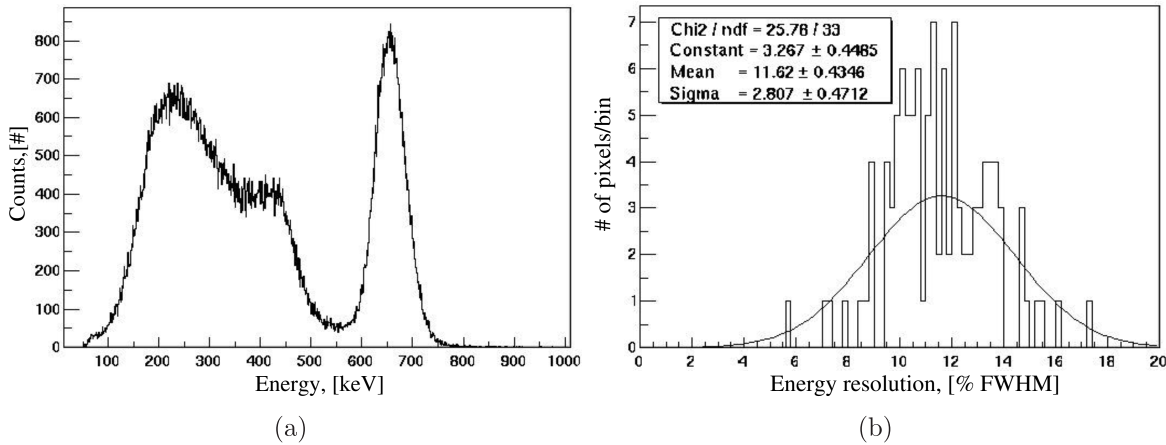

Figure 6.7: a) Energy spectrum of the ^{137}Cs source with only single events from all channels summed b) Histogram of energy resolution of CsI detector for 662keV energy

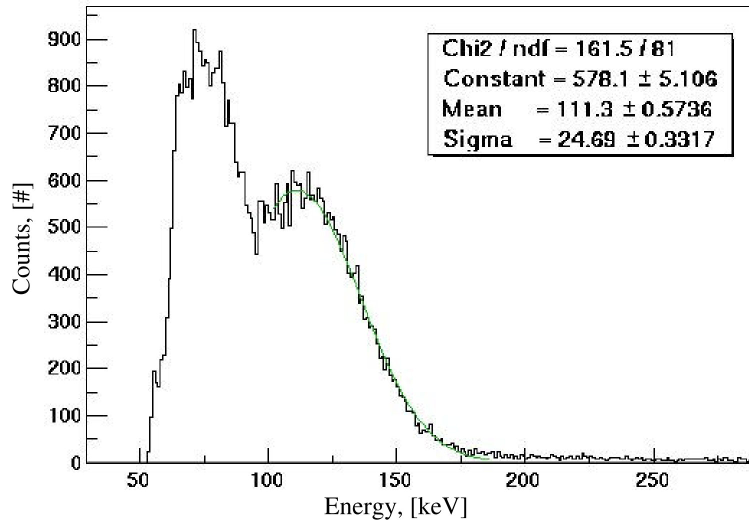

Figure 6.8: Energy spectrum of the ^{57}Co source with only single events from all channels summed

The resolution was also checked at lower energies. For that purpose the threshold was set down to 2100, channels with a high trigger rate were masked according to Figure 6.4 and spectrum of ^{57}Co was taken. As in the previous case only single events are selected

and shown in Figure 6.8. It can be seen that the 122keV photoabsorption peak is located on the baseline noise, therefore only the right part of the peak can be used for a Gaussian fit. The obtained mean value of the peak is slightly different because the calibration is not precise enough at low energies. The energy resolution, calculated from the spectrum is about 50% FWHM at 122keV energy(the best resolution obtained in a single channel was 39% FWHM). According to equation 6.4 one would expect 29% FWHM, the discrepancy can be explained with the similar arguments as in the case with ^{137}Cs.

Such a poor resolution together with the range of measured energies in the close proximity to the baseline noise can lead to the large number of incorrect coincidences between Compton- and photodetectors. This will make more complicated reconstruction of the position of γ-sources. Another drawback is that since the threshold has to be set low, only a part of pixels can be used because of the high trigger rate at low thresholds. Therefore the application of the CsI detector as a photoabsorber in the Compton camera prototype is strongly limited.

Chapter 7

Summary and Outlook

7.1 Summary

In this thesis a possible application of existing semiconductor pixel detectors from HEP[1] and a scintillation detector from astrophysics in a medical application - a Compton camera was investigated. The Compton camera is supposed to replace currently used Anger cameras in nuclear medicine because of its better sensitivity, which will allow to give a lower radiation dose to a patient. Two position-sensitive detectors working in coincidence are required to build a Compton camera prototype: one to measure the energy of Compton recoil electrons and the other to fully absorb scattered photons.

Silicon suits best as a scatter detector material since scattered photons have a high probability to leave the detector after a single Compton interaction. Due to the low leakage current of silicon detectors a very good energy resolution can be achieved even at room temperature. With a fine pixellated structure the detectors exhibit also a good position resolution, which is of crucial importance for imaging. Silicon pixel detectors have been used in HEP experiments over the years so their production technology is very advanced and very good quality and relatively chip detectors can be fabricated.

The application of pixel detectors in a Compton camera imposes other than in HEP demands on the readout electronic. The electronic have to be self-triggered, low noise, low power but operate at low rates. Also it has to deliver a timestamp for use in coincidences. To achieve low noise operation the electronic has to be tailored to the detector, therefore the detector properties were analysed first. Then a detailed theoretical noise analysis was carried out. Based on these calculations an analog multichannel readout was developed. One readout channel consists of a charge sensitive amplifier, a CRRC shaper, a peak detector, a discriminator, a time-to-voltage converter and an analog output buffer. A sparse scan readout scheme, which reads only pixels with hits, was realised. The mixed-signal readout chip RAMSES was implemented in the AMS $0.6\mu m$ CMOS technology and fabricated in a multi-project wafer run through Europractice IC Service[2]. The readout cycle and the data transfer to a PC were organised with a XILINX FPGA. The software for data acquisition, having a graphical user interface, was written in Borland C++.

[1] High Energy Physics

[2] www.europractice.imec.be

To verify noise performance, the readout electronic was wire-bonded to a Si-pixeldetector and spectra of γ-ray sources were recorded. From the spectrum of a ^{55}Fe source an electronic noise of about $49e^-$ was obtained at room temperature. It proves that readout electronic is adequate for using with a scatter detector in the Compton camera prototype.

As a full energy absorber dense materials with a high atomic number have to be used. From semiconductors only CdTe detectors can be considered, but they are too expensive. Since the energy resolution of the second detector is not very important, scintillator detectors can be a good alternative. An existing scintillation detector from MEGA experiment, consisting of an array of 10×12 CsI(Tl) crystals of $5mm \times 5mm$ section and read out with a Si PIN photodiode matrix, was adapted to smaller energies by using of shorter crystals($15mm$). The detector performance was verified and the energy resolution at 122keV was found to be about 50% at room temperature. This resolution is quite poor, which can lead to many noisy coincidences, making difficult the image reconstruction of a γ-source.

7.2 Outlook

First of all the readout electronic has to be bump-bonded to an appropriate Si-pixeldetector, with a good pixel isolation and a low leakage current. Due to the application of a bump-bonding technique a lower electronic noise is expected, since smaller than caused by wire-bonding stray capacitance will be added to the CSA input. Also this technique do not cause any physical damage to the pad.

Then a Compton camera prototype has to be assembled, providing the hardware coincidence[3] between the Si-pixeldetector and the CsI detector. To test the camera strong γ-ray sources[4] are required since only about 1% of photons will undergo a Compton scattering in the first detector. Therefore the facilities for radiation protection have to be provided. Another way to increase statistics can be a combination of several detector modules to enlarge the sensitive area of the first detector. Also the mechanics, which can change and fix the position of the detectors, relative to each other and to a γ-ray source, has to be developed.

With the prototype build and coincidence events taken, different image reconstruction algorithms, which are reviewed and compared e.g. in [Leb99, Tom02], can be tested; the position resolution of the Compton camera prototype can be determined.

Further improvements in the readout electronic can be achieved by the decoupling of the power supply for the CSA's from the global analog power supply.Also the threshold adjustment circuit can be corrected and improved, for example, by making the threshold adjustment independent of the shaper bias and also by employing the analog threshold adjustment mechanism[Lin01].

For even better energy resolution other detectors, such as for example a DEPFET[5] pixel detector, can be examined as a scatter detector. The DEPFET detector[Kem87,

[3] Since the developed readout electronic delivers also a timestamp a software coincidence can be an option

[4] A ^{57}Co radioactive source is suitable for the test since it emits photons of 122keV, which is close to the ^{99m}Tc energy of 140keV

[5] DEPleted Field Effect Transistor

Lut99] is a detector structure with integrated amplifying mechanism. A multichannel readout for the DEPFET pixeldetector is under development in our group[Win04].

The CsI detector, conceived actually for operation in the higher energy range, leaves many possibilities for improvement. Smaller section of the crystals and photodiodes will besides of the better position resolution lead to a smaller leakage current of the photodiodes. This will allow to operate with longer shaping times, which is important for light collection, without having larger noise. Smaller area of the photodiodes will also result in the smaller detector capacitance, which will also reduce the noise. Instead of the TA1 chip a new low noise readout ASIC, capable to set long shaping times and with a threshold adjustment circuitry has to be developed. With all these changes a better energy resolution and lower thresholds are possible. The improvement of the CsI detector performance can be encouraged by the works of Gruber et al.[Gru98] and Patt et. all[Pat98], who have obtained the energy resolution as good as 10.7% at 140keV energy and room temperature.

Originally the readout electronic was developed for a Compton camera but it also can be applied in other applications, where two-dimensional X-ray imaging with a very good energy resolution is required, i.e. radiography, autoradiography, protein crystallography, X-ray astronomy.

Appendix A

Noise in electronic devices

By definition, noise is any unwanted disturbance that interferes with a signal of interest. Disturbances may result for example from electromagnetic coupling of signals from neighbouring circuits, from mechanical vibrations of circuit components. These are all examples of external noise sources. Their effect can be minimised by shielding, filtering, changing the layout of circuit components. But a certain noise level will be always present due to intrinsic or fundamental noise sources. To the most important fundamental noise sources belong thermal noise, flicker noise and shot noise, which will be described now in detail.

A.1 Thermal noise

Thermal or Johnson noise arises because of the random motion of electrons due to thermal effects in a resistor. When a resistor is in the equilibrium with a surrounding medium the potential drop across its terminals is zero. Due to the thermal motion, however, fluctuations in the potential drop occur. These fluctuations can be expressed as a mean square value of the noise voltage $\overline{v_{n,th}^2}$ or the noise current $\overline{i_{n,th}^2}$, given by

$$\overline{v_{n,th}^2} = 4kTR\Delta f \qquad \overline{i_{n,th}^2} = \frac{4kT}{R}\Delta f \tag{A.1}$$

where Δf is the frequency bandwidth, k is Boltzmann's constant and R is the resistor or the equivalent resistance of medium where the thermal noise occurring. Since thermal noise is independent of the frequency it is also referred to as *white* noise.

A.2 Flicker noise

Flicker noise, referred to also as 1/f noise, which reflects its dependence on frequency, is seen in most electronic devices. This noise is associated with carrier traps in semiconductors, which capture and release carriers in a random fashion. Flicker noise is always connected with a direct current, flowing through a device; the mean-squared value of the noise current can be expressed as[Gra94]:

$$\overline{i^2_{n,1/f}} = K_1 \frac{I^a}{f^b} \Delta f \tag{A.2}$$

where $b \approx 1$, a is a constant in the range from 0.5 to 2, I is a direct current, K_1 is a constant for a particular device, Δf is a small bandwidth at frequency f. In the simulations with Cadence the SPICE2 model of the flicker noise is used with

$$\overline{i^2_{n,1/f}} = \frac{K_{fs} I^{AF}}{C_{ox} L^2 f^{EF}}, \text{ or } \overline{v^2_{n,1/f}} = \frac{\overline{i^2_{n,1/f}}}{g_m^2} = \frac{K_{fs} I^{AF-1}}{C_{ox} L^2 f^{EF}} \tag{A.3}$$

As an example, for the AMS 0.6μm CMOS technology AF=1.72, EF=1, K_{fs}=1.126·10^{-26}.

A.3 Shot noise

Shot noise is associated with a direct current flow across a device and is a direct consequence of the discrete nature of the electric charge. Consider a simple forward-biased p-n diode. Electrons and holes, with a charge q each, cross the potential barrier and arrive at anode and cathode, respectively, resulting in a current pulse. Their passage through the barrier is purely random in nature, and the current I_D becomes the sum of independent, random current pulses. This leads to the fluctuations of the current referred to as shot noise[Lu99]:

$$\overline{i^2_{n,shot}} = 2qI_D \Delta f \tag{A.4}$$

A.4 MOSFET noise model

Small-signal model of a MOSFET with associated noise sources is shown in Figure A.1. Three noise sources are added: the noise sources $i_{d,th}$ and $i_{d,1/f}$, which represents thermal and flicker noise associated with the resistive channel, and the noise source i_g related to the shot noise generated by the gate leakage current I_g.

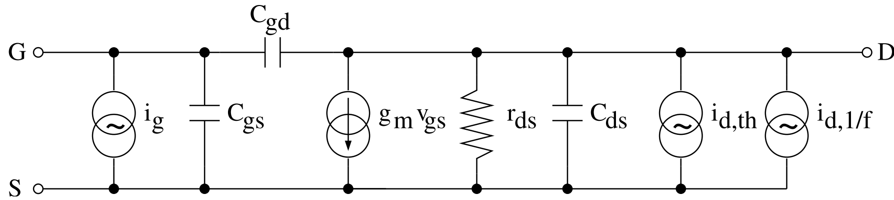

Figure A.1: Noise sources in a MOSFET

The last component is given by

$$\overline{i_g^2} = 2qI_g df \tag{A.5}$$

Since the gate current, flowing through the oxide, is very small, this component is usually negligible. Assuming the transistor operating in the saturation region, its noise associated

with the channel resistance can be approximated as[Cha97]:

$$\overline{i_{d,th}^2} = 4kT\gamma g_m df \quad \text{(A.6)}$$

where g_m is the transconductance of the FET and γ is a parameter, which depends on the oxide thickness and substrate doping. For modern CMOS processes $0.67 < \gamma < 1$. The flicker noise component is given by[Cha97]

$$\overline{i_{d,1/f}^2} = \frac{K_F I_{ds}}{C_{ox} L^2 f} df \quad \text{(A.7)}$$

where K_F is a constant, C_{ox} is the gate oxide capacitance per unit area, L - length of the transistor and I_{ds}- the current flowing through the transistor.

Appendix B

Layout of the RAMSES chip

The layout of a single pixel is shown in Figure B.1. The pixel cell has a size of $200\mu m \times 200\mu m$.

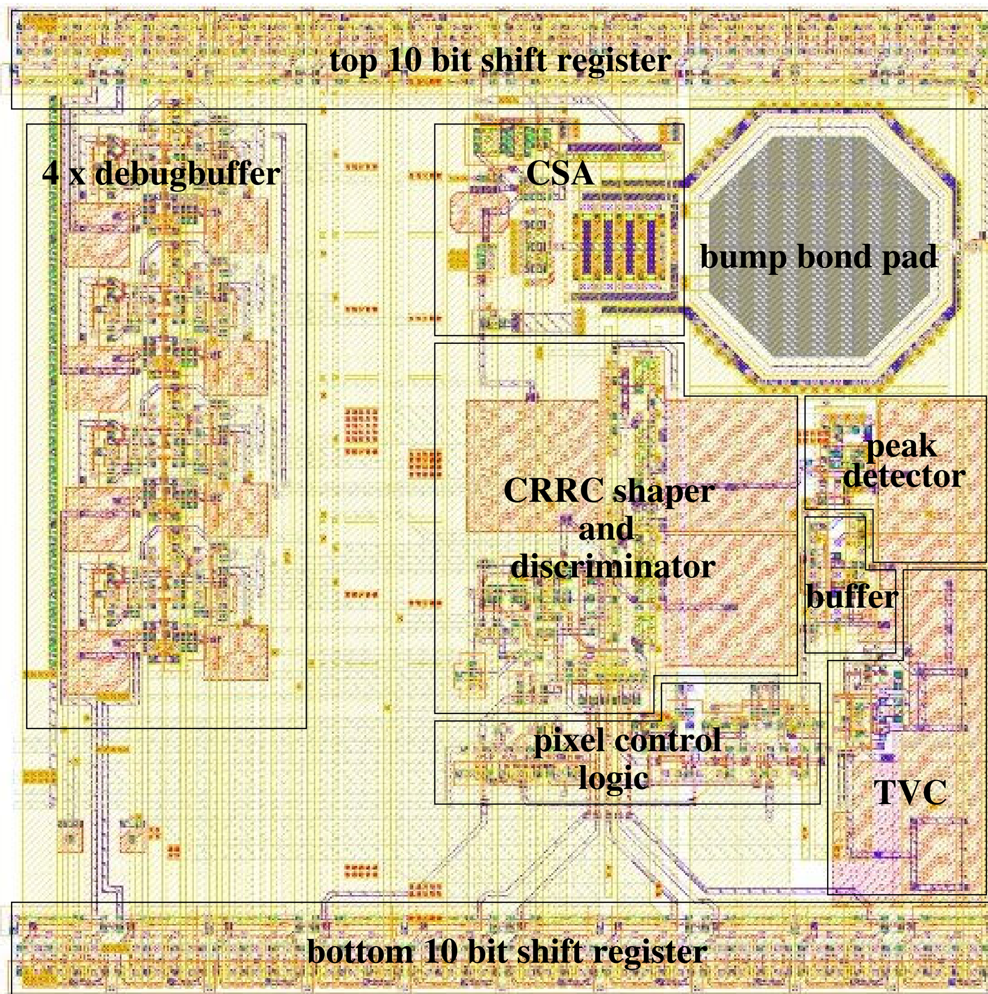

Figure B.1: Layout of a pixel cell

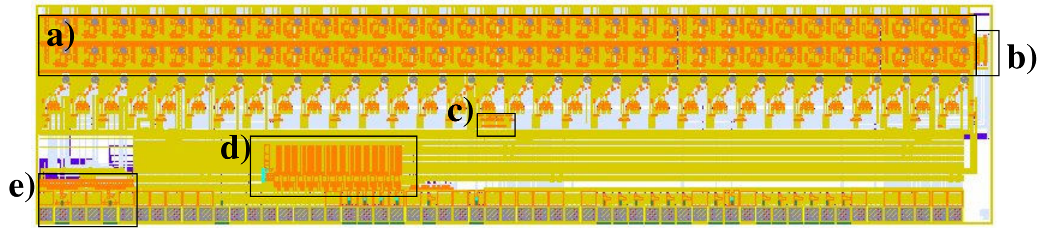

Figure B.2: Layout of the RAMSES chip

The layout of the whole RAMSES chip is shown in Figure B.2. It has a size of $6600\mu m \times 1515\mu m$. The following chip components are highlighted:

a) 2×32 array of single pixels

b) End-of-row(EOR) logic

c) End-of-column(EOC) logic

d) 16 digital to analog converters

e) two multiplexers with analog output buffers

Appendix C

Typical settings of the RAMSES chip

Table C.1: Typical settings of the RAMSES chip

Group	Name	value	unit	current in pixel, [μA]	Function
General	VDDA	3	V	-	analog power supply voltage
	VDDABUF	3	V	-	supply voltage for analog buffers
	VDDD	1.6	V	-	digital power supply voltage
CSA	Vfeed	1.25	V	-	bias voltage of the feedback transistor
	DAC5	50	#	0.48	bias of the source follower
	DAC9	100	#	0.96	active load, bias of the regulated cascode
	DAC10	223	#	35	bias of the input transistor
Shaper	DAC6	50	#	0.11	set of shaping time constant
Peak detector	DAC3	200	#	7.7	bias for peak detector
Discriminator	DAC7	200	#	0	set of threshold
	DAC8	200	#	0.96	bias of discriminator
TVC	DAC0	50	#	1.9	bias of the source follower
	DAC1	50	#	0.5	charge current
Debug buffer	DAC2	250	#	2.4	bias current for debug buffer and pixel buffer
Analog output buffer	DAC11	50	#	-	bias current for EOC and output analog buffers
	DAC12	50	#	-	bias current for EOC and output analog buffers

hitcol/row bias	DAC13	50	#	-	bias current for wired-OR of hitcol/row
hitbus bias	DAC14	20	#	-	bias current for wired-OR of hitbus

Appendix D

Software for data acquisition and test

A custom software has been developed for test of the RAMSES chip, data acquisition and to the some extent also for data analysis. It is written in Borland C++ to employ all the advantages of a graphical user interface. The following functions are performed by the software:

1. Programming of the shift registers of the RAMSES chip which include:
   (a) set of bias currents for the chip circuits
   (b) selection of a bias current to monitor or to source externally
   (c) selection of a pixel for readout debugging
   (d) selection of analog signals for output
   (e) change of individual pixel settings
2. Load of the FPGA configuration via serial interface
3. Set of delays and flags in the FPGA, used for various tests
4. Communication with measuring instruments via GPIB interface
5. Monitoring of measured results
6. Coordination of operations listed above to perform complex tests, e.g. threshold scan, linearity scan

A screenshot of the software, displaying results of the threshold scan(see section 5.5), is shown in Figure D.1.

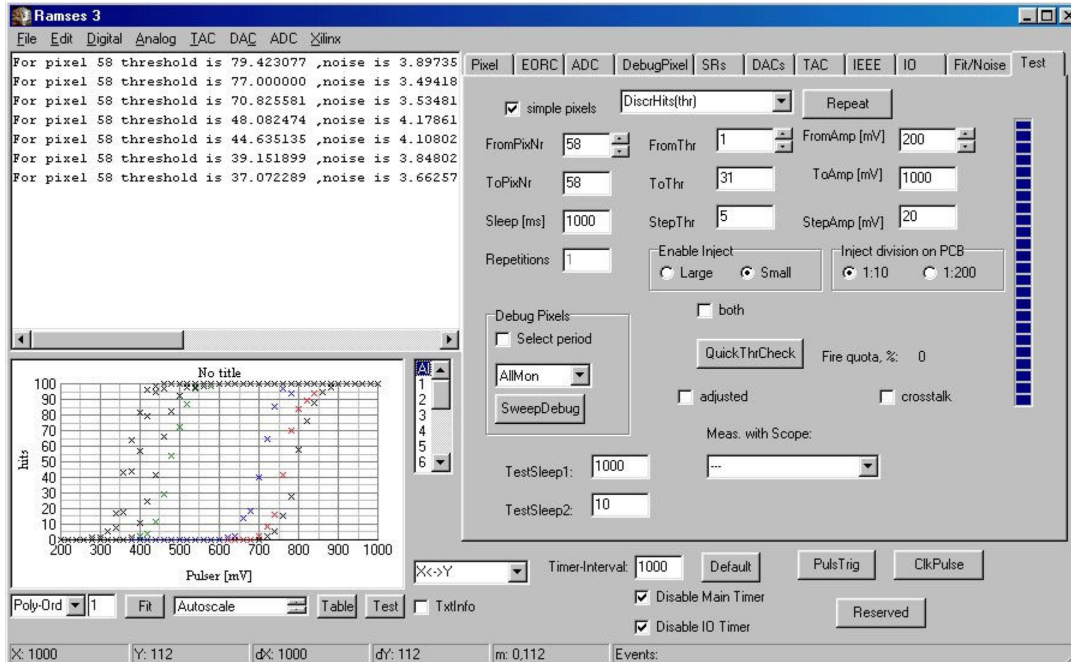

Figure D.1: Screenshot of the custom software

Bibliography

[Ali80] R.C. Alig, S. Bloom, C.W. Struck, *Scattering by ionization and phonon emission in semiconductors*, Phys. Rev. B, vol. 22, no. 12, pp. 5565-5582, 1980.

[All02] P.E. Allen, D.R. Holberg, *CMOS Analog Circuit Design*, 2nd ed., Oxford Univ. Press, 2002.

[And00] R. Andritschke, *Aufbau und Eichung der Kalorimeter fuer das Gammateleskop MEGA*, Diploma Thesis, TU Muenchen, 2000.

[Ang58] H.O. Anger, *Scintillation camera*, Rev. Sci. Instrum. 29, pp. 27-33, 1958.

[ATL99] ATLAS collaboration, *Detector and Physics Performance Technical Design Report 14,15* CERN/LHCC/99-14 and CERN/LHCC/97-15, Geneva, 1999.

[Bac98] R.J. Backer, H.W. Li and D.E. Boyce, *CMOS Circuit Design, Layout and Simulation*, IEEE Press, 1998.

[Bis93] A. Bischoff et al., *Breakdown protection and long-term stabilisation for Si-detectors*, Nucl. Instr. and Meth. A 326, pp. 27-37, 1993.

[Bla97] L. Blanquart et al., *Pixel analog cells prototypes for ATLAS in DMILL technology*, Nucl. Instr. and Meth. A 395, pp. 313-317, 1997.

[Cha97] Z.Y. Cahng, W.M.C. Sansen, *Low-Noise Wide-Band amplifiers in Bipolar and CMOS Technologies*, 2nd ed., Kluwer, 1997.

[Fis99] P. Fisher et al., *MEPHISTO - a 128-channel front end chip with real time data sparsification and multi-hit capability*, Nucl. Instr. and Meth. A 431, pp. 134-140, 1999.

[Gat88] E. Gatti, P.F. Manfredi, *Processing the signals from solid-state detectors in elementary-particle physics*, Rivista Del Nuovo Cimento, vol. 9, N. 1, 1986.

[Gra94] P.R. Gray, R.G. Meyer, *Analysis and design of analog integrated circuits*, 2nd ed., John Wiley & Sons, 1984.

[Gru96] C. Grupen, *Particle Detectors*, Cambridge University Press, 1996.

[Gru98] G.J. Gruber et al., *A Discrete Scintillation Camera Module Using Silicon Photodiode Readout of CsI(Tl) Crystals for Breast Cancer Imaging*, IEEE Trans. Nucl. Sci., vol. 45, no. 3, pp. 1063-1067, 1998.

[Ibr00] I. Ibragimov, *Development of a time measurement circuit for a pixel detector in CMOS technology*, Diploma Thesis, University of Siegen, 2000.

[Hau02] J. Hausmann, *Development of a low noise integrated readout electronic for pixel detectors in CMOS technology for a Compton camera*, Ph.D. Dissertation, University of Siegen, 2002.

[Hue01] F. Hügging, *Der ATLAS Pixelsensor*, Ph.D. Dissertation, University of Dortmund, 2001.

[Kan04] G. Kanbach et al., *The MEGA project*, New Astronomy Reviews, vol. 48, no. 1, pp. 275-280, 2004.

[Kem87] J. Kemmer and G. Lutz, *New detector concepts*, Nucl. Instr. and Meth. A 253, pp. 365-377, 1987.

[Kit96] C. Kittel, *Introduction to solid state physics*, 7th ed., John Wiley & Sons, 1996.

[Kno79] G.F. Knoll, *Radiation Detection and Measurement*, John Wiley & Sons, 1979.

[Lak94] K.R. Laker, W.M.C. Sansen, *Design of Analog Integrated Circuits and Systems*, McGraw-Hill, 1994.

[Leb99] J.W. LeBlanc, *A Compton Camera for Low Energy Gamma-Ray Imaging in Nuclear Medicine Applications*, Ph.D. Dissertation, University of Michigan, 1999.

[Lem93] A. Lempicki et al., *Fundamental limits of scintillator performance*, Nucl. Instr. and Meth. A 333, pp. 304-311, 1993.

[Leo94] W.R. Leo, *Techniques for Nuclear and Particle Physics Experiments*, 2nd ed., Springer-Verlag, 1994.

[Lin01] M. Lindner, *Entwicklung eines zählenden Pixeldetektors für "Digitales Röntgen"*, Ph.D. Dissertation, University of Bonn, 2001.

[Lut99] G. Lutz, *Semiconductor Radiation Detectors*, Springer-Verlag, 1999.

[Mat89] G. Matscheko et al., *Compton spectroscopy in the diagnostic x-ray energy range. II. Effects of scattering material and energy resolution*, Phys. Med. Biol., vol. 34, no. 2, pp. 199-208, 1989.

[Nic03] A. Niculae, *Development of a low noise analog readout for a DEPFET pixel detector*, Ph.D. Dissertation, University of Siegen, 2003.

[NIST04] National Institute of Standard and Technology, USA, 2004, http://www.physics.nist.gov/PhysRefData .

[Pat98] B.E. Patt et al., *High resolution CsI(Tl)/Si-PIN detector development for breast imaging*, IEEE Trans. Nucl. Sci., vol. 45, no. 4, pp. 2126-2131, 1998.

[Rad88] V. Radeka, *Low-noise techniques in detectors*, Ann. Rev. Nucl. Part. Sci., vol. 38, pp. 217-277, 1988.

[Ree72] W.A. Reed, P.Eisenberger, *Gamma-Ray Compton Profiles of Diamond, Silicon, and Germanium*, Phys. Rev. B, vol. 6, no. 12, pp. 4596-4604, Dec. 1972.

[Ren04] D. Renker, *Photosensors*, Nucl. Instr. and Meth. A 527, pp. 15-20, 2004.

[Rib75] R. Ribberfors, *Relationship of the relativistic Compton cross section to the momentum distribution of bound electron states*, Phys. Rev. B, vol 12, no. 6, pp. 2067-2074, Sept. 1975.

[Sae98] E. Saeckinger and W. Guggenbuehl, *A high-swing, high-impedance MOS cascode circuit*, IEEE J. Solid-State Circuits, vol. 25, pp. 289-297, Feb. 1990.

[San87] W. Sansen, *Integrated low-noise amplifiers in CMOS technology*, Nucl. Instr. and Meth. A 253, pp. 427-433, 1987.

[Sat02] G. Sato et al., *Characterization of CdTe/CdZnTe detectors*, IEEE Trans. Nucl. Sci., vol. 49, no. 3, pp. 1258-1263, 2002.

[Sch00] F. Schopper et al., *CsI calorimeter with 3-D position resolution*, Nucl. Instr. and Meth. A 442, pp. 394-399, 2000.

[Sch02] F. Schopper, *Entwicklung eines Teleskops zur Abbildung von Gammastrahlung mittels Comptonstoss und Paarerzeugung*, Ph.D. Dissertation, Technical University of Munich, 2002.

[Sed98] A.S. Sedra, K.C. Smith, *Microelectronic circuits*, Oxford Univ. Press, 1998.

[Ste91] M. Steyaert et al., *Full integration of extremely large time constants in CMOS*, Electron. Lett., vol. 27, no. 10, pp. 790-791, 1991.

[Sze81] S.M. Sze, *Physics of Semiconductor Devices*, 2nd ed., John Wiley & Sons, 1981.

[Sze85] S.M. Sze, *Semiconductor Devices, Physics and Technology*, John Wiley & Sons, 1985.

[Tom02] T. Tomitani and M. Hirasawa, *Image reconstruction from limited angle Compton camera data* , Phys. Med. Biol. vol. 47, pp. 2129-2145, 2002.

[Vit77] H. Vittoz, J. Fellrath *CMOS Analog Integrated Circuits Based on Weak Inversion Operation*, IEEE J. Solid-State Circuits, vol. SC-12, no. 3, pp. 224-231, 1977.

[Win04] A. Wintjen, *Entwicklung einer Ausleseelektronik fuer einen neuen Typ von Halbleiterdetektoren in CMOS-Technik*, Diploma Thesis, University of Siegen, 2004.

[Woa00] G. Woan, *The Cambridge Handbook of Physics Formulas*, Cambridge Univ. Press, 2000.

List of Figures

2.1 Energy loss for electron and proton in silicon 5
2.2 Range of electrons in silicon, cesium iodide and cadmium telluride 5
2.3 Photoelectric absorption 6
2.4 Compton scattering 7
2.5 a) Energy of the Compton edge as a function of photon energy b) Energy distribution of recoil electrons for E_γ=140.5keV and E_γ=364.5keV 7
2.6 Pair production and positron annihilation 8
2.7 Linear absorption coefficients as a function of photon energy for a) silicon b) cesium iodide 9
2.8 Energy band structure of a) silicon b) gallium arsenide(after [Sze85]) . . . 10
2.9 Band structure of an extrinsic semiconductor of a) p-type b) n-type 11
2.10 a) p-n junction at equilibrium; b) distribution of charge across the junction; c) distribution of electric field across the junction; d) distribution of electric potential across the junction 13
2.11 a) Reverse biased p^+-n junction as a radiation detector. Distributions of b) electric field and c) electric potential across the detector 14
2.12 Principle of a punch-through biasing. Side view of the detector and potential distribution near the surface for a) unbiased detector, b) reverse bias equal to the punch-through voltage and c) reverse bias larger than the punch-through voltage. 15
2.13 Structure of two neighbouring guard rings 16
2.14 Band structure of an inorganic scintillator 18
2.15 Structure of a silicon PIN photodiode 20

3.1 Principle of the Anger camera 24
3.2 Principle of the Compton camera 24
3.3 Photoabsorption efficiency as a function of energy[NIST04] for a) 300μm thick semiconductors b) 1.5cm thick scintillator crystals 26
3.4 Impact of the first detector geometry on angular uncertainty 28
3.5 Impact of the second detector geometry on angular uncertainty 29
3.6 Angular resolution: impact of the geometry of detectors 31
3.7 Angular resolution: impact of the scatter detector energy resolution 31
3.8 Compton effect with a vector diagram 32
3.9 Compton profile for crystalline silicon[Ree72] 33
3.10 $f(E_\gamma, \theta)$ as a function of scattering angle for two different energies 34

3.11 Total angular resolution: contribution of individual effects 34

4.1 The architecture of the RAMSES chip 36
4.2 The block diagram of the pixel 37
4.3 Noise sources in the analog readout 38
4.4 The charge amplifier 40
4.5 The OTA based CSA 41
4.6 Small signal equivalent circuit of the CSA 41
4.7 Dependence of thermal and flicker noise components and their sum on the gate width of the input transistor 43
4.8 Dependence of total noise on the gate width of the input transistor at different detector capacitances 43
4.9 The functional diagram of the cascode a) and the regulated cascode b) amplifiers 45
4.10 Schematic of the regulated cascode amplifier 45
4.11 Open loop transfer characteristics of the RGC amplifier 47
4.12 Noise contribution of the input FET to the total input noise 47
4.13 MOSFET as a feedback element: a) voltage-biased b) current-biased . . . 48
4.14 a) CSA test circuit b) Its equivalent according to the Miller theorem 49
4.15 CSA response to the inject pulse 50
4.16 The implemented CSA 52
4.17 Layout of the CSA($50\mu m \times 45\mu m$) 52
4.18 The functional diagram of the CRRC shaper 53
4.19 The CRRC shaper schematic 53
4.20 Small-signal model of the shaper 54
4.21 Noise contribution as a function of shaping time 55
4.22 Functional diagram of the peak detector 56
4.23 Block diagram of the discriminator 57
4.24 Implementation of the resistor chain 58
4.25 Sample of the discriminator threshold set 58
4.26 Principle of the time measurement in a pixel 59
4.27 Block diagram of the readout logic 60
4.28 The pixel control logic 61
4.29 An example of a sequential readout of multiple hits 62
4.30 Readout of a single hit: control signals 63
4.31 Block diagram of the Digital-to-Analog Converter 64
4.32 Simplified diagram of the current reference cell 64
4.33 Noise of the reference current 65
4.34 IMON structure 66
4.35 External current supply scheme for RAMSES circuits 66

5.1 Setup for data acquisition 67
5.2 Micro PCB with the RAMSES chip and the detector 68
5.3 Blueboard and PCBs in Faraday cage 69
5.4 Block diagram for CSA test 70
5.5 CSA output signal for different bias voltages *Vfeed* of the feedback transistor 71

5.6 CSA output voltage for a voltage step input signal. The rise time is measured between the vertical green lines at 10%(90%) of the signal 71
5.7 a) Fall time variation and b) DC-level variation of the CSA for 16 pixels . 72
5.8 Microphotograph of the wire-bond connection: a) chip side b) detector side 73
5.9 Block diagram for shaper testing 73
5.10 Shaper output signal for different DAC6 settings 74
5.11 Shaping time variation for 16 pixels 75
5.12 Shaper output signal for different amplitudes of the inject pulse 75
5.13 Setup used for the measurement with the external shaper 76
5.14 Noise as a function of shaping time for the CSA with open input and for the CSA bonded to the detector 76
5.15 Peak detector response for two different input signals 77
5.16 Drift of the peak value 78
5.17 The setup used for threshold scan 80
5.18 Threshold scan of a pixel; determination of the threshold and the noise . . 80
5.19 Threshold dependence on the adjustment code with DAC6=100 80
5.20 a) Minimum threshold with DAC6=50 for 16 pixels; threshold after adjustment to $1200e^{-}$ for 16 pixels b) Noise obtained from threshold scan for 16 pixels 81
5.21 TVC range selection 82
5.22 TVC output for two measured time intervals 82
5.23 Signal flow during readout of a single hit 83
5.24 Change of pedestals with shaper bias for 16 pixels 85
5.25 a) Sample of the linearity scan b) Gain variation for 16 pixels 85
5.26 a) Microphotograph of a part of the detector b) Detector dark current as a function of applied bias 86
5.27 Schematic cross section view and bias scheme of the detector 87
5.28 Test of the punch-through bias network a) Biasing scheme b) I-V characteristics 87
5.29 Energy spectrum of ^{109}Cd source 90
5.30 Energy spectrum of ^{55}Fe source 90

6.1 Side view of the cesium iodide detector 91
6.2 a) The photodiode array with the transparent silicon deposited on its surface(from [Sch02]) b) The array of 120 polished and isolated from each other CsI(Tl) crystals prepared for the optical coupling 92
6.3 a) Energy spectrum of ^{241}Am source in a single channel b) Histogram of noise performance of the Si-photodiode array connected to the TA1 chip . 93
6.4 a) Trigger rate for individual channels as a function of threshold b) Number of channels that have be masked to keep the total trigger rate below 100Hz as a function of threshold 94
6.5 Light output as a function of shaping time(from And[00]) 96
6.6 a) Distribution of light output as a function of the position in the crystal matrix b) Histogram of the distribution 97

6.7 a) Energy spectrum of the ^{137}Cs source with only single events from all channels summed b) Histogram of energy resolution of CsI detector for 662keV energy . . . 98
6.8 Energy spectrum of the ^{57}Co source with only single events from all channels summed . . . 98

A.1 Noise sources in a MOSFET . . . 106

B.1 Layout of a pixel cell . . . 109
B.2 Layout of the RAMSES chip . . . 110

D.1 Screenshot of the custom software . . . 114

Acknowledgements

First of all, my sincere gratitude goes to my supervisor, Prof. Dr. Martin Holder, for the initiation and support of this research, for his guidance, valuable advises and comments.

I would like to thank Dr. Adrian Niculae and Dr. Michael Ziolkowski for their helpful and constructive suggestions, for good and fruitful discussions. I thank Dr. Joachim Hausmann for his motivation and good ideas.

Furthermore, I am very grateful to Robert Andritschke and Dr. Florian Shopper from MPI for Extraterrestrial Physics in Garching, for helping me to understand and to assemble the CsI detector, used in this work.

I would also like to thank the other members of Prof. Holder's working group, especially Andreas Wintjen, Michael Krämer and our secretary, Margit Steinleitner, for their valuable help and for creating a friendly atmosphere.

Finally, I want to thank my parents and sister for their love and encouragement.